UNIVERSITY OF CALIFORNIA, SAN DIEGO

Wide Bandgap Semiconductors for Energy Efficiency and Renewable Energy Applications

A dissertation submitted in partial satisfaction of the

requirements for the degree Doctor of Philosophy

in

Electrical Engineering (Nanoscale Device and System)

by

Muchuan Yang

Committee in charge:

Professor Deli Wang, Chair
Professor Joanna M. McKittrick
Professor Donald J. Sirbuly
Professor Jie Xiang
Professor Paul K.L.Yu

2014

The Dissertation of Muchuan Yang is approved, and it is acceptable in quality and form for publication on microfilm and electronically:

_____

_____

_____

_____

_____

Chair

University of California, San Diego

2014

DEDICATION

To my parents

EPIGRAPH

I have missed more than 9000 shots in my career.

I have lost almost 300 games. 26 times, I have been trusted to take the game winning shot and missed.

I have failed over and over and over again in my life.

And that is why I succeed.

Michael Jordan

TABLE OF CONTENTS

LIST OF FIGURES

LIST OF TABLES

ACKNOWLEDGEMENTS

First of all, I would like to express my deepest appreciation to my advisor Professor Deli Wang for giving the opportunity to study and work at UCSD. I would like to acknowledge him for all the advice, guidance, and encouragement he gave me during this amazing journey. The lessons he gave me will be treasured in my mind for the rest of my life.

I would like to thank our former and current group members: Prof. Chun Li, Dr. Yi Jing, Dr. Ke Sun, Conor Riley, Namseok Park, Sun Young Noh, Siarhei Vishniakou, Brian Lewis, Alireza Kargar, Zhelin Sun, and Justin Cheung.

I would also like to thank Professor Paul. K. L. Yu for allowing me to study and use the III-nitride MOCVD system. Most of my work is based on InGaN/GaN MOCVD growth. I would like to thank my other committee members: Professor Joanna McKittrick, Professor Donald J. Sirbuly and Professor Jie Xiang.

I would also like to acknowledge the staffs at the UCSD Nano3 including Dr. Bernd Fruhberger, Ryan Anderson, Larry Grissom, Dr. Maribel Montero, and Sean Parks for their valuable help and advice on my research.

Chapter 3, section 3.3, in part has been submitted for publication of the material as it may appear in Physical Chemistry Chemical Physics, 2014, Yang, Muchuan; Sun, Ke; Cheung Justin; Yu, Paul K.L.; Wang, Deli. The dissertation author was the primary investigator and the first author of this paper.

Chapter 3, section 3.4 in part is currently being prepared for submission for publication of the material. Yang, Muchuan; Lu, Dylan; Yuan, Dajun; Wang, Hsin-Ping;

He, Jr-Hau; Liu, Zhaowei; Yu, Paul K.L.; Wang, Deli. The dissertation author was the primary investigator and the first author of this paper.

Chapter 4, in part is currently being prepared for submission for publication of the material. Yang, Muchuan; Li, Chun; Sun, Ke; Jing, Yi; Bendo, Yoshio; Wang, Deli. The dissertation author was the primary investigator and the first author of this paper.

VITA

2007	Bachelor of Science, Southeast University, China
2009-2014	Department of Electrical and Computer Engineering University of California, San Diego
2012	Master of Science, University of California, San Diego
2014	Doctor of Philosophy, University of California, San Diego

ABSTRACT OF THE DISSERTATION

Wide Bandgap Semiconductors for
Energy Efficiency and Renewable Energy Applications

by

Muchuan Yang

Doctor of Philosophy

University of California, San Diego, 2014

Professor Deli Wang, Chair

Energy has emerged to be a global concern as the world confronts the challenges of population growth, climate change, economic recovery, energy affordability. To overcome the energy crisis, people need to work with both hands: use one hand to make a transition from fossil fuels to clean, renewable energy and the other hand to cut down energy consumption by developing energy efficient devices and systems. In this dissertation, I focus my research to tackle these problems using wide

bandgap semiconductors, III-nitride (GaN and InGaN) and zinc oxide (ZnO) as basic materials due to their unique optoelectronic properties. Material growth — III-nitride using MOCVD and ZnO using hydrothermal solution synthesis are studied.

For renewable energy application, I developed InGaN/GaN MQW photoelectrode for spontaneous photoelectrochemical (PEC) water splitting and hydrogen fuel generation. The InGaN/GaN MQW structure provides sufficient photovoltage to split water. Using this single photoelectrode, a current density of 0.16 $mA \cdot cm^{-2}$ and a peak solar-to-hydrogen conversion efficiency of 0.2% are obtained at zero external bias. Two schemes are studied to improve the photoelectrode efficiency and stability. By adding NiO_x oxygen evolution catalyst, the overall solar-to-hydrogen conversion efficiency is improved to 0.64% at zero bias. The stability of photoelectrode is also much improved and photocurrent reduction of 4.5% in 12 hours is achieved. In order to further boost the performance of the photoelectrode, plasmonic metal nanostructures are created for enhanced light absorption. The conversion efficiency is improved up to 0.93%.

For energy-saving application, I demonstrated a novel lighting technology based on nano-materials—ZnO nanowires and carbon nanotubes. The novel design, junctionless light emitting device, consists of a carbon nanotube array cathode for electron field emission and a ZnO nanowire array light-emitting anode. High energy electrons directly bombard onto nanowires, generate electron-hole pairs, which subsequently recombine to emit light. Strong near band edge emission is obtained with a peak at 390 nm. The use of vertical nanowire array as anode offers advantages in increasing the junction area and carrier recombination/photon generation and enhancing

the light extraction efficiency. This approach utilizes the unique properties of nanoscale materials and opens an area for efficient lighting technologies in the future.

Chapter 1

Introduction

1.1 Energy crisis and environmental issue

Energy has emerged to be a global concern as the world confronts the challenges of population growth, climate change, economic recovery, and energy affordability. The global population has grown from about 6 billion in 2001 to nearly 7 billion in 2011, and is projected to increase to 9 billion in 2050. Combined with the economic growth, the scenario of future energy demand can be estimated by:[1]

$$\dot{E} = N \times (GDP/N) \times \left(\dot{E}/GDP \right) \qquad \textbf{1-1}$$

where $\dot{E}$ is the rate of energy consumption, N is the global population, GDP/N is the globally averaged gross domestic product (GDP) per capita, and $\dot{E}/GDP$ is the globally averaged energy intensity (the energy consumed per unit of GDP). According to Table 1-1, world per capita GDP was $ 7500 in 2001, and is projected to increase to $15000 per capita by 2050. With no changes in the globally averaged energy intensity, the world energy consumption rate would grow, due to population growth and economic growth, from 13.5 TW in 2001 to 40.8 TW in 2050. Even factoring in a decrease in energy intensity, the world energy consumption rate is still projected to be doubled from 13.5 TW in 2001 to 27 TW by 2050. Therefore, meeting the current and future demand for energy is of crucial importance, and is a huge challenge for human beings.

Through many tens of millions of years of biogenic-abiogenic processes, nature has stored vast amounts of fossil energy in the form of coal, petroleum, natural gas, shale oil and tar sands. The World Energy Assessment Report estimates of the total reserves and of the global resource base provide a benchmark for evaluating the total available global fossil energy base. 40-80 yr of oil reserves, 60-160 yr reserves of natural gas are present, and a 250 yr supply of coal. Although the estimated fossil energy resources could support the planet for several centuries, the devil is always in the details. As one source is depleted another will suffer higher rate of consumption with, in turn, more rapid depletion. There are also the unanticipated losses, such as coal mine fires or sabotage of oil pipelines.

Table 1-1: World energy statistics and projections.[1]

Quantity	Definition	Units	2001	2050
N	Population	B persons	6.145	9.4
GDP	Gross domestic product	T $/yr	46	140
GDP/N	Per capita GDP	$/(person-yr)	7470	14850
$\dot{E}$	Energy consumption rate	TW	13.5	27.6
$\dot{E}$/GDP	Energy intensity	W/($/yr)	0.294	0.2

A perhaps far more serious concern associated with the use of fossil fuels is the impact on the environment. The main concern in this regard is the emission of greenhouse gases, in particular CO_2, and their contribution to global climate change. The CO_2 concentration in the past 50 yr has been rising because of anthropogenic CO_2 emissions from fossil fuel consumption. It is now in excess of 380 ppm (part per million), and is currently rising by about 2 ppm/year. According to the International Panel on Climate Change (IPCC), a CO_2 level above 450 ppm carriers a high risk of causing global warming by more than 2ºC. Such a rise is likely to have a severe adverse impact on

ecosystems and human society. If the temperature change can be limited to less than 2ºC, there is a good chance that society can adapt. Several studies agree that the current decade, between 2010 and 2020, is a critical one. Unless we are able to sharply reduce CO_2 emissions within the next 10 years, exceeding the 450 ppm level seems unavoidable. Indeed, the transition from fossil fuels to clean, renewable energy sources is of revolutionary importance for its societal impact.

1.2 Renewable energy and energy efficiency

In order to reduce the human dependence on fossil fuels and decrease the exhaust of CO_2, we need to work with two hands: one hand to make the transition toward clean, renewable energy sources; and the other hand to dramatically reduce the energy consumption by developing more energy efficient devices and systems. Nowadays, undergoing intensive research is a wide variety of renewable energy technologies are undergoing intensive study and research, such as solar, wind, biomass, geothermal as well as technologies to adopt or replace current lighting, building heating and cooling, and water heating devices or systems for improved energy efficiency. My research tackles both energy harvesting and efficiency and focuses on developing solar water splitting hydrogen fuel cells, specifically photoelectrochemical (PEC) cells, and new energy-saving lighting technology, junctionless light emitting device, by using nanoscale materials — carbon nanotubes (CNTs) and ZnO nanowires (NWs).

1.2.1 Renewable energy and PEC hydrogen production

The main attraction of renewable energy is that it is abundant, clean, and will last as long as the planet exists. The ultimate renewable energy resource is the sun. The supply of energy from the sun to the earth is gigantic: 3×10^{24} joules a year, approximately

10,000 times more than the global energy consumption. Therefore, solar energy conversion is a promising way to provide a clean and sustainable energy source to meet the increasing energy demand. Currently, solar energy is mainly converted into electricity using solar cells. The major drawback of electricity is that it is difficult to store. The common storage container for electricity is the battery. However, the battery technology itself is still under development and suffers from all kinds of problems, such as small energy density, short lifetime, and the potential leakage of the toxic chemicals used in batteries.

Another pathway of utilizing solar energy is to convert it into hydrogen, which is envisioned as the ideal energy-carrier for storage and distribution. In contrast to electricity, hydrogen can be easily stored in a gas container for long periods. Also, it can be readily distributed through transportation or pipelines. PEC solar water splitting is one of the most promising renewable energy technologies for converting solar energy to hydrogen for uses in the future hydrogen economy.[2-6] A major advantage of PEC cell is that it is very simple and elegant in concept and involves relatively less processes steps as compared to many other H_2 production methods. As shown in Figure 1-1, PEC cells are usually built from photo-sensitive semiconductors, which use solar photons to generate a sufficient voltage in an electrolysis cell to electrolyze water, producing H_2 and O_2 gases simultaneously. If the solar energy is only energy input in the PEC system, and is able to drive both H_2 and O_2 evolution reactions, then we call it spontaneous solar water splitting.

The primary challenges for PEC are to develop semiconductor photoelectrodes with sufficient photovoltage to electrolyze water, to minimize internal resistance losses, to have long lifetime, to maximize photon utilization efficiencies, and to reduce

manufacturing cost. However, integrating all these properties into one single semiconductor turns out extremely difficult, sometimes even conflict.

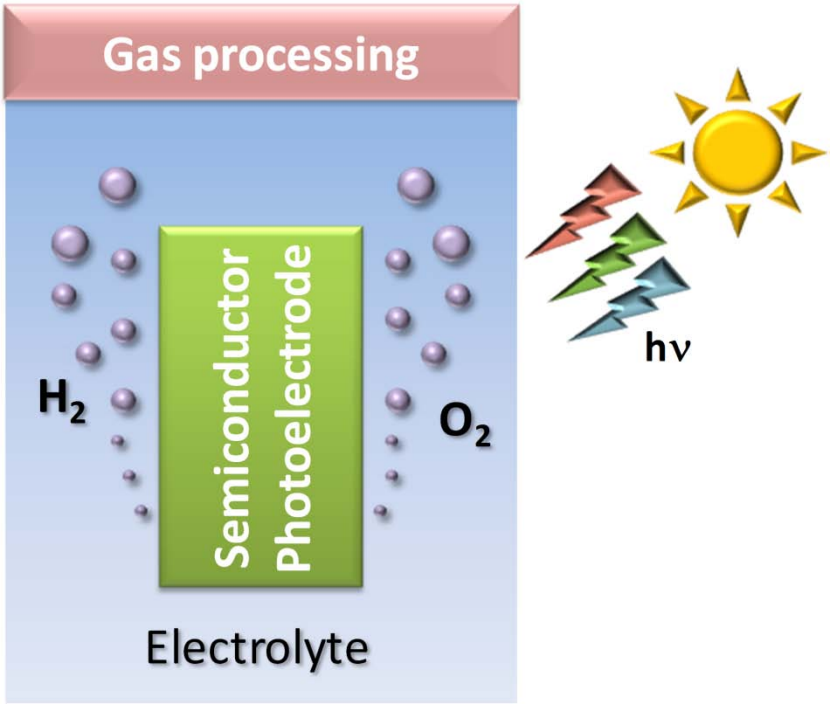

Figure 1-1: Concept of PEC solar water splitting and hydrogen production.

In my work, III-nitrides, specifically InGaN/GaN multiple quantum wells (MQWs) are applied as an essential building block for photoelectrode. Our design and the unique properties provided by the structure overcome those inherent obstacles existing in photoelectrodes for PEC. Spontaneous PEC water splitting with the solar as the sole energy input is achieved.

1.2.2 Semiconductor lighting technology

Lighting is an essential part in human beings' life, and consumes nearly 20% of total electricity generated globally. Since nowadays, most of the electricity is still generated by burning fossil fuels; lighting is also the second largest CO_2 emission source. There are several lighting technologies that are presently used, such as incandescent,

compact fluorescent lamp (CFL), and semiconductor solid state lighting. Among these, incandescent has been used for long time and is the most popular lighting method. However, it is also the most inefficient lighting technology, in which over 90% of the energy is wasted as heat rather than light. CFL is much more energy efficient than incandescent, but has its own problem. Each CFL contains a small amount of toxic mercury, which could a substantial threat to the environment if not deal properly. Semiconductor solid state lighting is by far the most promising lighting technology because of its high efficiency and long lifetime.[7] Wide bandgap semiconductors, such as GaN and InGaN are core materials in solid state lighting. One of the issues associated with wide bandgap semiconductors is that there is a large refractive index difference between semiconductors and air. For example, GaN has a refractive index of 2.5, and the refractive index for air is 1. This large difference leads to an effect called total internal reflection, in which a critical angle will restrict the light emission in semiconductor. Only very small portion of light within critical angle can effectively escape from the semiconductor, and the rest will be confined in materials and eventually get lost as heat. As a matter of fact, for GaN, the critical angle is only 23º.[8] Therefore, finding a way to improve the light extraction efficiency is of great importance to solid state lighting.

Semiconductor NWs are very promising building blocks for high efficiency lighting technology.[9-15] The nanoscale interface between the NW and substrate material relaxes the lattice matching requirement, which allows more versatile design of the light emitting system. More importantly, NWs have the ability to improve the light extraction efficiency due to the waveguide effect[16] or photonic crystal effect. These properties make semiconductor NW extremely important and attract a lot of research interests as a new

platform for next generation light emitting devices. In my work, low temperature solution grown ZnO NW arrays are used as active light emitting materials, and strong near band edge emission is demonstrated.

1.3 Wide bandgap semiconductors

Wide bandgap semiconductors are poised to revolutionize the next generation of energy-saving solid state lighting and clean energy innovations. GaN, for example, is an enabling material behind the ultra-high efficiency light emitting diodes (LEDs), which produce more than 10 times more light per watt of input energy than comparable incandescent bulbs and extend service life by 30 times or more.[17, 18] ZnO, another wide bandgap semiconductor, has also attracted a lot of attention owing to its large exciton binding energy, which is expected to be favorable for high efficiency light emitting devices, especially laser diodes (LDs) up to high temperatures.[19]

Meanwhile, wide bandgap semiconductors are also expected to pave the way for exciting innovations in renewable energy applications. For example, as a direct bandgap semiconductor, GaN can only response to the UV light, because of its wide bandgap (3.4 eV). However, by incorporating In into GaN to form InGaN alloy, it can absorb smaller energy photons coming from the visible region. Harnessing these properties can lead to new opportunities in clean energy applications, such as solar cells and PEC fuel cells.

Wide bandgap semiconductors are a foundational technology that promises to transform multiple industries and markets. Extensive research and use of wide bandgap semiconductors and their related devices will have a huge impact on energy saving and environmental issues.

1.4 Dissertation outline

Chapter 2 discusses material growth, including metal-organic chemical vapor deposition (MOCVD) of InGaN/GaN MQWs and hydrothermal solution growth of ZnO NWs. In chapter 3, InGaN/GaN MQW PEC cell will be discussed in detail. In section 3.1, basic PEC principles are introduced, and various photoanodes for PEC water splitting will be briefly reviewed. In section 3.2, bare InGaN/GaN MQW photoanode is demonstrated for un-biased spontaneous PEC water splitting. In section 3.3, InGaN/GaN MQW photoelectrodes with NiO_x|Ni electrocatalysts for efficient oxygen evolution are discussed. In section 3.4, plasmonic metal nanostructures are created on the photoanode surface to further improve the light absorption and boost the PEC performance. In Chapter 4, a novel device concept — junctionless light emitting device with ZnO NWs as UV emitters is proposed and demonstrated. Chapter 5 and 6 concludes and briefly discusses the future work, respectively.

1.5 References

1. Lewis N.S., Nocera D.G. Powering the planet: Chemical challenges in solar energy utilization. *Proceedings of the National Academy of Sciences* **103**, 15729 (2006).

2. Fujishima A., Honda K. Electrochemical Photolysis of Water at a Semiconductor Electrode. *Nature* **238**, 37 (1972).

3. Gratzel M. Photoelectrochemical cells. *Nature* **414**, 338 (2001).

4. Walter M.G., Warren E.L., McKone J.R., Boettcher S.W., Mi Q., Santori E.A., Lewis N.S. Solar Water Splitting Cells. *Chemical Reviews* **110**, 6446 (2010).

5. Tachibana Y., Vayssieres L., Durrant J.R. Artificial photosynthesis for solar water-splitting. *Nature Photonics* **6**, 511 (2012).

6. Grimes C.A., Varghese O.K., Ranjan S. Light, Water, Hydrogen. Springer US (2008).

7. Pimputkar S., Speck J.S., DenBaars S.P., Nakamura S. Prospects for LED lighting. *Nature Photonics* **3**, 180 (2009).

8. Huh C., Lee K.-S., Kang E.-J., Park S.-J. Improved light-output and electrical performance of InGaN-based light-emitting diode by microroughening of the p-GaN surface. *Journal of Applied Physics* **93**, 9383 (2003).

9. Duan X., Huang Y., Cui Y., Wang J., Lieber C.M. Indium phosphide nanowires as building blocks for nanoscale electronic and optoelectronic devices. *Nature* **409**, 66 (2001).

10. Yan R., Gargas D., Yang P. Nanowire photonics. *Nature Photonics* **3**, 569 (2009).

11. Gargas D.J., Gao H., Wang H., Yang P. High Quantum Efficiency of Band-Edge Emission from ZnO Nanowires. *Nano Letters* **11**, 3792 (2011).

12. Yeh T.-W., Lin Y.-T., Stewart L.S., Dapkus P.D., Sarkissian R., O'Brien J.D., Ahn B., Nutt S.R. InGaN/GaN Multiple Quantum Wells Grown on Nonpolar Facets of Vertical GaN Nanorod Arrays. *Nano Letters* **12**, 3257 (2012).

13. Chen M.-T., Lu M.-P., Wu Y.-J., Song J., Lee C.-Y., Lu M.-Y., Chang Y.-C., Chou L.-J., Wang Z.L., Chen L.-J. Near UV LEDs Made with in Situ Doped p-n Homojunction ZnO Nanowire Arrays. *Nano Letters* **10**, 4387 (2010).

14. Lee J.M., Choung J.W., Yi J., Lee D.H., Samal M., Yi D.K., Lee C.-H., Yi G.-C., Paik U., Rogers J.A., Park W.I. Vertical Pillar-Superlattice Array and Graphene Hybrid Light Emitting Diodes. *Nano Letters* **10**, 2783 (2010).

15. Qian F., Li Y., Gradečak S., Wang D., Barrelet C.J., Lieber C.M. Gallium Nitride-Based Nanowire Radial Heterostructures for Nanophotonics. *Nano Letters* **4**, 1975 (2004).

16. Kuo M.-L., Kim Y.-S., Hsieh M.-L., Lin S.-Y. Efficient and Directed Nano-LED Emission by a Complete Elimination of Transverse-Electric Guided Modes. *Nano Letters* **11**, 476 (2010).

17. Nakamura S., Senoh M., Nagahama S.-i., Iwasa N., Yamada T., Matsushita T., Sugimoto Y., Kiyoku H. Ridge-geometry InGaN multi-quantum-well-structure laser diodes. *Applied Physics Letters* **69**, 1477 (1996).

18. Nakamura S., Pearton S., Fasol G. The Blue Laser Diode. Springer Berlin Heidelberg (2000).

19. Takahashi K., Yoshikawa A., Sandhu A. Wide Bandgap Semiconductors. Springer Berlin Heidelberg (2007).

Chapter 2

Materials Growth

2.1 Introduction

Wide bandgap semiconductors GaN and ZnO have the same crystal structure of the hexagonal wurtzite type as shown in Figure 2-1, with the similar lattice constants that are summarized in Table 2-1.[1]

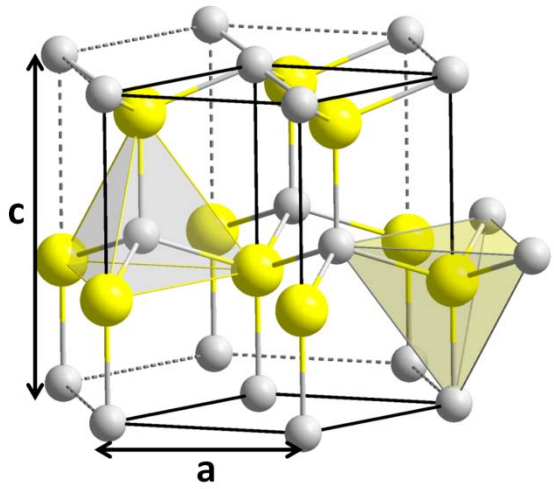

Figure 2-1: Wurtzite crystal structure of GaN and ZnO.

The direct wide bandgaps of GaN and ZnO make them particularly important in short wavelength (blue/UV) optoelectronic devices and applications. For example, the "blue light emitting diode" is a well know application of GaN, which revolutionized the solid state lighting technology.[2] From then on, GaN has become one of the most exploited semiconductors as optical sources for full color displays, white light illumination, and blue-violet laser diode (LD)[3] for high density DVDs.[4]

For solar energy conversion applications, such as photovoltaic cells, PEC water splitting and hydrogen fuel generation, people want the active material to be able to absorb as much solar light as possible. Although GaN has a wide bandgap of 3.4 eV, which only works in the UV region, by introducing indium (In) into GaN, to form InGaN alloy, the light response can be extended into the visible region. InN has a small bandgap of 0.7 eV, theoretically, by increasing the In concentration in the InGaN alloy, it should be able to cover the entire solar spectrum. Moreover, InGaN has a high absorption coefficient ~ 10^5 cm^{-1}.[5] These properties make InGaN alloy promising as solar energy harvesting material. However, because of the large lattice mismatch between InN and GaN and low In solubility,[6] it is difficult to obtain thick high quality InGaN film with high In concentration. The solution is to have InGaN/GaN MQW structure. With reduced thickness of InGaN, the QW region can achieve high In concentration, while maintain good crystal quality. The QW growth repeats several times to increase the total thickness of InGaN for light absorption.

Recently, there is a widespread interest in the use of ZnO in UV light emitting diodes (LEDs) and LDs, because of its unique large exciton binding energy (60 meV).[7] A lot of research effort has been made to develop ZnO nanostructures[8], such as nanowires or nanorods, for next generation of light emitters and waveguides.[9]

Table 2-1: Energy bandgaps and lattice constants of GaN and ZnO.

Material	Energy Bandgap (eV)	a (Å)	c (Å)
GaN	3.4	3.18	5.2
ZnO	3.3	3.25	5.18

In this chapter, metal-organic chemical vapor deposition (MOCVD) of InGaN/GaN MQW structure will first be introduced. Both ZnO nanowire and thin film

grown by hydrothermal method will then be discussed. Lastly, InGaN/GaN epi-grwoth on solution synthesized ZnO film will be demonstrated.

2.2 MOCVD growth of InGaN/GaN MQWs

MOCVD is the most common technique for growing III-nitride semiconductors. The growth of GaN and MQWs are performed in a Thomas Swan 3×2 FT MOCVD system (Figure 2-2).

Figure 2-2: Thomas Swan 3×2 FT MOCVD system.

Trimethylgallium (TMGa),Triethylgallium, and Trimethylindium (TMIn) are the common precursors to introduce metal into the MOCVD reactor. Carrier gases, such as H_2 and N_2 are used to move the precursors into the reactor as they have a high vapor pressure at room temperature. Ammonia (NH_3) is used as the nitrogen source. Silane (SiH_4) is normally used to introduce Si into the reactor as an n-type dopant, while Biscyclopentadienyl magnesium (Cp_2Mg) is used to carry Mg, which is a p-type dopant.

During growth, the precursor gases are transported into the reactor, which is kept at elevated temperatures, causing the pyrolysis of the precursors, which then react, and deposit on the substrate surface. A typical deposition reaction of GaN can be described in:

$$(CH_3)_3Ga + NH_3 \rightarrow GaN + 3CH_4 \qquad \textbf{2-1}$$

During growth, a single wavelength reflectometry at 635 nm is used for highly accurate growth rate and surface roughness measurement. GaN is transparent at 635nm, so a light beam incident perpendicular to the sample will not be significantly absorbed. Based on differences between the refractive indices of the substrate and GaN epilayer, reflection will occur at the interface of the materials. Since the constructive and destructive interference depending on the thickness of the film, it is possible to measure the growth of the film through the use of Fabry-Perot oscillations in the reflectance spectra. In addition, the reflectance spectrum provides a way to monitor steps during the growth. A typical in-situ reflectometry data for InGaN/GaN MQW growth is shown in Figure 2-3. Detailed growth conditions will be introduced in the next few sections.

2.2.1 Substrate

The most commonly used substrate for GaN epitaxy is (0001) c-sapphire. Figure 2-4 gives a schematic depiction of the growth of a (1000) GaN film onto a c-sapphire substrate clearly indicating the large lattice mismatch (16%).[10] Besides, there is also a large thermal expansion mismatch between sapphire substrate and GaN film. Both of them lead to poor material quality. However, sapphire is thermally stable during high temperature growth and mechanically hard during the follow up fabrication processes. It is also transparent to the most of spectrum. Moreover, it is relatively inexpensive

compared to other possible substrates for GaN epitaxy. Therefore, to overcome the lattice and thermal expansion mismatches and continue using sapphire as substrate for GaN growth, buffer layers are typically employed for the growth of high quality GaN.

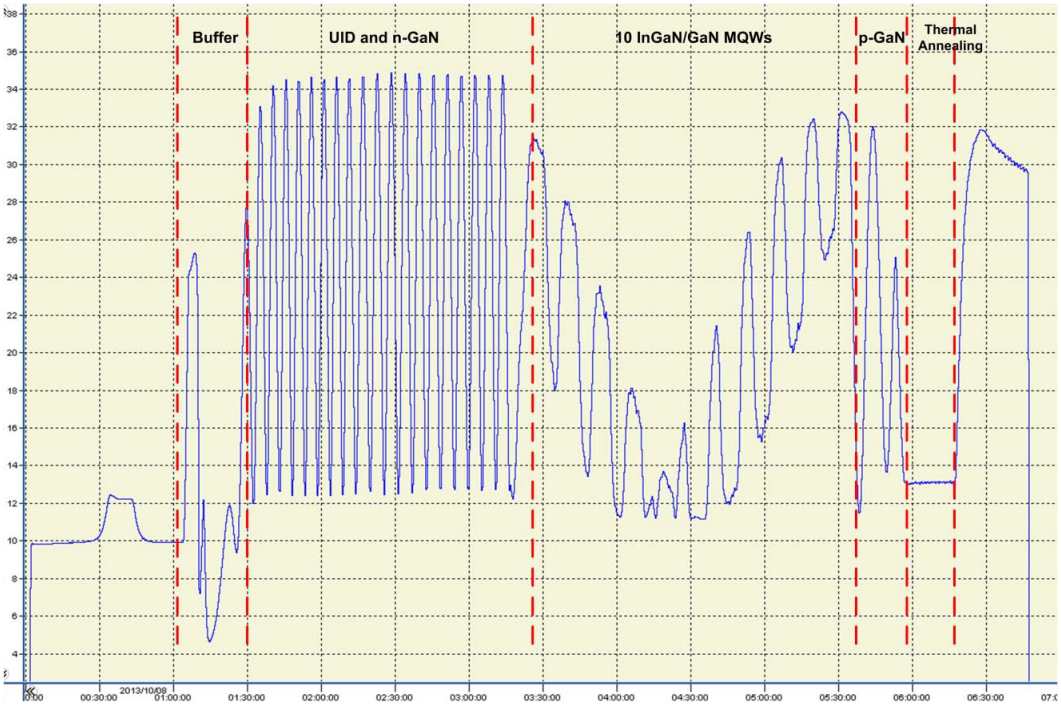

Figure 2-3: In-situ reflectometry data for InGaN/GaN MQW growth.

2.2.2 Buffer layer

A low temperature buffer layer is grown to absorb defects due to the lattice mismatch, which will allow a high temperature growth to yield a superior crystalline quality GaN film. First, a prebaking takes place, where the substrate is heated to around 1100 ºC for 10 minutes in hydrogen to improve the surface quality followed by a nitridation by having NH_3 into the reactor. The GaN buffer layer is grown at 530 ºC, 600 mbar with TMGa and NH_3 flow rate of 15 and 1000 sccm for 3 minutes.

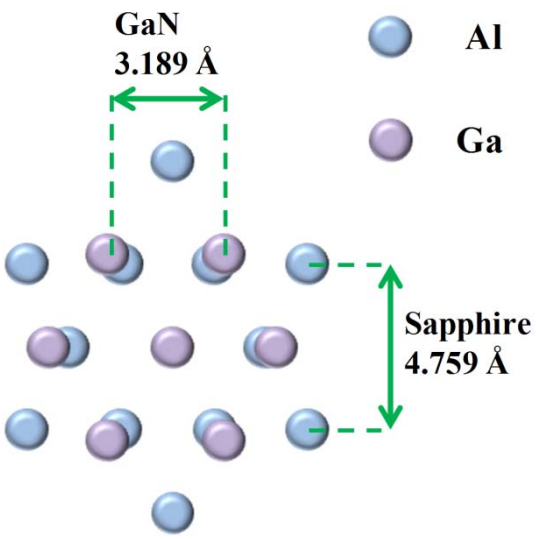

Figure 2-4: Schematic of GaN growth onto c-sapphire substrate.

The buffer layer has poor crystal quality because of the low temperature growth. In order to improve the crystal quality, the reactor temperature is raised to 1040 ºC for buffer nucleation and recrystallization, and get ready for GaN growth.

2.2.3 UID and n-GaN layer

After the buffer layer growth, two layers of GaN growth are done. First, an unintentionally doped (UID) GaN layer is grown at 1040 ºC, 300mbar, with with TMGa and NH_3 flow rate of 37.5 and 2500 sccm, respectively, for 1 hour. Then, an n-GaN layer is grown by introducing saline into the reactor. The growth temperature keeps at 1040 ºC, with growth pressure of 200 mbar, and TMGa, NH_3, and effective saline flow rate of 35, 3500 and 1.4 sccm, respectively. The growth continues for another hour. The obtained n-GaN layer has a thickness of around 1 μm and a doping concentration of around 3×10^{18} cm^{-3}.

2.2.4 InGaN/GaN MQW layer

The InGaN/GaN MQW layer growth is done using nitrogen as carrier gas. Ten periods of InGaN/GaN QW layers are grown. For each period, the growth temperature of the InGaN quantum well (QW) region is 692 ºC and the TEGa and TMIn flow rates are 16 and 80 sccm, respectively. TEGa is applied because it has a lower pyrolysis temperature compared to TMGa. The growth time is 90 seconds, which results a 3 nm thick InGaN QW region. The QW growth finishes with a cap layer at same temperature. The GaN quantum barrier (QB) is then grown at 850 ºC for 190 seconds with the TEGa flow being increased to 100 sccm. The same process repeats ten times.

2.2.5 P-GaN layer

The p-GaN growth is done in hydrogen ambient. The growth temperature is raised to 950 ºC, with TMGa, NH_3, and Cp_2Mg flow rates of 15, 4000 and 350 sccm, respectively. The obtained p-GaN layer has a thickness of around 200 nm and a doping concentration of around 5×10^{17} cm^{-3}.

For a long time it was impossible to obtain p-GaN films. Unavailability of p-GaN films has prevented III-nitrides from yielding LEDs or LDs. It was only in 1992 that people found that p-GaN with low resistance could be obtained by thermal annealing of the GaN crystal after growth.[11] In addition, the role of hydrogen atoms in the passivation mechanism of Mg acceptors was then clarified.[12] This thermal annealing technique is now commonly used to obtain MOCVD grown p-GaN. After the p-GaN growth, the reactor temperature is reduced to 750 ºC, and the system is again taken back into nitrogen atmosphere. The thermal annealing time is 20 minutes.

2.2.6 Material characterization

High resolution x-ray diffraction (HR-XRD) and scanning transmission electron microscopy (STEM) are used to characterize the material quality of the as-grown InGaN/GaN MQW structure. Figure 2-5 shows HR-XRD pattern in the (0002) plane of the sample using ω-2θscan. The major sharp peak originates from the n-GaN layer below

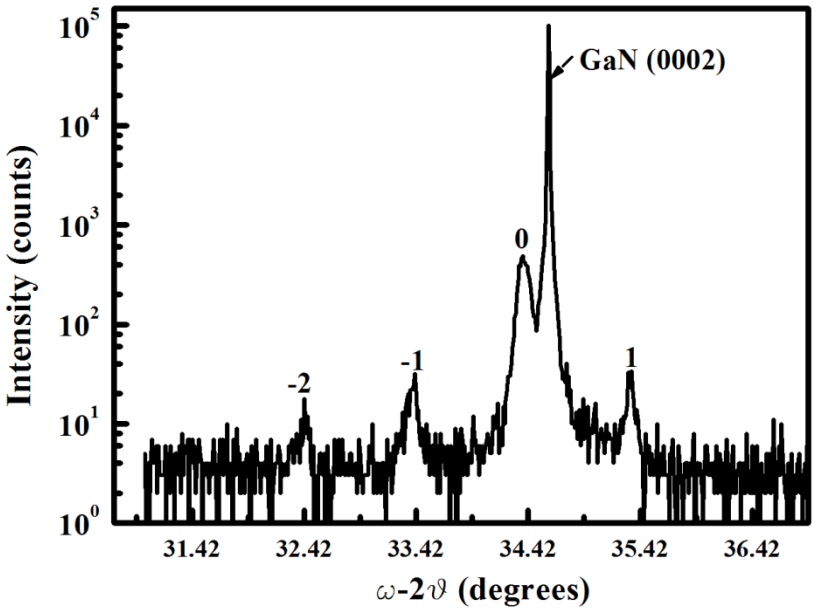

Figure 2-5: HR-XRD of (0002) plane of InGaN/GaN MQW sample.

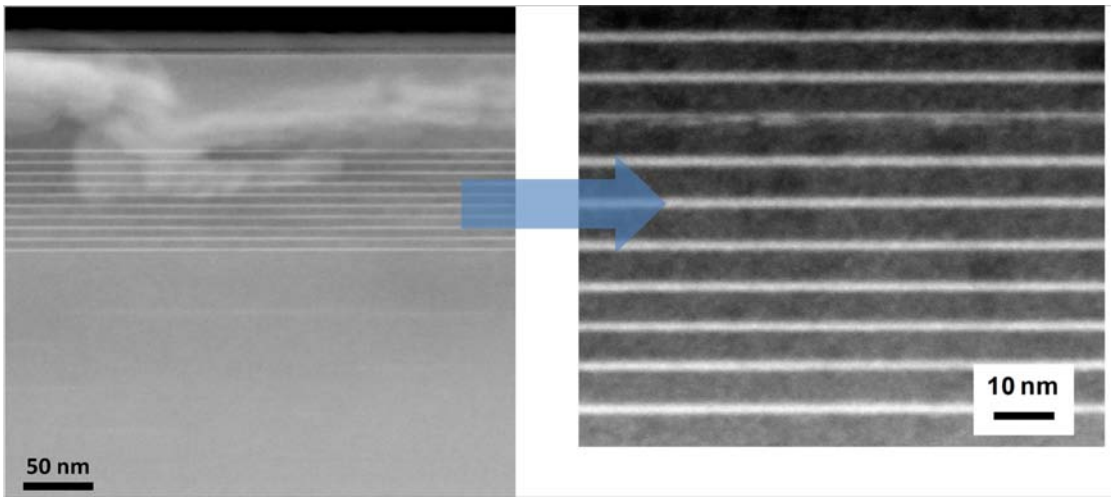

Figure 2-6: STEM image of InGaN/GaN MQW sample. Magnification of MQW region (right image) shows ten periods of QWs.

the MQWs. The satellite peaks (0, -1, -2) are resulted from the dynamic interference and diffraction of x-ray beams from the MQWs, which indicate excellent layer periodicity of the InGaN/GaN MQWs.[13] The small peaks between those satellite peaks imply the recognizable and abrupt interfaces between QW and QB.[14] The Cross-sectional STEM image is shown in Figure 2-6, with n-GaN, InGaN/GaN MQWs, and p-GaN layers. The magnification of MQW region confirms 10 periods of InGaN/GaN layers with sharp interfaces and without observable threading dislocations. The electroluminescence (EL) measurement (Figure 2-7) is conducted to determine the bandgap of the as-grown sample.

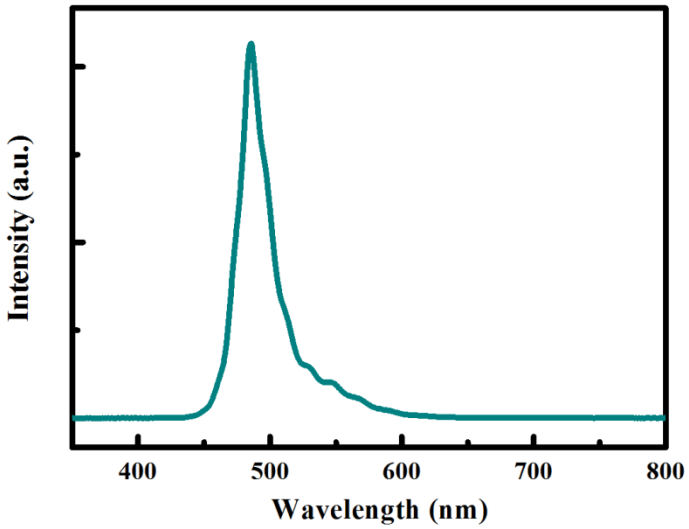

Figure 2-7: EL spectrum of InGaN/GaN MQW sample.

The EL spectrum shows a single peak at 485 nm which corresponds to an energy gap of 2.55eV and an estimated 22.5% In concentration in the MQW by using Equation 2-2:

$$E_g = xE_g(InN) + (1-x)E_g(GaN) - bx(1-x) \qquad \textbf{2-2}$$

with a bowing parameter b of 1.4.[15]

2.3 Hydrothermal synthesis of ZnO

As low temperature aqueous solution process, hydrothermal synthesis of nanostructures holds great promise for nanoscale fabrication and engineering.[16, 17] It is actually the crystallization from supersaturated aqueous solution, and is compatible with a variety of substrates. Moreover, hydrothermal synthesis is a low cost process, and has good potential for scale-up production. In this section, bottom-up hydrothermal growth of ZnO nanowire array will first be demonstrated, followed by ZnO thin film synthesis.

2.3.1 ZnO nanowire array growth

In this section, aqueous solution growth of ZnO NW arrays will be demonstrated on a c-sapphire substrate. First, a 40 nm ZnO thin film is sputtered on the substrate as a seeding layer for the solution growth. The growth of ZnO NWs is as following: 25 mM of zinc acetate and hexamethylenetetramine (HMTA) in DI water is prepared. Quartz substrate is fixed on a supporting glass slide, with the ZnO coated side down and immerses in the solution. The reactor is placed in a silicone oil bath with the inner temperature maintained at 85 ºC.[18] The solution growth is gently agitated at 200 rpm for 2 hours. Vertically aligned ZnO NW arrays are obtained, as shown in Figure 2-8, with average diameter of 150 nm and length of 2 μm.

In aqueous solution, zinc salt is solvated by water, giving rise to several hydroxyl species, including $ZnOH^{+}(aq)$, $Zn(OH)_2(aq)$, $Zn(OH)_3^{-}(aq)$ and $Zn(OH)_4^{2-}$. Solid ZnO nuclei are formed by the dehydration of these hydroxyl species.[19] Because each face of ZnO wurtzite crystal has a different associated free energy, the actual deposition rate of zinc ion species on these faces varies, leading to different morphologies. For ZnO, the

$\{0001\}$ planes along the c axis has the highest energy, thus (0001) is the fastest growing direction, which results in vertical ZnO NWs.

HMTA has a profound effect on the ZnO NW growth. First, it acts as a pH buffer. In order to promote ZnO precipitation, basic condition is crucial because divalent metal ions do not readily hydrolyze in acidic media.[20] HMTA is used to increase the pH at the crystal surface. Additionally, HMTA may also have an effect on hindering the ZnO growth of certain surfaces, which eventually leads to one-dimensional NW structure.

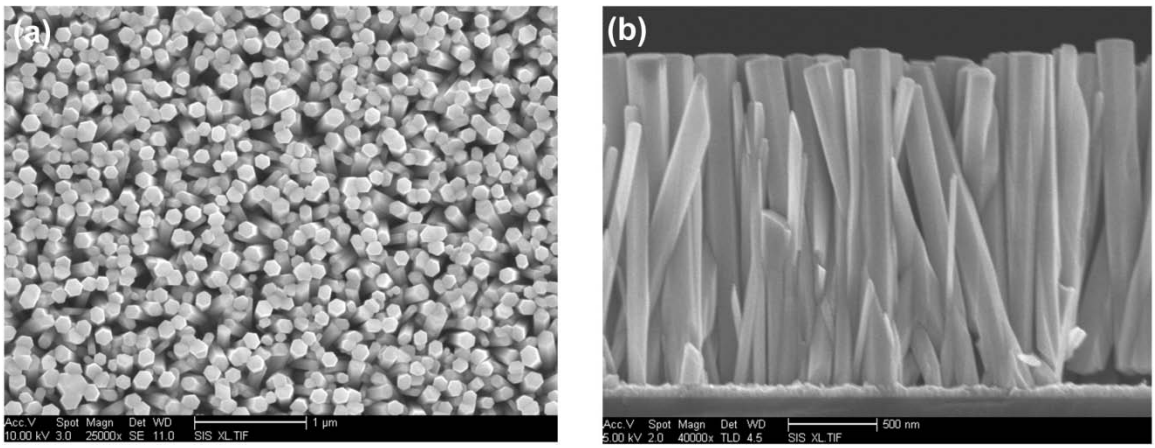

Figure 2-8: SEM images of hydrothermal grown ZnO NWs: (a) Top view, (b) Cross-sectional view.

2.3.2 ZnO thin film growth

ZnO thin film can be synthesized through a two-step hydrothermal growth. A c-sapphire is used as substrate for ZnO thin film growth. In the first step, 2% aluminum doped ZnO (AZO) film is sputtered on the c-sapphire as a seeding layer. The thickness of AZO film is 40nm. A normal ZnO NW array growth is conducted, but with less growth period of 1 hour. The use of AZO seeding layer on sapphire is found to give NWs more vertically aligned as shown in Figure 2-9a. The sample is then taken out of the reactor, and rinsed by DI water. Fresh reaction solution is prepared, with 0.25 mM zinc acetate

and HMTA respectively, and 0.1 mM copper acetate. The sample is put back into growth condition again with fresh solution for another hour growth. Large scale crystalline ZnO thin film with smooth surface is obtained as shown in Figure 2-9b.

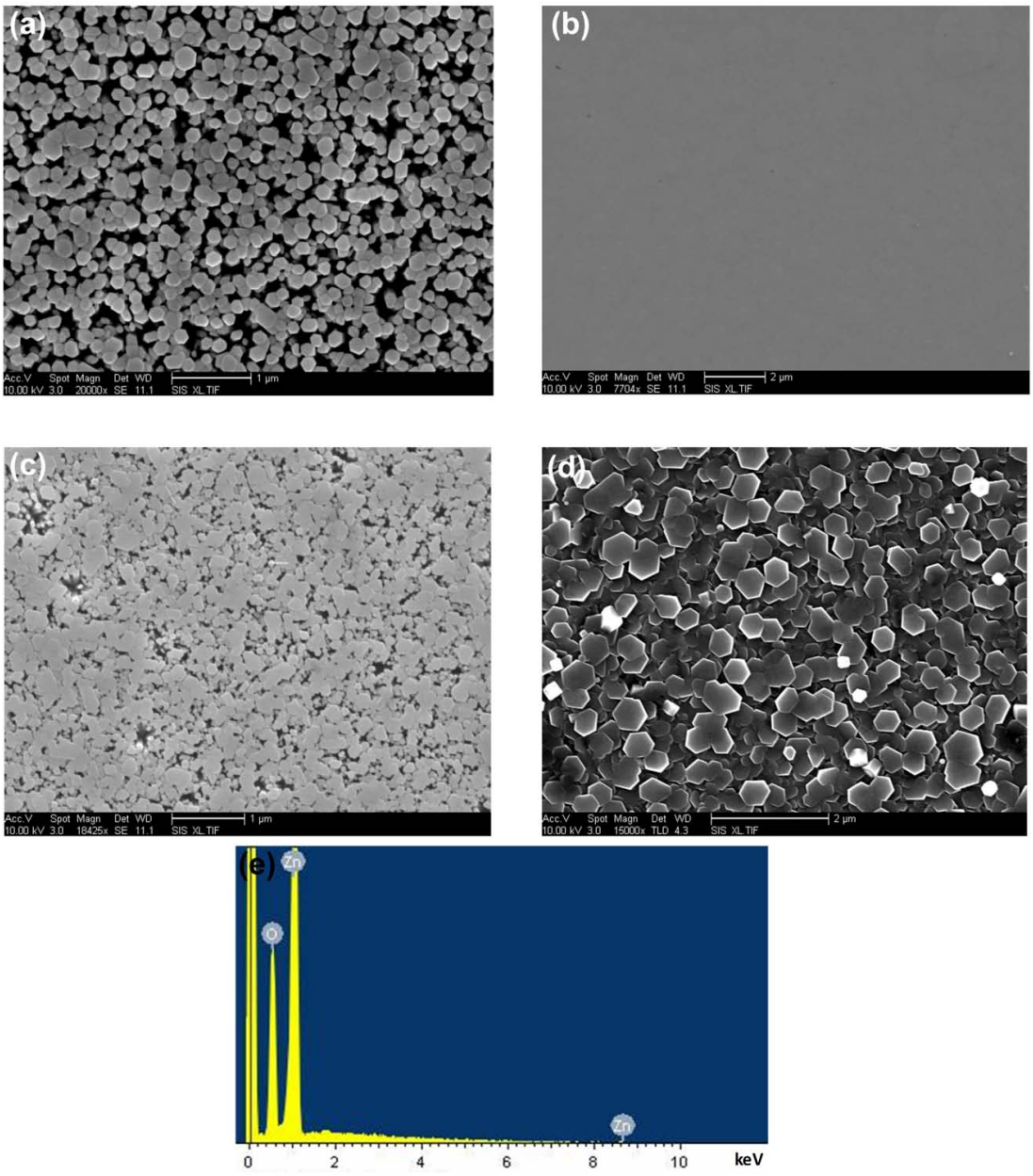

Figure 2-9: SEM images of ZnO thin film from hydrothermal growth. (a) ZnO NW arrays with AZO seeding on sapphire, (b) ZnO thin film after two-step growth, (c) ZnO thin film growth in step two for 30 mins, (d) ZnO thin film growth in step two with 0.5 mM copper acetate, (e) EDX of ZnO thin film.

Copper acetate plays an important role in the ZnO thin film formation during growth step two. In order to have thin film with smooth surface, the already formed NWs in step one need to be coalesced laterally, which means the preferred vertical growth along the c axis has to be inhibited, and the lateral growth needs to be promoted. The function of copper ions is to stick onto the top (0002) surface of NWs, keep the zinc ion species from the top face, while force them to precipitate on the sidewalls.[21] Figure 2-9c clearly shows the merging process of ZnO NWs. However, if over amount of copper ions are adding to the solution, the lateral growth becomes too strong, which causes very rough surface as shown in Figure 2-9d. One thing to point out is that copper ions do not incorporate into the growing ZnO crystal; instead, their presence in the solution primarily leads to crystal growth suppression. This is confirmed by energy-dispersive X-ray spectroscopy (EDX) shown in Figure 2-9e, where only oxygen and zinc peaks exist.

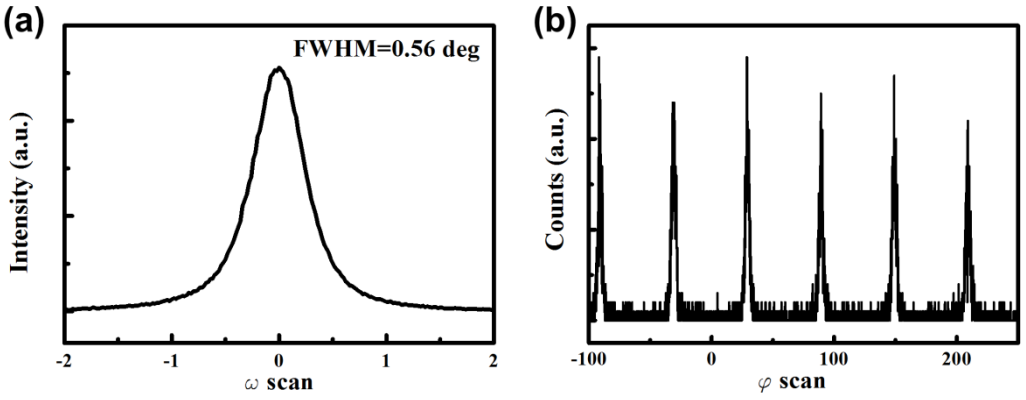

Figure 2-10: XRD measurement of ZnO thin film. (a) Rocking curve, (b) φ scan.

XRD is used to identify the crystal quality of the as-grown ZnO thin film. The (0002) ω scan rocking curve shows a full width half maximum (FWHM) of 0.56 º, which indicates good crystal quality with low defects level (Figure 2-10a). The φ scan shows six

major peaks, corresponding to six equivalent $\{01\bar{1}0\}$ planes, which confirms single crystal wurtzite structure of ZnO thin film (Figure 2-10b).

2.4 GaN growth on solution synthesized ZnO thin film

GaN and ZnO have the same crystal structure and similar lattice constant, which make ZnO very appealing as substrate for GaN epi-growth.[22-24] Based on the successful demonstration of the single crystalline ZnO thin film from solution growth, InGaN/GaN MQW MOCVD growth on solution synthesized ZnO thin film is exploited.

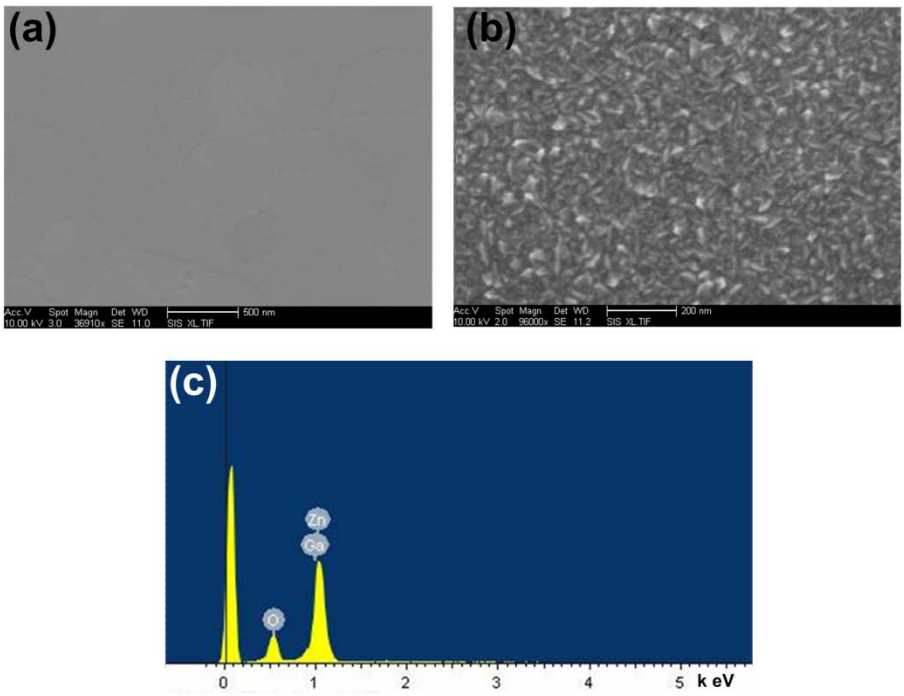

Figure 2-11: (a) SEM image of ZnO thin film before GaN growth. (b) SEM image of sample after LT GaN growth. (c) EDX of sample after LT GaN growth.

A multi-step growth method is used to grow GaN/MQWs on ZnO. First, a low temperature (LT) GaN growth is conducted with a reactor temperature of 550 ºC and for 15 minutes in nitrogen carrier gas. Nitrogen is used, instead of hydrogen, as carrier gas to minimize hydrogen reaction with ZnO at elevated temperature. Here nitrogen is used because hydrogen attacks ZnO at elevated temperature. After the LT growth, the reactor

temperature is raised to 750 ºC for 40 minutes and to 800 ºC for another 10 minutes growth. Furthermore, on the top of high temperature (HT) GaN layer, InGaN/GaN MQWs are subsequently grown with reactor temperature of 700 ºC. TEGa and TMIn are used as precursors for InGaN layer growth, respectively.

Each of the growth are characterized by examination of the structures after the growth, namely samples with growth terminated after each step are studied. Figure 2-11a and b show SEM images of sample before and after LT GaN growth. There are pyramid-like structures at the sample surface, which are typically observed in LT GaN nucleation layer. EDX shows both Zn and Ga peaks, indicating GaN are successfully grown on ZnO (Figure 2-11c).

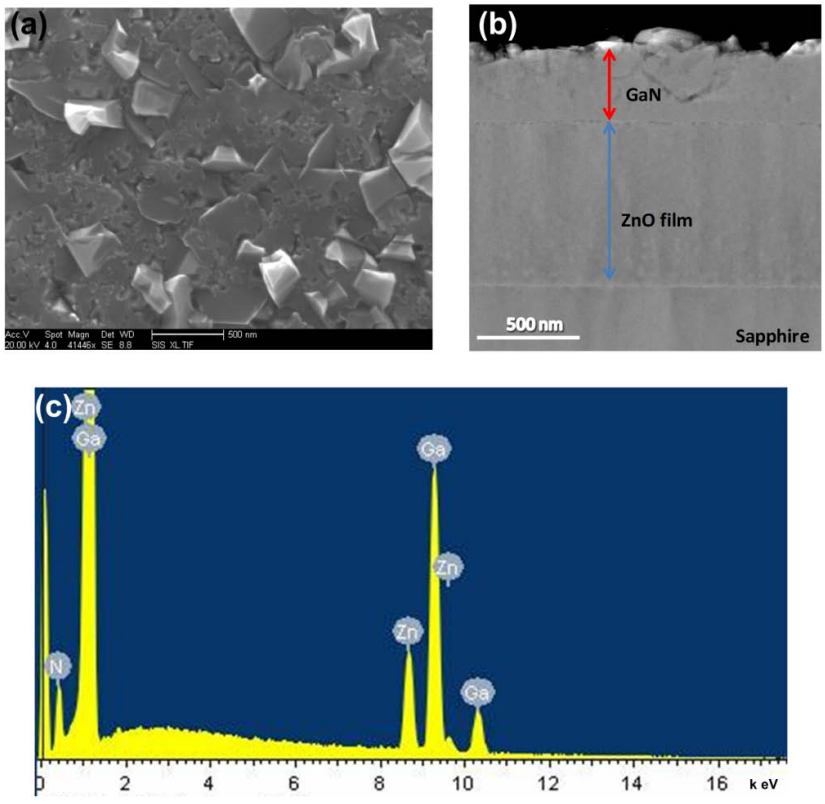

Figure 2-12: (a) SEM image of sample surface after HT GaN growth. (b) Cross-sectional view SEM image of sample. (c) EDX of sample after HT GaN growth.

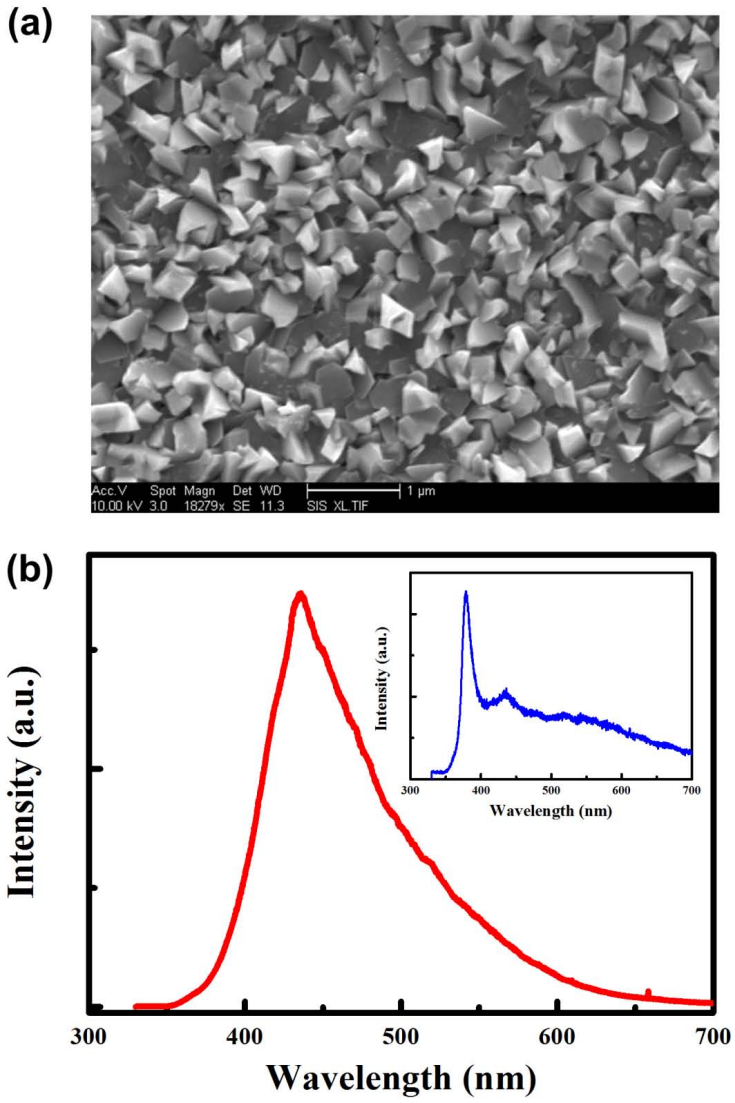

Figure 2-13: (a) SEM image of InGaN/GaN MQWs grown on ZnO film. (b) PL spectrum of InGaN/GaN MQWs on ZnO. Inset showing PL spectrum of GaN on ZnO.

Figure 2-12a shows the top view SEM image of sample surface after HT GaN growth. The cross-sectional SEM image (Figure 2-12b) indicates a clear boundary between ZnO and GaN epi-layer. EDX also shows both Zn and Ga peaks, confirming that ZnO has remained (Figure 2-12c). Figure 2-13a shows the SEM image of InGaN/GaN MQWs grown on ZnO thin film. Rough surface is obtained probably due to the low growth temperature. Photoluminescence (PL) measurement is done by exciting the

sample with a 325 nm He-Cd laser. As shown in Figure 2-13b, the InGaN/GaN MQW on ZnO sample demonstrates an emission peak at 430 nm, while the GaN on ZnO has an emission peak at 390 nm, indicating the successful growth of InGaN material.

2.5 Conclusion

In this chapter, MOCVD growth of InGaN/GaN MQW structure is reviewed. XRD and TEM confirm good crystal quality in the MQW region. EL measurement indicates 22% In concentration in the InGaN QW region. Hydrothermal solution growth of ZnO NWs is then discussed. This method promises easy, low cost and large scale nanostructure fabrication. By introducing a two-step growth method, single crystalline ZnO thin film is obtained. The smooth surface of the ZnO thin film is achieved by adding right amount of copper ions into the reaction, which suppress the growth along the c-axis, and promote the lateral growth. In addition, InGaN/GaN epi-growth on solution synthesized ZnO film has been demonstrated by using a multi-step growth method.

In chapter 3, the InGaN/GaN MQW will be used as a platform to develop photoelectrodes for spontaneous solar water splitting and hydrogen fuel generation. ZnO NWs are going to be used as efficient UV light emitters for high efficiency lighting technology, which will be introduced in chapter 4.

2.6 Appendix

In this appendix, the In concentration in the InGaN QWs, the number of MQWs, and their effects on the device photovoltaic behavior are discussed. In order to narrow the bandgap of InGaN QW for better visible light harvesting, high In concentration in the InGaN layer is needed. This is achieved by growing the InGaN QWs at relatively low temperature of 600 ºC. The EL measurement of the grown sample shows a peak at 584 nm (Figure 2-14a), indicating a bandgap of 2.1 eV, which is favored for solar energy harvesting and an estimated In concentration of 35.7% in the InGaN layer by using Equation 2-2. Two kinds of samples are grown with different numbers of InGaN QWs, 3 and 10.

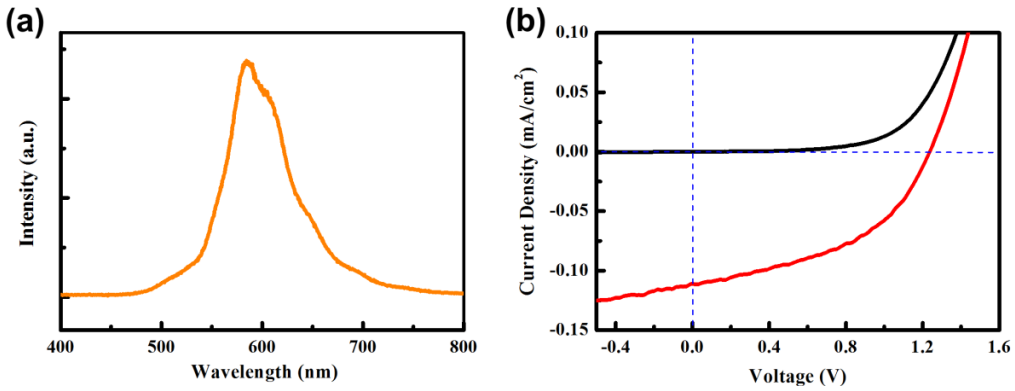

Figure 2-14: (a) EL spectrum of InGaN/GaN MQW sample with high In concentration. (b) Photovoltaic measurement of 3-QW sample.

A semi-transparent top contact of 3 nm Ni/5nm Au is made on samples for photovoltaic measurement. The measurement is done under 1 sun AM 1.5 illumination with a power intensity of 100 mW•cm^{-2}. The 3-QW sample (Figure 2-14b) shows a V_{oc} of 1.24 V and a J_{sc} of 0.11 mA•cm^{-2}, with a solar conversion efficiency of 0.063%. The 10-QW sample is expected to produce large photocurrent due to more InGaN layers, however, the measurement results show very weak photovoltaic effect, with large dark

current (Figure 2-15). The large dark current could be due to the poor confinement of In in the QW region, and thus the In diffusion into the p-GaN and n-GaN region, which constitutes a complete pathway for carrier transport regardless of the GaN p-n junction. On the other hand, the weak photovoltaic effect could be due to the In aggregation of phase separation. The In-rich regions act as deep localized defects, which can pin down the Fermi levels.

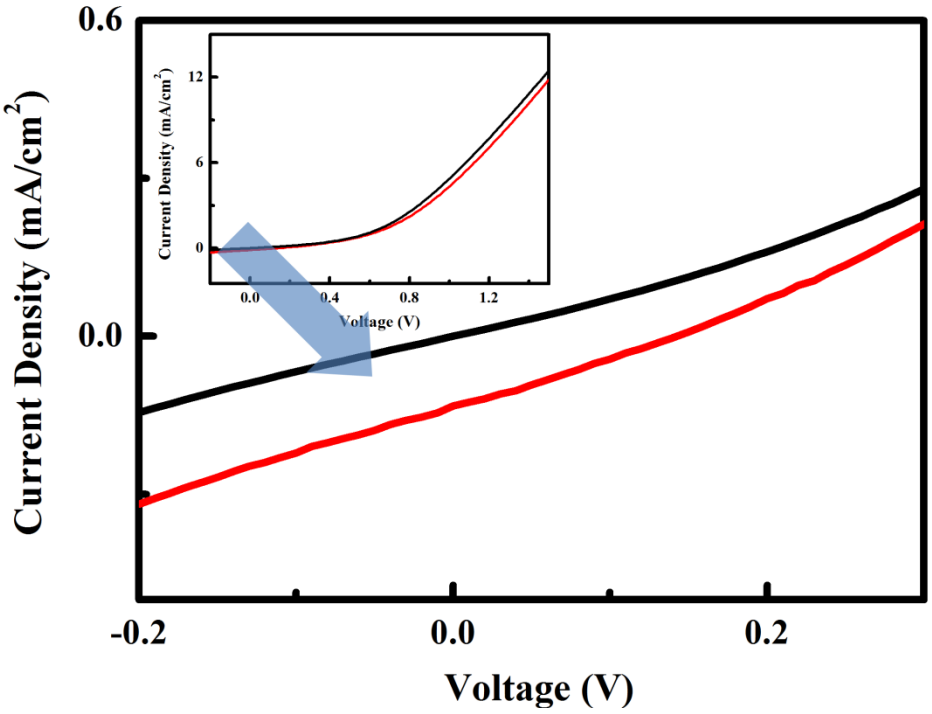

Figure 2-15: Photovoltaic behavior of 10-QW sample at bias of -0.2 V to 0.3 V. Inset shows photovoltaic measurement of 10-QW sample.

To improve the material quality, the growth temperature is elevated to 700 ºC for InGaN QW. The tradeoff would be the lower In concentration, and thus less visible spectrum response. The QW number is kept at 10. Figure 2-16a shows the EL spectrum of as-grown sample, with an emission peak at 470 nm. This corresponds to a bandgap of 2.6 eV and an In concentration of 21%. The photovoltaic measurement (Figure 2-16b)

shows a V_{oc} of 1.55 V and an improved J_{sc} of 0.42 mA•cm^{-2}, with a solar conversion efficiency of 0.26%.

In conclusion, low temperature InGaN growth could lead to In aggregation and phase separation, which degrade the InGaN/GaN MQW photovoltaic effect. High temperature growth leads better material quality and thus improves photovoltaic performance. By having more InGaN QWs, the light absorption is expected to increase, however, meanwhile, some literatures also indicate that the material quality of InGaN layers could get worse by increasing the number of QWs.[25-27]

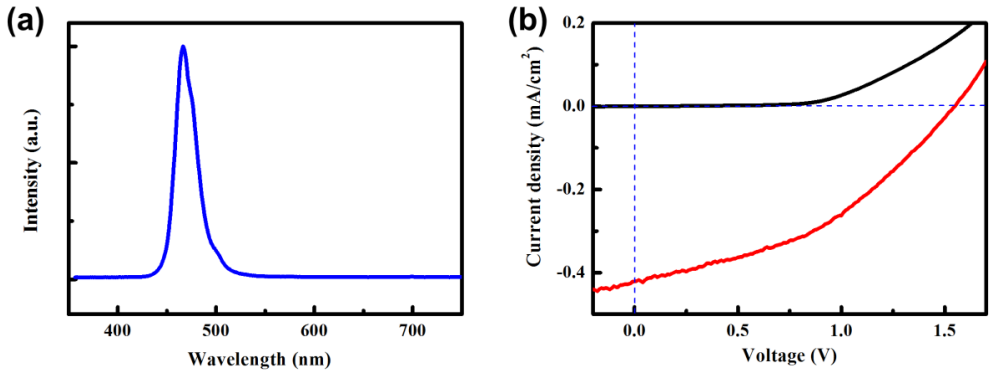

Figure 2-16: (a) EL spectrum of InGaN/GaN MQW sample grown at high temperature. (b) Photovoltaic measurement of 10-QW sample grown at high temperature.

2.7 References

1. Pearton S. GaN and ZnO-based Materials and Devices. Springer Berlin Heidelberg (2012).

2. Nakamura S., Pearton S., Fasol G. The Blue Laser Diode. Springer Berlin Heidelberg (2000).

3. Nakamura S., Senoh M., Nagahama S.-i., Iwasa N., Yamada T., Matsushita T., Sugimoto Y., Kiyoku H. Ridge-geometry InGaN multi-quantum-well-structure laser diodes. *Applied Physics Letters* **69**, 1477 (1996).

4. Jiang H.X., Jin S.X., Li J., Shakya J., Lin J.Y. III-nitride blue microdisplays. *Applied Physics Letters* **78**, 1303 (2001).

5. Muth J.F., Lee J.H., Shmagin I.K., Kolbas R.M., Casey J.H.C., Keller B.P., Mishra U.K., DenBaars S.P. Absorption coefficient, energy gap, exciton binding energy, and recombination lifetime of GaN obtained from transmission measurements. *Applied Physics Letters* **71**, 2572 (1997).

6. Ho I.h., Stringfellow G.B. Solid phase immiscibility in GaInN. *Applied Physics Letters* **69**, 2701 (1996).

7. Reynolds D.C., Litton C.W., Collins T.C. Optical Properties of ZnO. In: *Zinc Oxide Materials for Electronic and Optoelectronic Device Applications*. John Wiley & Sons, Ltd (2011).

8. Schmidt-Mende L., MacManus-Driscoll J.L. ZnO – nanostructures, defects, and devices. *Materials Today* **10**, 40 (2007).

9. Yan R., Gargas D., Yang P. Nanowire photonics. *Nature Photonics* **3**, 569 (2009).

10. Zhu D., Wallis D.J., Humphreys C.J. Prospects of III-nitride optoelectronics grown on Si. *Reports on Progress in Physics* **76**, 106501 (2013).

11. Nakamura S., Iwasa N., Senoh M., Mukai T. Thermal Annealing Effects on P-Type Mg-Doped GaN Films. *Japanese Journal of Applied Physics* **31**, (1992).

12. Nakamura S., Iwasa N., Senoh M., Mukai T. Hole Compensation Mechanism of P-Type GaN Films. *Japanese Journal of Applied Physics* **31**, (1992).

13. Yen-Lin L., Chuan-Pu L., Yung-Hsiang L., Tao-Hung H., Ray-Ming L., Dong-Yuan L., Zhao-Xiang P., Tai-Yuan L. Origins of efficient green light emission in phase-separated InGaN quantum wells. *Nanotechnology* **17**, 3734 (2006).

14. Cho H., Lee J., Kim C., Yang G. Structural and optical investigation of InGaN/GaN multiple quantum well structures with various indium compositions. *Journal of Electronic Materials* **30**, 1348 (2001).

15. McLaughlin D.P., Pearce J. Progress in Indium Gallium Nitride Materials for Solar Photovoltaic Energy Conversion. *Metallurgical and Materials Transactions A* **44**, 1947 (2013).

16. Vayssieres L. Growth of Arrayed Nanorods and Nanowires of ZnO from Aqueous Solutions. *Advanced Materials* **15**, 464 (2003).

17. Greene L.E., Law M., Goldberger J., Kim F., Johnson J.C., Zhang Y., Saykally R.J., Yang P. Low-Temperature Wafer-Scale Production of ZnO Nanowire Arrays. *Angewandte Chemie International Edition* **42**, 3031 (2003).

18. Sun K., Wei W., Ding Y., Jing Y., Wang Z.L., Wang D. Crystalline ZnO thin film by hydrothermal growth. *Chemical Communications* **47**, 7776 (2011).

19. Greene L.E., Yuhas B.D., Law M., Zitoun D., Yang P. Solution-Grown Zinc Oxide Nanowires. *Inorganic Chemistry* **45**, 7535 (2006).

20. Yamabi S., Imai H. Growth conditions for wurtzite zinc oxide films in aqueous solutions. *Journal of Materials Chemistry* **12**, 3773 (2002).

21. Joo J., Chow B.Y., Prakash M., Boyden E.S., Jacobson J.M. Face-selective electrostatic control of hydrothermal zinc oxide nanowire synthesis. *Nature Materials* **10**, 596 (2011).

22. Chung K., Lee C.-H., Yi G.-C. Transferable GaN Layers Grown on ZnO-Coated Graphene Layers for Optoelectronic Devices. *Science* **330**, 655 (2010).

23. Yu H., Wang S., Li N., Fenwick W., Melton A., Klein B., Ferguson I. MOVPE growth of AlGaN/GaN superlattices on ZnO substrates for green emitter applications. *Journal of Crystal Growth* **310**, 4904 (2008).

24. Rogers D.J., Hosseini Teherani F., Ougazzaden A., Gautier S., Divay L., Lusson A., Durand O., Wyczisk F., Garry G., Monteiro T., Correira M.R., Peres M., Neves A., McGrouther D., Chapman J.N., Razeghi M. Use of ZnO thin films as sacrificial templates for metal organic vapor phase epitaxy and chemical lift-off of GaN. *Applied Physics Letters* **91**, (2007).

25. Kim D.-J., Moon Y.-T., Song K.-M., Choi C.-J., Ok Y.-W., Seong T.-Y., Park S.-J. Structural and optical properties of InGaN/GaN multiple quantum wells: The effect of the number of InGaN/GaN pairs. *Journal of Crystal Growth* **221**, 368 (2000).

26. Myung Goo C., Suh E.K., Lee H.J. High-quality In 0.3 Ga 0.7 N/GaN quantum well growth and their optical and structural properties. *Semiconductor Science and Technology* **16**, 783 (2001).

27. Yam F.K., Hassan Z. InGaN: An overview of the growth kinetics, physical properties and emission mechanisms. *Superlattices and Microstructures* **43**, 1 (2008).

Chapter 3

InGaN/GaN MQW PEC Cell

3.1 Introduction

This section starts with an introduction of the principles of PEC cell, followed by a discussion on the essential components in PEC measurement setup, and ends up with a summary of the studies on photoanode materials, such as metal oxides, silicon, III-V compounds, and III-nitrides are reviewed.

3.1.1 PEC water splitting reactions

The concept of PEC water splitting for hydrogen production has been investigated for decades, with first demonstration in 1972 by Fujishima and Honda[1]. As one example, the light-driven water splitting reactions can be written in terms of the H^+ ionic exchange between anode and cathode in the acidic electrolyte solutions:

$$2h\nu \rightarrow 2e^- + 2h^+ \qquad \textbf{3-1}$$

$$H_2O + 2h^+ \rightarrow 2H^+ + 1/2\,O_2 \qquad \textbf{3-2}$$

$$2H^+ + 2e^- \rightarrow H_2 \qquad \textbf{3-3}$$

$$\Delta G^\circ = +237.18 kJ/mol \qquad \textbf{3-4}$$

$$V_{rev} = \Delta G^\circ / nF = 1.23V \qquad \textbf{3-5}$$

$$V_{op} = V_{rev} + \eta_c + \eta_a + \eta_\Omega \qquad \textbf{3-6}$$

Here hν is the photon energy, ΔG° is the standard Gibbs free energy, V_{rev} is the standard reversible potential, F is Faraday's constant, and n (=2) is the number of

electrons exchanged. V_{op} is the operational voltage, η_c , η_a , η_Ω are overpotentials associated with cathode, anode, and conductivity, respectively. Alternatively, the two half reactions can also be written in terms of OH^- ionic exchange in basic solution:

$$2OH^- + 2h^+ \rightarrow H_2O + 1/2\,O_2 \qquad \textbf{3-7}$$

$$2H_2O + 2e^- \rightarrow 2OH^- + H_2 \qquad \textbf{3-8}$$

The specific reaction pathways depend on the nature electrodes, electrolyte and other real conditions. However, the standard Gibbs free energy change of +237.2kJ/mol and the standard reversible potential of PEC water splitting of 1.23V are independent of the reaction pathways, and indicating the thermodynamic minimum energy needed for splitting water into gases under standard condition of 25ºC and 1bar. In real situation, all PEC systems will have losses as those represented in various overpotential terms in the equations. Therefore, the energy needed to split water will inevitably exceed 1.23V. In practice, the energy required for water splitting at a semiconductor photoelectrode is frequently reported as 1.6-2.4 V,[2] depending on gas production rate.

3.1.2 Single junction PEC cell

Figure 3-1 illustrates fundamental processes in a single junction PEC system containing a semiconductor photoanode and a metal cathode. Under solar illumination, photons ($h\nu$) are absorbed in the semiconductor, and generate electron (e^-) and hole (h^+) pairs. The photogenerated electrons and holes are then separated by a built-in electric field due to the formation of the rectifying junction at the semiconductor/electrolyte interface. In photoanode case, holes will be driven by the built-in field toward the semiconductor/electrolyte interface, where, with appropriate energetic and kinetic

conditions, they can drive oxygen evolution reaction (OER). Simultaneously, electrons travel in an opposite direction, through an electrical connection to the counter electrode to promote hydrogen evolution reaction (HER).

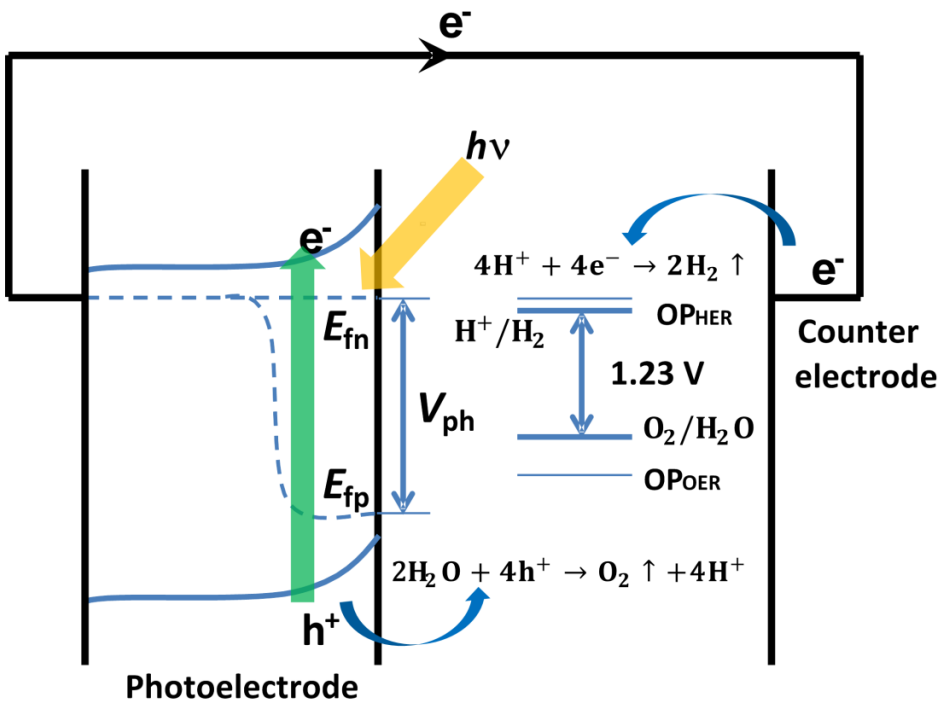

Figure 3-1: Fundamental processes in a two-electrode PEC system.

The rectifying junction at the semiconductor/electrolyte junction is the actual driving force for PEC water splitting. It is similar to the solid-state p-n junction or Schottky junction, which are widely used in photovoltaic (PV) cells. These rectifying junctions generate built-in electric fields, which are capable of separating photogenerated carriers. In PV cells, the separation process drives photocurrent to produce electricity, while in the PEC cells, the charge separation drives both OER and HER half reactions to split water.

During the charge generation and separation, there is an extremely important concept called the photovoltage (V_{ph}) or the useable potential for a PEC cell. With the

absorption of sunlight in the semiconductor, the thermal equilibrium condition breaks, due to the excess concentration of photogenerated electron-hole pairs. The original Fermi level splits into separate quasi-Fermi levels for electrons and holes. The photovoltage in the semiconductor is the potential difference between the quasi-Fermi levels of electrons ($E_{f,n}$) and holes ($E_{f,p}$) under illumination. The maximum value of photovoltage that can be obtained is determined by the barrier height of the rectifying junction.

The photovoltage is the actual energy that can be extracted from semiconductor, and directly determines if spontaneous water splitting could happen. For example, it is often reported that the band edge positions of a single junction semiconductor photoelectrode must straddle with the redox potentials, in order to split water. However, this is by no means a sufficient condition for water splitting. Figure 3-2 shows the band edge positions of several most common PEC semiconductors relative to redox potentials. For wide bandgap semiconductors, such as TiO_2, ZnO, and GaN, the band edges of these materials all straddle with the redox potentials. However, none of them have demonstrated spontaneous PEC water splitting. It is because that the photovoltages or the usable potentials generated from these semiconductors do not meet the thermodynamic energy requirement in addition to other overpotential losses.

As a result of spontaneous emission, non-radiative recombination, and non-ideal band structure alignment, the available photovoltage is always less than the bandgap of the semiconductor. To achieve sufficient high photovoltage to drive both half reactions simultaneously, for a single semiconductor photoelectrode, the bandgap over 3 eV is typically required. However, such a wide bandgap will severely limit the solar energy

harvesting. For practical spontaneous (unassisted) water splitting, the photovoltage must be larger than the energy required in the actual situation, in other words, the photovoltage

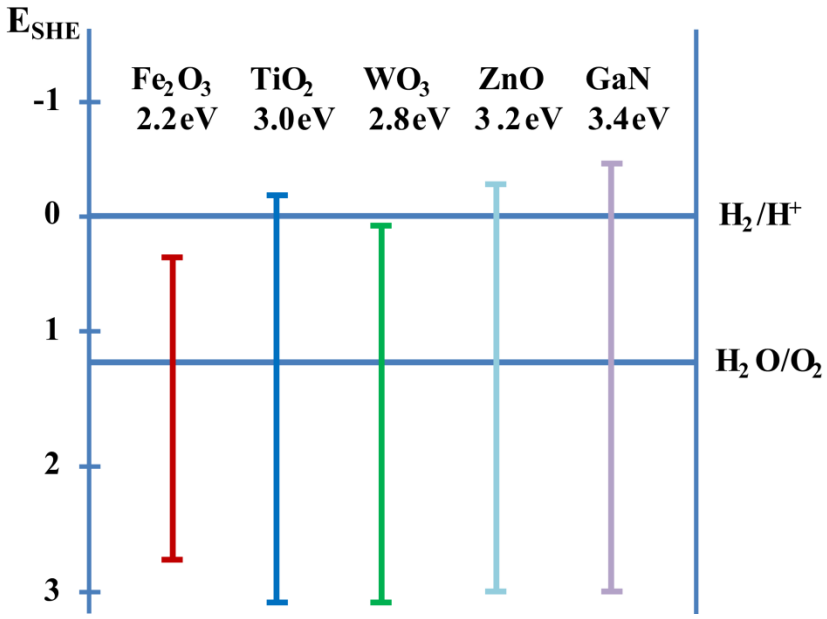

Figure 3-2: Band edge positions of several common PEC semiconductors relative to the redox potentials vs. the standard hydrogen electrode (SHE).

must enable the quasi-Fermi levels under illumination to straddle the OER and HER redox potentials plus overpotentials.

3.1.3 PEC solar-to-hydrogen conversion efficiency

Practical PEC cells consist of two electrodes immersed in the electrolyte and a bias is applied between the working photoelectrode and counter electrode. The efficiency of such configuration (assuming no corrosion reaction at the photoelectrode) can be calculated from:

$$\eta_{abce} = \frac{J \times (1.23 - V_{bias})}{P_{in}} \qquad \textbf{3-9}$$

where V_{bias} is the applied voltage between anode and cathode, J is the externally measured current density, and P_{in} is the input power density. For spontaneous solar water

splitting, where the sunlight is the only energy source, the true solar-to-hydrogen (STH) conversion efficiency can be calculated by using photocurrent J_{ph} at V_{bias} = 0 V (short-circuit condition). Based on idealized cases where 100% of the photons in the solar spectrum with energies exceeding the bandgap are absorbed and converted, theoretical STH and solar photocurrent of a photoelectrode under AM 1.5G irradiation (100 mW•cm^{-2}) are displayed in Figure 3-3.[3]

It is clear that the photocurrent density is the key factor that influences the conversion efficiency. This is different from the solid-state PV cells, which operate at the maximum power point (the maximum of photovoltage and photocurrent), for the highest solar-to-electric conversion. In PEC cells, it is the bandgap-limited saturated photocurrent density that defines the ultimate hydrogen production rate.

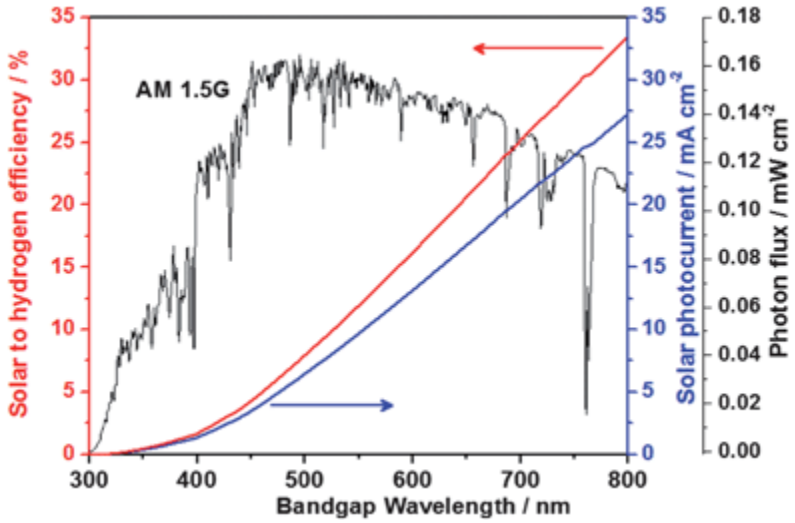

Figure 3-3: Dependence of theoretical STH and solar photocurrent density of photoelectrodes on their absorption edges under AM 1.5G irradiation (100 mW•cm^{-2}).[3]

However, in practice, it is difficult to obtain high STH conversion efficiency in single junction photoelectrode PEC cells with the existence of fundamental conflicts in trying to achieve photocurrent density and photovoltage as high as possible at the same

time. Wide bandgap semiconductor materials would be needed to provide sufficient photovoltage or usable potential to split water. This, however, can severely limit the solar energy harvesting and reduce the photocurrent and the STH conversion efficiency. For instance, in certain photoelectrode PEC system, it requires photovoltage amounts to be 1.8 V to achieve spontaneous water splitting. Even for high quality semiconductor materials, the quasi-Fermi level separation can only be 50-70% of the bandgap, which means that the minimum bandgap for the onset of solar water splitting for this photoelectrode would be 2.6-3.6 eV. The optical absorption limit due to the semiconductor bandgap sets an upper bound for STH conversion efficiency, which in this case, could be well below 1% as indicated in Figure 3-3. On the other hand, strictly speaking, any semiconductor photoelectrodes incapable of generating sufficient photovoltage will not be able to sustain solar water splitting, and thus cannot produce photocurrent and will have 0% STH conversion efficiency.

3.1.4 PEC measurement setup

In order to investigate the properties and performance of photoelectrodes, the PEC measurement setup requires several components: the reference electrode, the counter electrode, electrolyte, potentiostat, and solar simulator.

When studying the properties of the working photoelectrode, the applied potential is a key parameter. The potential should be measured with respect to a fixed reference potential, so that any change in the applied potential reflects a change in the working electrode alone. Therefore, a reference electrode is applied. The applied potentials are usually reported against the reversible hydrogen electrode (RHE) scale for PEC water splitting studies. Zero volt on the RHE scale reflects the HER potential in the actual

solution, irrespective of the pH. In my study, two reference electrodes are used. Silver/silver chloride (Ag/AgCl) electrode is used for nearly neutral electrolyte (pH=7.2), and mercury/mercury oxide (Hg/HgO) electrode for alkaline electrolyte (pH=14). Potentials measured with respect to reference electrodes can be converted to the RHE. For Ag/AgCl reference electrode with 1M saturated KCl, the RHE can be calculated with the following expression:

$$E(REH) = E(Ag/AgCl) + 0.197 + 0.059 \times pH \qquad \textbf{3-10}$$

Here, 0.197 V is the potential of the Ag/AgCl reference electrode with respect to the standard hydrogen potential (SHE). Similarly, for Hg/HgO reference electrode, the RHE can be obtained with expression:

$$E(RHE) = E(Hg/HgO) + 0.14 + 0.059 \times pH \qquad \textbf{3-11}$$

where 0.14 V is the potential of the Hg/HgO reference electrode with respect to the SHE.

In a PEC system with a photoanode as the working electrode, the material for counter electrode or the cathode is typically Pt, which combines good chemical stability with very small overpotential for HER (~ 0.1V). In our PEC setup, a coiled Pt wire electrode is used.

In PEC water splitting, the electrolyte is a solvent in which the active species are reduced or oxidized. Since pure water is poor conductor, supporting ions are usually added to ensure that the desired current flow can be attained. The concentration of the electrolyte should be sufficiently high to avoid large voltage loss across the electrolyte. However, the use of high pH solvent as electrolyte is often dangerous and not environmentally safe, therefore, using nearly neutral solutions and developing photoelectrodes which can efficiently split them is very desirable. In our study, two kinds

of electrolytes are used: 0.25 M Na_2SO_4 electrolyte buffered with PBS (phosphate buffered saline solution) with pH =7.2, and 1M NaOH electrolyte with pH =14.

The potentiostat is the central component in every PEC setup. Usually, the potentiostat has three test leads to be connected to the PEC cell. The three leads are for the working, counter and reference electrodes. The aim of the potentiostat is: it measures the potential difference between the reference and working electrodes, and makes sure that it stays equal to the desired potential difference by adjusting the potential at the counter electrode.

The potential reported by the potentiostat corresponds to the measured potential difference between the reference and working electrodes. Therefore, in PEC measurement, when we are trying to understand the processes that take place at the photoelectrode (working electrode), we use the three-electrode measurement configuration. In this case, the counter electrode only serves to supply the voltage and current to keep the potential difference between reference and working electrodes at the desired value. In contrast, in order to study the real STH conversion efficiency of a PEC cell, two-electrode measurement configuration must be used, in which the reference and counter electrodes leads have to be tied together to measure the potential difference between the working and counter electrodes.

Solar simulator is another central component in PEC measurement setup, because the main figure-of-merit for a PEC solar water splitting device is its performance under real sunlight. To facilitate meaningful comparisons between devices, the performances are typically quoted for the so called AM 1.5G condition, which stands for “air mass 1.5 global”, and refers to the spectral distribution and intensity of sunlight on a 37^{o} south-

facing tilted surface after it has traveled through 1.5 times the thickness of the earth's atmosphere. The AM 1.5G spectrum has a total integrated intensity of 100 mW•cm^{-2}. Since real AM 1.5G sunlight is not readily available at all times and at all locations, solar simulators are used in the experiment.

In our measurement, the electrochemical behavior of samples is measured using Digi-Ivy DY2300 potentiostat. A xenon lamp from a solar simulator with a AM 1.5 filter provides an output light intensity of 100 mW•cm^{-2}. Figure 3-4 shows the images of potentiostat, solar simulator and the schematic of PEC setup. All data are recorded using DY2300 software.

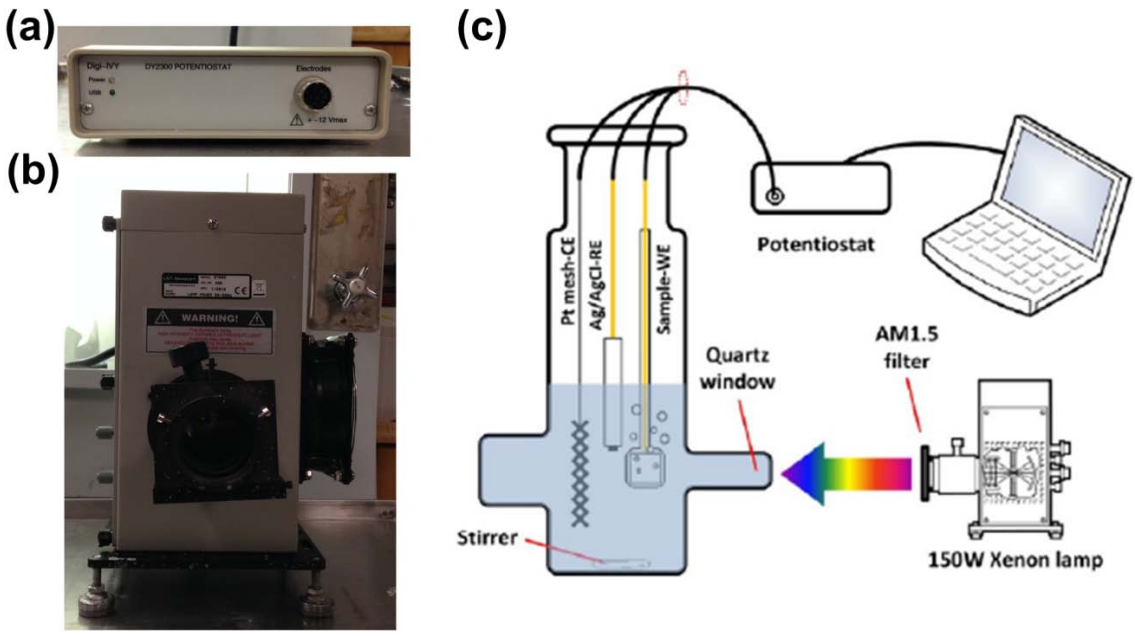

Figure 3-4: (a) Digi-Ivy DY2300 potentiostat. (b) Solar simulator. (c) Schematic of PEC measurement setup (courtesy of Ke Sun).

3.1.5 Photoanodes for water splitting

As shown in Figure 3-1, for water splitting, metal counter electrode, typically Pt is used as cathode for HER due to its high stability in various conditions and low

overpotential to reduce water. On the other hand, water oxidation and oxygen generation is a more complex and challenging process, therefore, a lot of research effort has been focused on photoanodes for OER. Generally speaking, for single bandgap semiconductor, the photoanode material must be an n-type semiconductor, such that the electric field generated by band bending (rectifying junction) drives holes toward the semiconductor/electrolyte interface. The bandgap of the material should be narrow enough for efficient absorption of visible light and the band edge positions have to be suitable for OER and HER. Additionally, the material needs to be stable under water against photocorrosion (oxidation). However, since the width of the bandgap is a measure of the chemical bond strength, semiconductors stable under illumination, are typically wide bandgap materials, such as metal oxides, which mainly respond in the UV region and are insensitive to the visible spectrum. The integration of these conflicting properties in a photoanode proves to be extremely difficult. In the following sections, I will discuss photoanodes based on several different material systems for oxygen evolution and solar water splitting.

3.1.6 Metal oxides as photoanodes

Because of the requirement of stability under oxidizing conditions, the most popular photoanode materials that have been investigated are metal oxides[4], such as TiO_2, Fe_2O_3, WO_3, $SrTiO_3$. TiO_2 is the most actively studied photoanode material for PEC water splitting and hydrogen generation. People are so interested in TiO_2 because it is considered more stable against photocorrosion among the available photoelectrode semiconductors. TiO_2 exists in three phases, brookite, anatase and rutile, with rutile as the most stable phase, and a bandgap of 3 eV. The wide bandgap could be one drawback that

limits the solar light absorption and photocurrent, but, the actual fatal weakness is that even with this large bandgap, the maximum obtained photovoltage of TiO_2 photoanode is only ~ 0.9 V, insufficient to sustain spontaneous water splitting. Consequently, TiO_2 photoanode based PEC cells often require an external bias.

α- Fe_2O_3, hematite, has been a material of interest in PEC water splitting for long time.[5, 6] It has a bandgap of 2.2 eV hence is one of the most attractive photoanode materials for harvesting solar energy for hydrogen production. Moreover, α- Fe_2O_3 is stable in most electrolytes over a wide range of pH. Unfortunately, despite these advantages, it is labeled as a poor photoanode mainly due to its band edges not being properly aligned to the redox levels of HER and OER.[7] Other shortcomings, such as a short hole diffusion length, short lifetime of charge carriers and poor mobility of charge carriers, also hinder α- Fe_2O_3 from being efficient photoanode for water splitting.[6, 8-10]

Tungsten trioxide, WO_3, has also been applied as photoanode material for PEC water splitting.[11] However, it suffers from several weakness such as indirect optical transition, short hole diffusion length, and stability issue in some electrolytes. To date, demonstrations of single junction water splitting have utilized very large bandgap materials such as $SrTiO_3$ and $KTaO_3$.[12, 13] Because of the low light absorption, the STH conversion efficiency is typically well below 1%. To extend the photoresponse of $SrTiO_3$ photoanodes into longer wavelength, various transition metal ions have been tried to dope the single crystal $SrTiO_3$.

3.1.7 Silicon and III-V compound semiconductor photoanodes

Silicon and III-V semiconductors are important materials in the electronics industry, because of their earth abundance. They also attract amount of attention as

photoanode materials for PEC water splitting since they are excellent light absorbers with high carrier mobilities.[14, 15] However, they are extremely prone to anodic photocorrosion. Surface passivation layers have to be added to suppress or retard photocorrosion.[16] Such additional processes significantly increase manufacturing cost, which partially neutralize the advantage of using these materials. Moreover, with the small bandgap, for single junction configuration, photovoltages generated from these materials based photoanodes are generally not enough to sustain water splitting. Typical solution is to build multiple junctions or tandem cells to boost the photovoltage, but could also increase the photoelectrode designing complexity and fabrication difficulty, which eventually leading to high cost.

3.1.8 III-nitrides semiconductor photoanodes

III-nitrides have been the dominant material system for high performance light emitting diodes (LEDs) and laser diodes.[17, 18] Recently III-nitrides, particularly InGaN/GaN alloy, have also gained much attention as photoelectrode materials for PEC applications.[19, 20] First of all, theoretical calculation shows that the band edges of GaN and InGaN (with In content up to 50%) straddle with both the HER and OER potentials, which is crucial to spontaneous water splitting.[21, 22] More importantly, by varying the In content in GaN (E_g = 3.4 eV), the bandgap absorption edge of InGaN could potentially cover the entire solar spectrum for enhanced light harvesting. Compared to other tandem cells, the application of InGaN/GaN should lead to simpler and more cost-effective designs of PEC cell, since it would require only one alloy system.

However, solar water splitting using InGaN/GaN alloys as photoaondes has so far been demonstrated only with limited success, and in most studies, an external bias is

needed to sustain water splitting.[23-26] For example, GaN nanorod photoelectrode[27] showed a maximum efficiency of 0.26% at an external bias of 0.8V in HCl solution (pH=0.1). Si/InGaN branched nanowire photoelectrode showed extremely low anodic current even under bias. The need of bias to sustain water splitting is due to the small bandbending at the S/E interface, which leads to insufficient photovoltage for water splitting. Even though the band edges of the InGaN/GaN alloys straddle with the HER and OER levels, spontaneous water splitting still cannot happen.

3.2 InGaN/GaN MQW photoanodes

3.2.1 Introduction

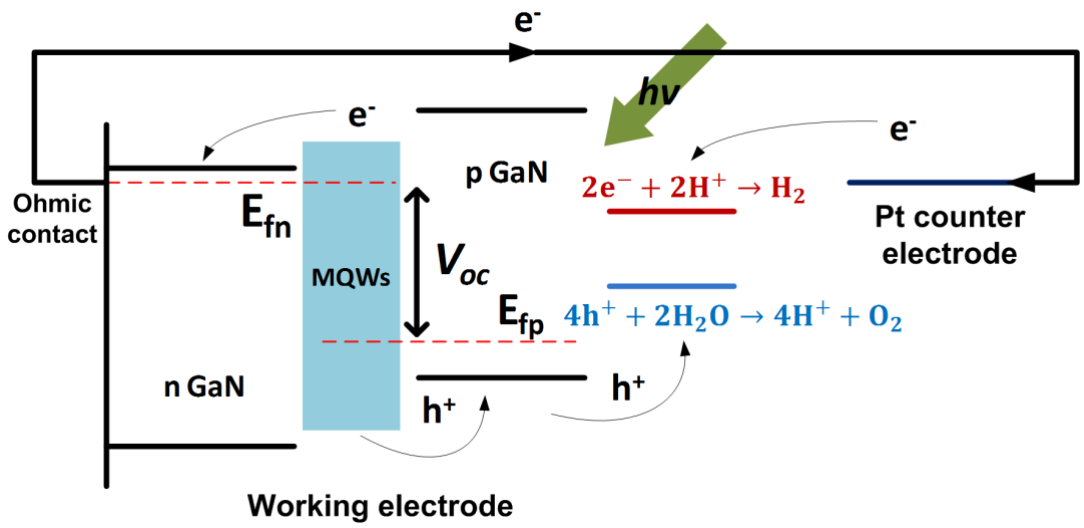

Figure 3-5: Schematic of InGaN/GaN MQW PEC cell for spontaneous water splitting.

Figure 3-5 shows the schematic of InGaN/GaN MQW PEC cell for water splitting. The InGaN/GaN MQW structure is used as a photoanode, and the advantage of applying it is that it allows the decoupling of photovoltage generation, light absorption, and electrochemical reaction and thus relaxes the stringent restrictions for a photoanode material. First of all, the GaN p-n junction could provide sufficient photovoltage to

sustain water splitting. One-dimensional (1D) Poisson simulation (Figure 3-6) indicates that the maximum photovoltage that the GaN p-n junction could provide can be up to 3 eV (based on p/n doping concentration mentioned in chapter 2). This value is much larger than the energy requirement for practical water splitting, which means unassisted spontaneous water splitting is achievable.

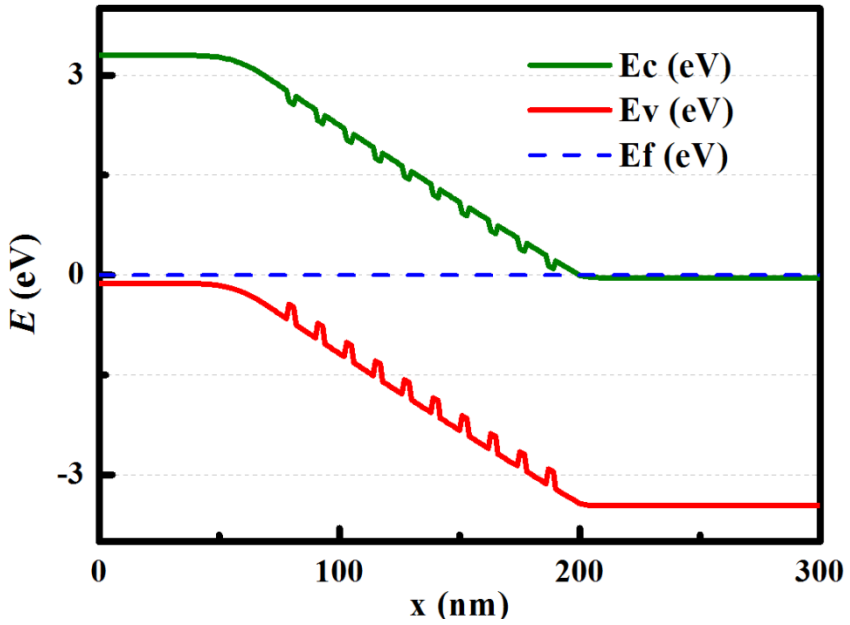

Figure 3-6: 1D Possion simulation of InGaN/GaN MQW band diagram**.**

Second, the absorption can be enhanced by using InGaN/GaN MQWs. InGaN has high absorption coefficient of 10^5 cm^{-1} near the band edge.[28] By applying the ultra-thin QW structure, the InGaN layer can be incorporated with high In content while maintaining good crystal quality.[29] Figure 3-7 shows the absorption spectrum of InGaN/GaN sample with 10 periods of MQWs. The absorption keeps high (> 85%) until 360 nm, which corresponds to the GaN bandgap (3.4 eV), indicating that this high absorption is due to the thick GaN layer. The absorption then shows a quick drop until 450 nm, and very limited value (< 1%) over longer wavelength. From the spectrum, it is

believed that 450 nm (2.75 eV) is the effective absorption edge of the InGaN layers. By combining the absorption spectrum with the solar irradiation spectrum, the theoretical photocurrent density is calculated to be 1.08 mA•cm^{-2}.

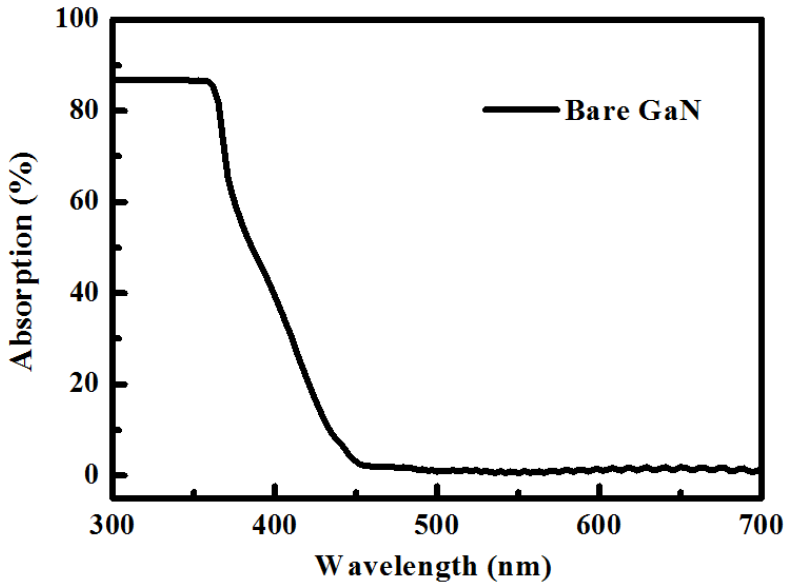

Figure 3-7: Absorption spectrum of InGaN/GaN MQW sample.

Moreover, compared to the single material photoelectrode, the photovoltaic action is decoupled from the electrochemical reaction, which only happens at the p-GaN/electrolyte interface. As shown in Figure 3-5, after the photo-generation in the MQW region, the electron-hole pairs separated by the internal electric field due to the GaN p-n junction. Electrons are swept into the n-GaN layer, which is connected to the Pt counter electrode for hydrogen evolution half reaction. Meanwhile, holes are swept into the p-GaN layer, which is in contact with the electrolyte for oxygen evolution. The significance of this configuration is that photovoltaic energy harvesting and fuel production processes can be individually studied and optimized. Thus, better solar-fuel conversion performance is expected by using InGaN/GaN MQW photoanode.

3.2.2 PEC measurement

The PEC performance of the InGaN/GaN MQW photoelectrodes is measured in a 0.25 M Na_2SO_4 electrolyte buffered with PBS (phosphate buffered saline solution) (pH =7.2) in a three-electrode configuration (with an as-grown InGaN/GaN MQW working electrode, a Pt counter electrode, and a Ag/AgCl, with 1 M KCl, reference electrode).[30, 31] Figure 3-8 shows the *J-V* characteristics of MQW photoanode under different light illumination intensities. Different illumination intensities are applied here to determine whether the measured current is due to light response and it clearly shows that when the light intensity decreases, the current also decreases correspondingly. In dark, a low anodic current density j_{an}< 0.15 μA•cm^{-2} at 2.62 V vs. the reversible hydrogen electrode (RHE) is observed upon scanning from a positive onset potential (E_{onset}) > 1.3 V vs. RHE. The onset potential is defined as the potential at which the current changes from negative (cathodic) to positive (anodic) values. Under 1 sun 1.5 AM illumination, there is a large negative onset potential shift of 1.4 V. Similar to open circuit voltage (V_{oc}) in the PV cell, the onset potential shift ΔE_{onset} is attributed to the difference between electron and hole quasi-Fermi levels in the embedded InGaN/GaN MWQ PV cell. To confirm this point, the performance of corresponding solid-state PV cell is characterized and a V_{oc} of 1.55 V and a short circuit current (j_{sc}) of 0.42 mA•cm^{-2} are obtained (Figure 2-16b). The PV cell and PEC cell shows close V_{oc} and ΔE_{onset}, but both are smaller than the simulated maximum value. This may be due to the pin down of the quasi-Fermi level to the indium-rich regions (aggregates) in the QW, which act as recombination channels[32], or due to the existence of series resistance in neutral electrolyte solution. There is a larger short circuit current from PV cell compared to current density at zero bias from PEC measurement,

which can be due to the reaction limited current because of there is only limited number of OH^- ions and the kinetic loss due to the use of neutral solution. Moreover, the lack of OER catalysts could cause inefficient charge transfer, and thus a low anodic photocurrent. Note that in a typical PEC configuration, the potential band bending formed at this interface (p-GaN/electrolyte) may not favor an ohmic transportation for the energetic holes to the electrolyte. However, when under light illumination, with photogenerated holes being swept into p-GaN region, the Schottky barrier height could be significantly reduced, so holes can overcome or tunnel through the barrier to reach the electrolyte and still contribute to the photocurrent.

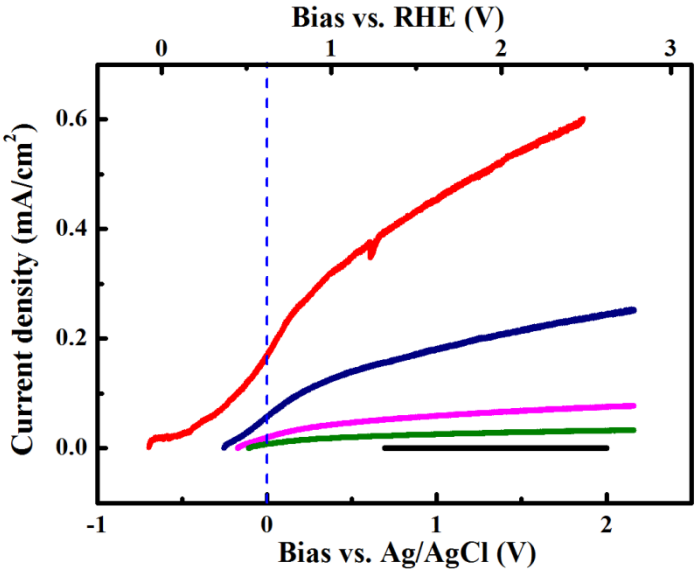

Figure 3-8: *J-V* characteristics of the InGaN/GaN MQW photoanode under various illumination intensities: under dark (black line), under 1 sun 1.5 AM illumination, 100 mW•cm^{-2} (red line), 31.6 mW•cm^{-2} (blue line), 10 mW•cm^{-2} (pink line) and 3.16 mW•cm^{-2} (green line).

In a typical PV cell, the photocurrent density J_L is given by Equation 3-12:[33]

$$J_L = q\int_{E_g}^{\infty} \frac{d\varphi_{ph}}{d(h\nu)} d(h\nu) \qquad \textbf{3-12}$$

where φ_{ph} is the photon flux density, q is the electronic charge 1.6×10^{-19} C. The equation also suggests the linear relationship between photocurrent density and the input light intensity under zero bias. Figure 3-9 plots the anodic current density at zero bias (0.622V vs. RHE) as a function of light intensity. It is found that the photocurrent density decreases almost linearly (from 0.17 mA•cm^{-2} to 7.8 μA•cm^{-2}) when the input light intensity decreases from 100 mW•cm^{-2} to 3.16 mW•cm^{-2}, proving that there is no significant recombination loss in the InGaN/GaN MQW structure and at the p-GaN/electrolyte interface.

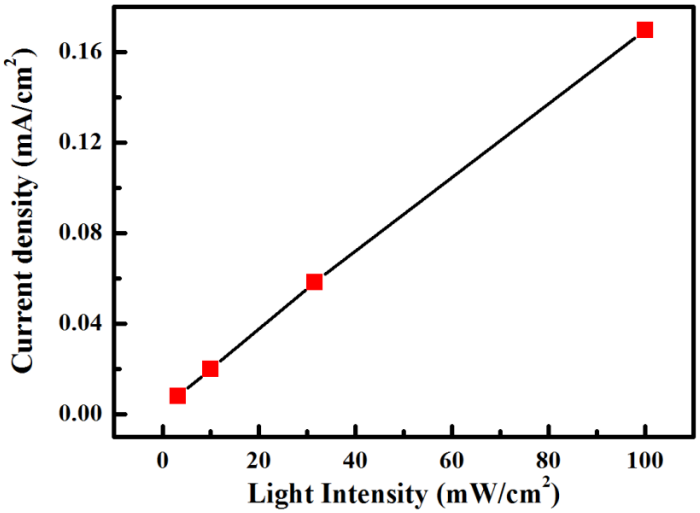

Figure 3-9: Current density at zero bias (0.62 V vs. RHE) versus the light intensity.

To further demonstrate the functional advantages of the MQW structure, we have also studied a 30nm InGaN thin film photoanode. The InGaN photoelectrode has an identical In concentration as in the InGaN layer of MQWs and a comparable total thickness of the active light absorption region (10 InGaN QWs). Figure 3-10 compares the PEC performance of these two photoanodes. Because of the additional PV cell in MQW photoanode, it showed a much sharper increase of the photocurrent compared to

the InGaN film photoanode. The photocurrent (0.17mA•cm^{-2}) at zero bias (blue dashed line) from MQW photoanode was orders of magnitude larger than that from the InGaN film (1.15 μA•cm^{-2}), which suggests that spontaneous solar water splitting is possible using MQW photoelectrode but not using the pure InGaN photoelectrode. Table 3-1 summarizes a detailed comparison of layer structures and PEC performance between the InGaN/GaN MQW and InGaN thin film photoanodes. The lack of built-in rectifying junction in the InGaN film and insufficient band bending at the S/E may lead to the low performance of InGaN film photoelectrode.

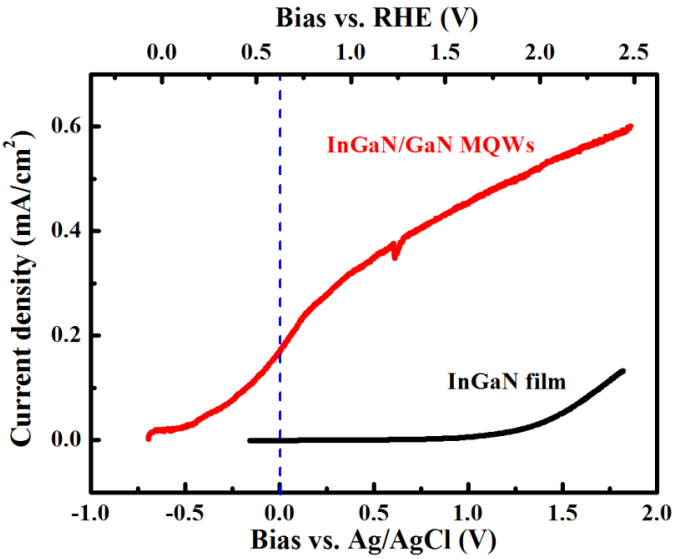

Figure 3-10: *J-V* characteristics of the InGaN/GaN MQW and InGaN thin film photoelectrodes.

The conversion efficiency of the InGaN/GaN MQW photoelectrode for water splitting is measured using a two-electrode configuration. The applied bias conversion efficiency (ABCE) can be calculated from *J-V* data using Equation 3-9. A peak conversion efficiency of 0.2% is obtained at zero external bias with the current density of 0.16 mA•cm^{-2} (Figure 3-11).

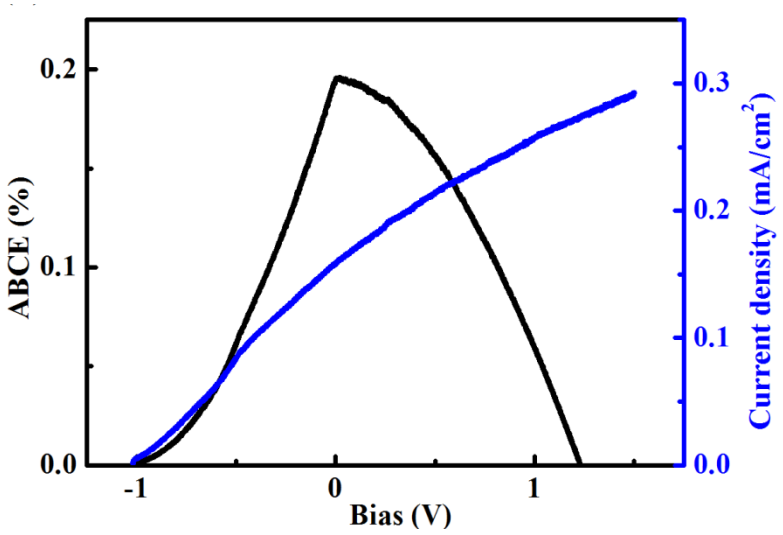

Figure 3-11: Two-electrode measurement of InGaN/GaN MQW photoelectrode.

One issue associated with III-nitride photoelectrodes, which severely hinders them from practical application, is their durability, especially as photoanodes for OER. In our stability test (Figure 3-12); we observe a rapid current density drop of 50% of its initial value in 20 minutes. We attribute this current decay to GaN oxidation and etching.

Table 3-1: Photoelectrodes layer structures and PEC performance.

Photoelectrode	InGaN thin film	InGaN/GaN MQWs
Onset potential shift ΔE_{on} (V)	0.27	1.4
Anodic current density at zero bias (μA•cm^{-2})	1.15	160
Control layers	InGaN ~ 30nm	p GaN, InGaN/GaN (3nm/9nm)×10 MQWs
Common layers	n GaN ~ 1.5μm	
	undoped GaN buffer ~ 1.5μm	
	c-sapphire substrate	

PEC etching of III-nitrides has been reported.[34, 35] Wang calculated the thermodynamic oxidation potentials of various semiconductor materials in aqueous solution, and showed that the oxidation potential of GaN is more negative compared to water oxidation potential (H_2O/O_2), which means GaN, rather than water, may first be oxidized by photogenerated holes.[36] GaN PEC etching process includes two simultaneous chemical reactions of oxide formation and dissolution[37], which can be expressed by the two following equations:

$$2GaN + 6h^+ + 6OH^- \leftrightarrow Ga_2O_3 + 3H_2O + N_2 \uparrow \qquad \textbf{3-13}$$

$$Ga_2O_3 + 6OH^- \rightarrow 2GaO_3^{3-} + 3H_2O \qquad \textbf{3-14}$$

Indeed, Riechert showed that only N_2 signal was detected when InGaN nanowire was used as photoanode.[38] The results indicate that instead of water oxidation, a photo-induced corrosion process and the decomposition of InGaN take place. The stability can be significantly improved by coating the p-GaN with surface protection layer or OER catalysts,[39, 40] which will be demonstrated and discussed in section 3.3.

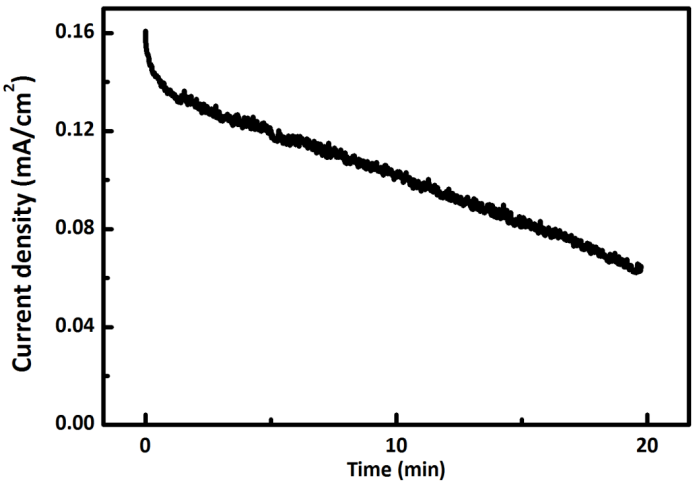

Figure 3-12: Stability test of InGaN/GaN MQW photoelectrode, under zero bias.

3.2.3 Summary

InGaN/GaN MQWs photoanode is designed and fabricated for spontaneous PEC water splitting. The structure allows the decoupling of energy generation, light absorption and electrochemical fuel production, and thus relaxes the stringent restrictions for a photoelectrode material. Specifically, the GaN p-n junction provides sufficient photovoltage to sustain water splitting, while the InGaN/GaN MQWs are responsible for shifting the light absorption to longer wavelength for enhanced solar energy harvesting. Water oxidation takes place at the p-GaN/electrolyte interface, and spontaneous water splitting is demonstrated. At zero external bias, the PEC cell achieves a peak conversion efficiency of 0.2% with current density of 0.16 $mA \cdot cm^{-2}$. This work shows that InGaN/GaN MQW structure has great potential as photoelectrode building block for efficient and low-cost solar water splitting and fuel generation.

3.3 NiO_x|Ni|InGaN/GaN MQW photoanode

3.3.1 Introduction

In this section, a photoelectrode consists of InGaN/GaN MQW and a nickel (Ni) thin film will be introduced, for improved PEC water splitting — more efficient and robust. The InGaN/GaN MQW structure, as demonstrated in section 3.2, offers sufficient photovoltage and photocurrent for spontaneous solar water splitting. The Ni film serves multiple functions: a reflection mirror which enhances the light absorption and photocurrent, and an ohmic contact that improves the transport of photogenerated carriers and reduces internal resistive loss; a protection layer against photoinduced decomposition of GaN, and most importantly, an oxygen evolution reaction catalyst with the formation of nickel oxide (NiO_x) in the alkaline electrolyte. The overall STH conversion efficiency

is 0.64% at zero bias, which is almost two times larger than that of the GaN MQW photoelectrode without Ni coating. The stability of photoelectrode is also much improved and photocurrent reduction of less than 4.5% in 12 hours is achieved.

3.3.2 Electrocatalysts for PEC water splitting

In section 3.2, it has been shown that the semiconductor photoelectrode properties fundamentally determine the PEC water splitting performance. Besides, one common strategy to improve the PEC device efficiency is to add catalytic units to the surface of the semiconductor photoelectrodes. Typically these electrocatalysts are deposited as thin film or nanoparticles.[2] The principal goal of applying electrocatalysts is to improve the kinetics at the semiconductor/electrolyte interface for desired reactions, meaning providing low energy activation pathways for the photo-generated carriers to participate in HER or OER.

3.3.3 Electrocatalysts for OER

Of the two half reactions in water splitting, OER is considerably more complex than HER. It requires a four-electron oxidation of two water molecules coupled to the removal of four protons to form oxygen-oxygen bond. As a result, oxidation of water generally needs relatively high overpotentials, and this puts additional requirement on the activities of OER catalysts compared to catalysts for HER. Moreover, a catalyst for OER must tolerate prolonged exposure to oxidizing conditions. Therefore, developing efficient and robust electrocatalysts for OER is very challenging and demanding.

Widely reported OER electrocatalysts are normally based on noble metals with high electrochemical activity such as Ru and Ir, and their metal oxides. For example, Ru and its oxide RuO_2 have been considered as the best OER catalysts.[41] Applications of

RuO_2 to improve the water oxidation reaction have been demonstrated in some milestone type of solar driven water splitting devices.[42, 43] However, these noble metal oxides (RuO_2, IrO_2) are more stable in acid, and get anodic dissolution in alkaline environment.[44, 45] Meanwhile, the limited availability of noble metals leads to high cost, which is a main obstacle for them as catalysts in large scale applications.

On the other hand, transition metals (such as Ni, Co, and Mn) and their related materials have attracted a lot interests as OER catalysts.[46, 47] Although their catalytic activities are typical lower than Ru and Ir, they are more earth abundant and more stable different conditions. For example, several research groups have observed that cobalt-oxyhydroxide-based catalysts electrodeposited from phosphate buffer (Co-Pi) reduce the

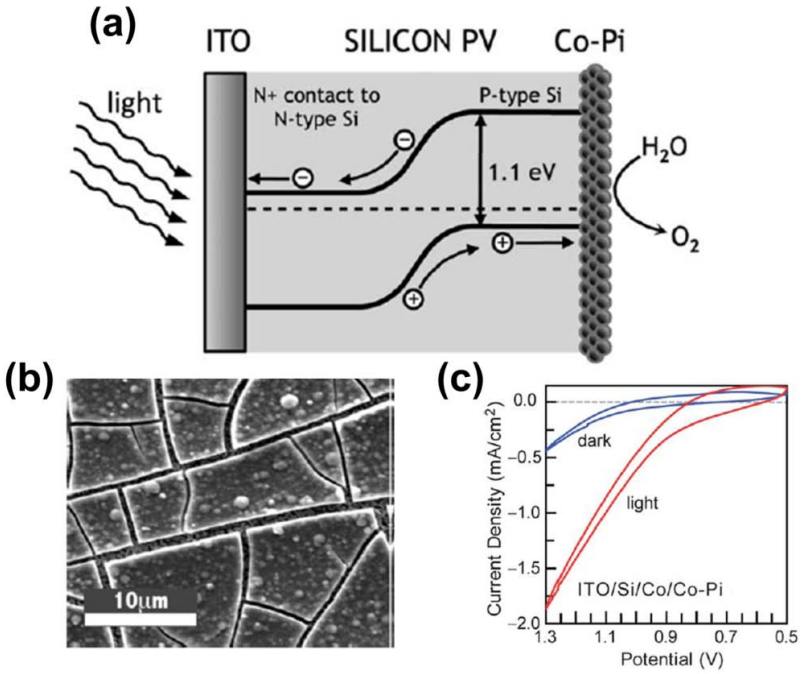

Figure 3-13: (a) Schematic of the silicon p-n junction photovoltaic device used as a photoanode coated with the thin film of the Co-Pi catalyst on the p-side and the ITO electrode on the n-side. (b) SEM image of ITO/Si/Co/Co-Pi electrode. (c) Cyclic voltammogram of the ITO/Si/Co/Co-Pi electrode.[46]

OER onset potential of photoanodes.[14, 46, 48, 49] By integrating Co-Pi catalyst onto a Si p-n junction PV cell (Figure 3-13a), the Co-Pi coated Si photoanode shows low onset potential at 0.85V and a large current density up to 2 mA•cm^{-2} under illumination at pH 7 (Figure 3-13c). In contrast, photoanode based on the same Si PV cell coated with ITO shows onset of water oxidation at 1.35 V under illumination.[50, 51]

3.3.4 NiO_x as OER catalyst

Nickel is considered the most suitable anode material for commercial water electrolyzer[52] because of its catalytic property, corrosion resistance in concentrated alkaline solutions, and its abundance (9th most abundant element in the earth). Stoichiometric nickel oxide (NiO) forms a face-centered cubic lattice with slight triangular distortions, and can be characterized as a wide bandgap insulator with reported bandgap between 3.6 and 4 eV. However, the electronic behaviour of NiO is altered dramatically by the presence of interstitial oxygen in NiO, which leads to nonstoichiometric NiO_x.In nonstoichiometric NiO_x, the average oxidation state of nickel is greater than the 2^+ in the stoichiometric material. The Ni^{3+} ions acts as acceptor centers and the NiO_x exhibits transport properties of a p-type semiconductor. Interestingly, the presence of Ni^{3+} ions, which is important to conductivity in NiO_x, is reported to play a key role in promoting the OER.[53] The mechanism of the NiO_x catalytic effect is summarized below:[54]

$$Ni(II,III) + OH^- \leftrightarrow Ni(II,III)OH + e^- \quad \textbf{3-15}$$

$$2Ni(II,III)OH \leftrightarrow Ni(II,III)O + H_2O \quad \textbf{3-16}$$

$$Ni(II,III)O + OH^- \leftrightarrow Ni(II,III)HO_2 \quad \textbf{3-17}$$

$$2Ni(II,III)HO_2 \leftrightarrow Ni(II,III)O + H_2O + Ni(II,III) + O_2 \uparrow \quad \textbf{3-18}$$

NiO_x has been applied as catalyst for silicon based photoanodes for OER.[16] The OER activity of NiO_x is only slightly inferior to that of RuO_2 or IrO_2, but NiO_x is more stable in the alkaline electrolyte and more attractive from an economic point of view. Therefore, NiO_x becomes one of the most promising catalysts for practical water oxidation.

3.3.5 NiO_x|Ni|InGaN/GaN MQW photoanode

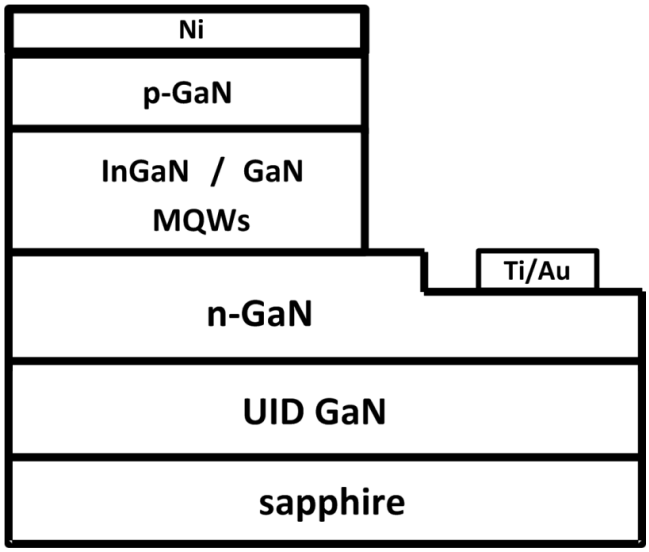

Figure 3-14: Schematic of NiO_x|Ni|InGaN/GaN MQW photoanode structure.

A photoelectrode consists of InGaN/GaN MQW structure and a Ni thin film was fabricated for efficient and stable PEC water splitting. The schematic of the photoelectrode is shown in Figure 3-14. Metal thin film deposition is done by electron beam evaporation: Ti/Au thin films are deposited on n-GaN to form ohmic contact and 150nm Ni thin film is deposited on p-GaN. The Ni thin film can serve multiple functions. In addition, the Ni coating can also serve as a reflection mirror layer for improved light absorption. Figure 3-15 shows the absorption spectra of Ni coated sample (red curve) and bare GaN sample (black curve). The entire absorption spectrum is elevated over

broadband for Ni coated sample, and significantly increased to over 60% at 450 nm, which is the effective absorption edge. Although the absorption also shows increase over longer wavelength, it is believed that those smaller energy photons are not able to generate electron-hole pairs, thus have no contribute to the photocurrent. Based on the absorption spectrum and solar spectrum, the theoretical maximum photocurrent for Ni coated sample is calculated to be 2.2 mA•cm^{-2}, almost twice the value of that can be obtained from bare GaN sample.

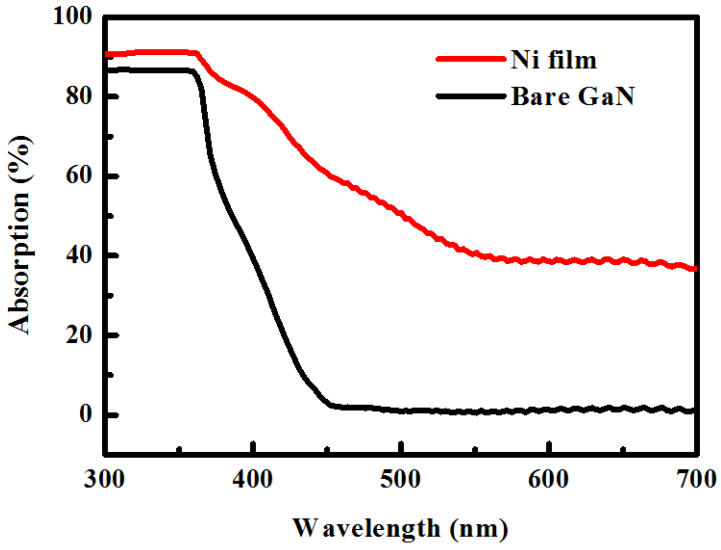

Figure 3-15: Absorption spectra of Ni coated sample (red curve), and bare GaN sample (black curve).

3.3.6 Multi-functional PEC experiment setup

The photoanode is immersed in a 1M NaOH electrolyte (pH =14), and its PEC performance is measured by a three-electrode potentiostat setup: a working electrode (WE), a Pt counter electrode (CE), and a Hg/HgO reference electrode (RE) as shown in Figure 3-16. The photoelectrode consists of three junctions — the p-i-n junction with the MQWs sandwiched between the n- and p-GaN layers, the p-GaN/Ni junction, and the Ni

(NiO_x)/electrolyte (solid/liquid) junction. By connecting to leads fabricated on both Ni/p-GaN and n-GaN and adding two more switches (S1, S2) in the measurement circuits, we

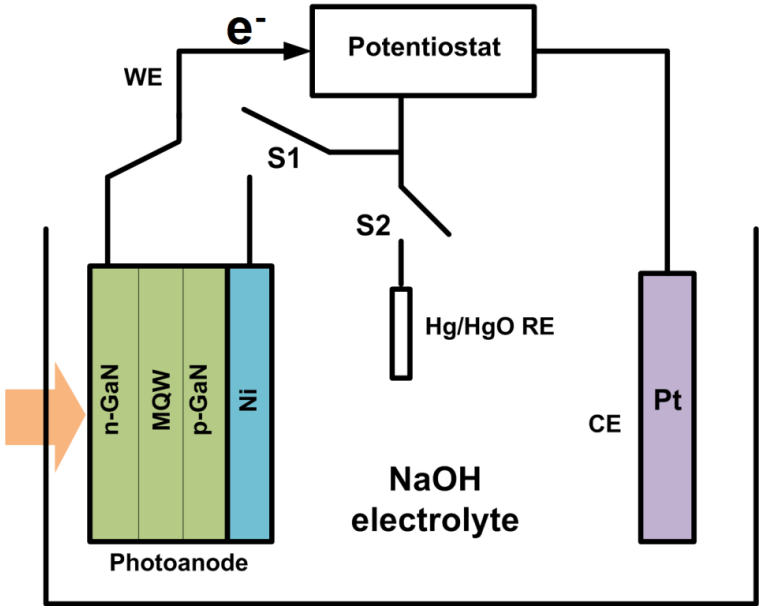

Figure 3-16: Schematic of three-electrode potentiostat setup.

can independently carry out the solid-state PV measurement, Ni film activation (NiO_x formation), and photoelectrode PEC characterization, conveniently in one system without modifying the setup, which allows more consistent and time efficient data collection. On the other hand, this strategy allows us to separate, and more importantly, to individually design and optimize the optoelectronic, carrier transport, and electrochemical processes into different sections of the PEC cell. Table 3-2 describes different measurement configurations.

Table 3-2: Setup configurations for different measurements/functions.

Measurement/Function	WE	S1	S2	CE	RE
Three-electrode PEC	n-GaN	off	on	Pt	Hg/HgO
Two-electrode	n-GaN	off	off	Pt	-
Ni/NiO_x activation	Ni	off	on	Pt	Hg/HgO
Photovoltaic	n-GaN	on	off	-	-

3.3.7 PEC Measurements

Before PEC measurement, the PV behaviors of samples are first characterized. Connecting the WE to n-GaN and switch S1 to Ni contact, the PV performance can be measured. The top Ni film in this case serves as an ohmic contact material for p-GaN[55] to decrease the contact resistance, particularly with thermal annealing. The thermal annealing is done in a rapid thermal annealing (RTA) system, with annealing temperature of 450 ºC under N_2/O_2 mixed atmosphere for 3 minutes. As shown in Figure 3-17, the RTA treated Ni sample has a larger short circuit current (J_{sc}) (0.62 mA•cm^{-2}) than the un-annealed Ni sample (0.4 mA•cm^{-2}) upon illumination, suggesting improved carrier transport at p-GaN/Ni contact after RTA. The open circuit voltage (V_{oc}) for both devices are the same (2.3 V), and this large V_{oc} obtained is crucial, which strongly indicates the sustainable spontaneous solar water splitting. Based on the PV measurement, the Ni RTA sample show an energy conversion efficiency of 0.97%, which is 50% more compared to that of un-annealed one (0.64%).

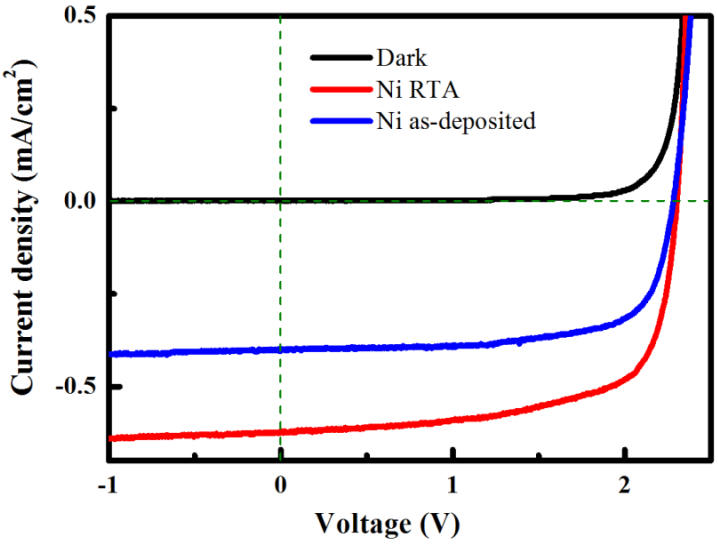

Figure 3-17: *J-V* plot of the InGaN/GaN MQW photovoltaic cell under dark, with RTA Ni contact and as-deposited Ni under 100 mW•cm^{-2} illumination.

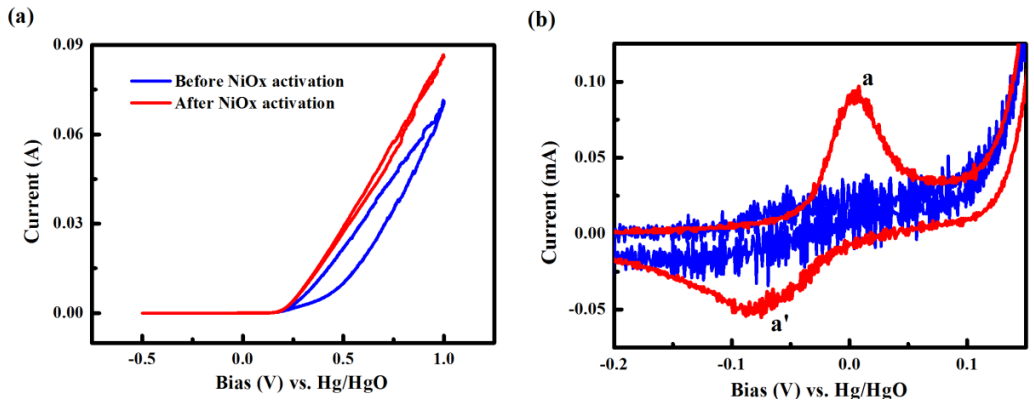

Figure 3-18: (a) CV plot of Ni thin film in 1M NaOH, before and after NiO_x activation. Scan rate: 10 $mV \cdot s^{-1}$. (b) Magnification of CV from -0.2 V to 0.1 V.

Although Ni can be oxidized during the PEC reaction, to have consistent performance of different batch of devices, the Ni layer is intentionally activated in the alkaline electrolyte to form NiO_x prior to the PEC measurement. During Ni activation, the WE is connected to top Ni thin film. We first applys a cyclic voltammetry scan with a potential window from -0.5V to 1V, at a rate of 10 $mV \cdot s^{-1}$ (Figure 3-18a blue curve). Then we oxidize the Ni film by applying multiple CV scans with the same potential range, but at a faster rate 100 $mV \cdot s^{-1}$, until the anodic current saturates. After the activation process, we again scan the Ni film at 10 $mV \cdot s^{-1}$ (Figure 3-18b red curve) to observe any difference from the CV curve. At the low potential range from -0.2V to 0.1V, one oxidation peak a and one reduction peak a′ appears after multiple activation scans. This low potential region has been called the Ni(II) region, and peak a has been assigned to the formation of $Ni(OH)_2$, as indicated by Equation 3-15. Similar voltammograms have been reported for nickel based anode in various alkaline solutions.[56, 57] At more positive potential range from 0.25V to 1V, a large anodic current is observed after the activation scan. This potential region is known as the Ni(III) region, and the relatively larger anodic

current is related to further oxide growth and the change in Ni oxidation state from 2^+ to 3^+, as indicated by Equation 3-17.

Figure 3-19 shows the CV measurement of InGaN/GaN MQW samples with different surface coatings and treatments. The photoanode with RTA Ni followed by NiO_x activation (NiO_x|Ni|InGaN/GaN MQW) shows the lowest onset potential ($V_{ph\text{-}onset}$, defined as 0.1mA•cm^{-2} under 100mW cm^{-2} illumination) (-2.105 V vs. Hg/HgO, -1.139 V vs RHE) in the CV studies. The $V_{ph\text{-}onset}$ of NiO_x|Ni|InGaN/GaN MQW electrode is well below the thermodynamic oxidation level of water ($E_{H2O/O2}$, green dashed line, 0.264 V vs Hg/HgO, 1.23 V vs RHE). This is because of the embedded PV cell, which could provide 2.3V photovoltage that moves the $V_{ph\text{-}onset}$ to more negative values. NiO_x|Ni|InGaN/GaN MQW photoanode also demonstrates the largest anodic current density (0.556 mA•cm^{-2}) at $E_{H2O/O2}$. In the CV curve, there are two small peaks in the negative potential range (-2.5 V to -2.0 V), corresponding to Ni oxidation and reduction, which are the signs of successful NiO_x formation. The photoanode with RTA Ni, but no NiO_x activation (RTA Ni|InGaN/GaN MQW, green curve) shows a close $V_{ph\text{-}onset}$ (-1.136 V vs RHE) compared to NiO_x|InGaN/GaN MQW, but a smaller anodic current (0.39 mA•cm^{-2}) at $E_{H2O/O2}$. It is believed that the difference of the anodic current between them is due to the NiO_x catalytic effect for OER, which improves the kinetics of charge transfer. The photoanode with as-deposited Ni (Ni|InGaN/GaN MQW, blue curve) shows a more positive $V_{ph\text{-}onset}$ (-1.647 V vs Hg/HgO), and an anodic current density of 0.362 mA•cm^{-2} at $E_{H2O/O2}$. For aforementioned three samples, there is very minor difference between forward and backward CV scans, which suggests great stability of the Ni protected MQW photoanode. The bare GaN photoanode with no surface coating (bare

GaN, pink curve) shows an even more positive $V_{ph\text{-}onset}$ (-1.496 V vs Hg/HgO) and a current density of 0.285 mA•cm^{-2}. However, the forward and backward CV scan could not overlap with each other, indicating irreversible electrochemical reactions. According to the comparison, the superior performance of NiO_x|Ni|InGaN/GaN MQW photoanode over others is closely related to the NiO_x formation and its OER catalytic effect.

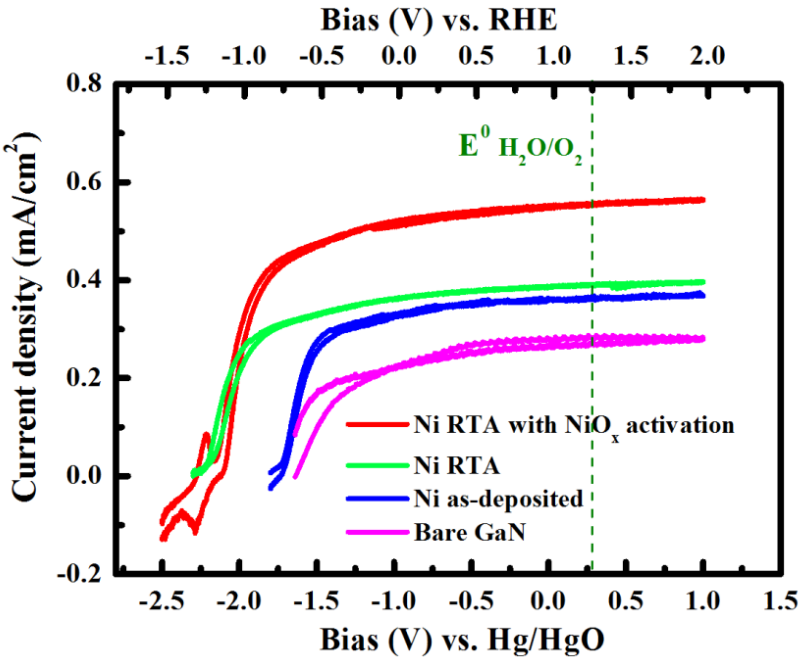

Figure 3-19: Comparison of CV characteristics of MQW photoanodes with different coatings.

The applied bias conversion efficiency (ABCE) of the NiO_x|Ni|InGaN/GaN MQW photoanode for water splitting is measured using a two-electrode configuration, and is calculated from *J-V* data using Equation 3-9. The NiO_x|Ni|InGaN/GaN MQW photoanode achieves an overall STH conversion efficiency of 0.64% at zero bias with the current density of 0.52 mA•cm^{-2} (Figure 3-20a). These values are much higher than most of other reported III-nitrides PECs. At the real working condition, a lot of oxygen bubbles are generated at the photoanode surface as shown in Figure 3-21. The two-electrode

measurements of Ni|InGaN/GaN MQW and bare InGaN/GaN photoanodes are also conducted (shown in Figure 3-20b and c) and the performances of InGaN/GaN MQW photoanodes with different surface treatments are summarized in Table 3-3. The efficiency at zero bias for NiO_x|Ni|InGaN/GaN MQW photoanode shows 56.1% and 82.9% increase compared to that of Ni|InGaN/GaN and bare InGaN/GaN photoanodes, respectively.

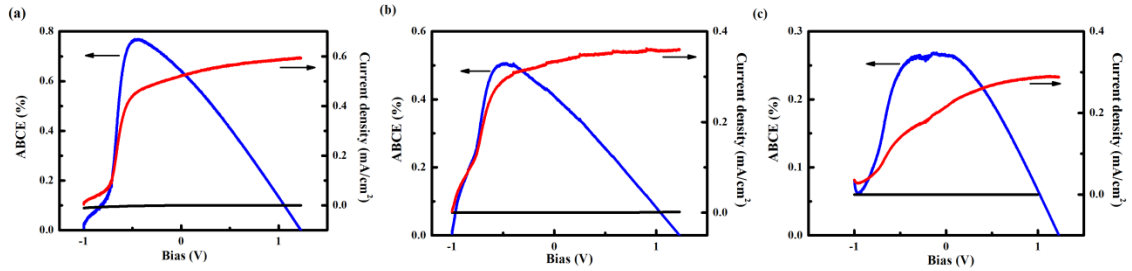

Figure 3-20: Two-electrode measurement of photoanodes with different surface coatings and treatment.

Figure 3-21: Bubbles generated at the surface of the NiO_x|Ni|InGaN/GaN MQW photoanode.

Table 3-3: Summary of photoanodes performance (NiO_x|Ni|InGaN/GaN MQW).

Electrode	**$V_{ph\text{-}onset} - EH_2O/O_2$ (V)**	**Current density (mA•cm^{-2}) at EH_2O/O_2**	**ABCE (% at 0V)**
NiO_x|Ni	-2.37	0.556	0.64
Ni as-deposited	-1.91	0.362	0.41
Bare GaN	-1.76	0.285	0.26

The conversion efficiency may also be expressed as a product of the solar conversion efficiency of the InGaN/GaN MQW PV cell η_{PV}, and fuel generation efficiency of water electrolysis η_{FG}, which includes losses that arise from the overpotentials at the solid/liquid junction and ohmic resistances:

$$\eta_{abce} = \eta_{PV} \times \eta_{FG} \qquad \textbf{3-19}$$

Since the PV cell provides a conversion efficiency of 0.96%, η_{FG} is calculated to be ~ 70%. With the NiO_x as the OER catalyst, this value is comparable with η_{FG} in some other PEC systems, where higher-efficiency PV cells are used, such as 3jn-a-Si PVs and GaAs PV.[14, 15] We note that based on η_{FG}, higher overall efficiency PEC cell may be readily achieved through the use of more efficient III-nitride PVs.[20, 58, 59]

Lastly, Ni coated photoelectrodes have shown most active and stable solar water oxidation, which can act as a protective layer for the p-GaN. The stability of the NiOx|Ni|InGaN/GaN MQW photoanode in the strong alkaline environment is studied. The measurements are conducted at zero bias. The current density keeps stable over extended period (Figure 3-22, red curve), with reduction of 0.023 $mA \cdot cm^{-2}$ (less than 4.5%) in 12 hours, indicating excellent stability of NiO_x|Ni protected InGaN/GaN MQW photoanode. On the other hand and for comparison, we also conduct a stability test on bare InGaN/GaN MQW photoanode. A rapid decrease current density, drops over 20% in 7 hours, along with large fluctuation, is observed (Figure 3-22, blue curve), presumably due to the photoelectrochemical oxidation and decomposition of top p-GaN in the strong alkaline solution.

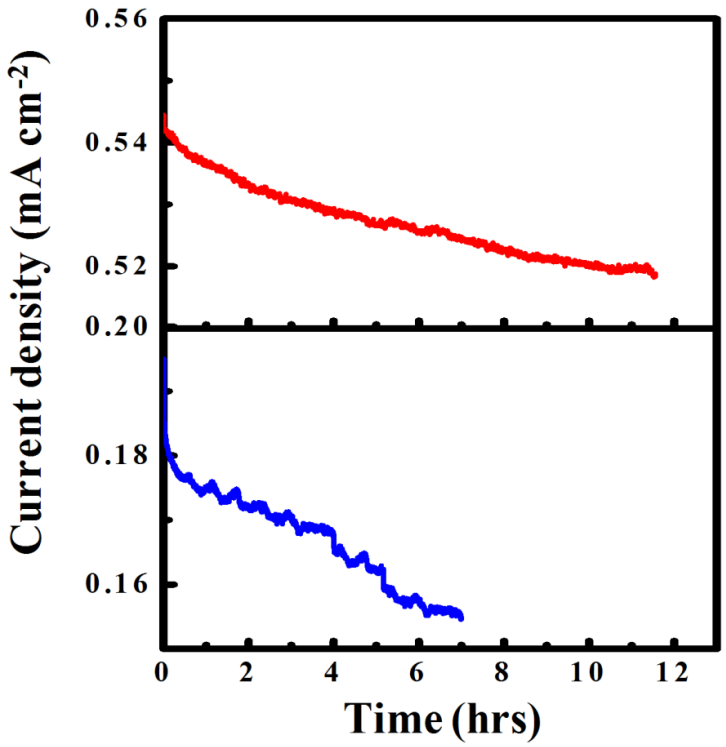

Figure 3-22: Comparison of stability tests between NiO_x|Ni|GaN/InGaN MQW (red curve) and bare GaN (blue curve) photoanodes.

3.3.8 Summary

A NiO_x|Ni|InGaN/GaN MQW photoanode has been developed for efficient and stable spontaneous water splitting. The InGaN/GaN MQW solar cell structure allows decoupling, and thus independent tuning and optimization, of the photovoltaic action and electrochemical fuel production reaction. The InGaN/GaN MQW solar cell structure allows efficient light absorption in the InGaN layers, and simultaneously the large photovoltage from the GaN p-n junction to sustain spontaneous solar water splitting. Moreover, a Ni thin film is coated on the MQW devices, which serves multiple functions and further boosts the overall performance of the photoanode. Ni, after thermal annealing, helps photocarrier transport and the NiO_x, formed on the photoanode through activation in the alkaline solution, works as an electrocatalyst for more efficient OER. The well

overlapped forward and backward CV scans, as well as the long-term lifetime test indicate excellent stability of the Ni protected photoanode. The NiO_x|Ni|InGaN/GaN MQW photoanode shows an overall efficiency of 0.64% at zero bias, with a less than 5% reduction of current density in 12 hours. The sufficient photovoltage provided by InGaN/GaN MQW solid-state junction, the good carrier transport ability of Ni contact on p-GaN, and the catalytic effect of NiO_x at the solid/liquid junction lead our approach to be very promising for practical spontaneous solar water splitting and hydrogen production.

3.4 InGaN/GaN MQW photoanode with plasmonic metal nanostructures

3.4.1 Introduction

In section 3.3, I demonstrate that efficient and stable PEC water splitting can be achieved by using InGaN/GaN MQW with NiO_x catalysts. The NiO_x catalysts improve the kinetics and lower the overpotential for OER at the photoanode, leading to increased STH conversion efficiency. In order to further boost the PEC cell performance, larger photocurrent is desired, meaning more solar energy has to be harvested. In this section, I use laser interference ablation to modify the InGaN/GaN MQW surface, creating plasmonic metal nanostructures for enhanced solar photon collection.

Typically, plasmonic metal nanostructures can improve the solar energy conversion efficiency of semiconductors via two pathways:[60] photonic enhancement and plasmonic energy-transfer enhancement. For patterned plasmonic metal nanostructures with relatively large size, the incident light can be effectively scattered multiple times, therefore increasing the optical path length and the absorption in the semiconductor layers.[61-66] This is referred to as photonic enhancement or light trapping. In this case, the

enhancement happens at the energies above the bandgap of a semiconductor. Alternatively, if the semiconductor is very close to the metal, the enhancement can occur by transferring the energy in the oscillating electrons or local plasmonic field from the metal to the semiconductor via direct electron transfer or plasmon-induced resonant energy transfer.[67-72] This is called as plasmonic energy-transfer enhancement and is strong in small metal nanoparticles with small scattering cross-sections. In this section, I utilize the photonic enhancement effect from the plasmonic metal nanostructures to enhance the solar light harvesting and the PEC performance.

As shown in Figure 3-23, long-range ordered plasmonic metal nano-dent arrays are created on InGaN/GaN MQW surface. First, laser interference ablation is used to directly pattern nano-dent arrays on top p-GaN layer. After the patterning, triple metal layers Ni/Ag/Ni with thickness of 5 nm/50 nm/100 nm are deposited. The 5 nm Ni is used to make a good electrical contact on p-GaN for hole transport. Then 50 nm Ag film is deposited, because Ag is reported to be able to excite the surface plasmon resonance at wavelength around 450 nm, which could match the InGaN QW bandgap. Lastly, another 100 nm Ni film is deposited. This Ni layer is then intentionally activated in the alkaline electrolyte to form NiO_x as described in section 3.3, serving as OER catalysts. The as-fabricated plasmonic metal nano-dent are expected to initiate electromagnetic wave scattering at the upper surface of the photoanode, which leads to enhanced light absorption in the p-GaN, MQWs and n-GaN over large portion of the solar spectrum (400 nm to 700 nm). The light absorption ability of the photoelectrode is improved due to plasmonic wave scattering effect from the plasmonic metal nanostructures. The absorption enhancement increases the photocurrent obtained from the plasmonic metal

nano-dent photoelectrode, and eventually leads to higher STH conversion efficiency of the PEC cell.

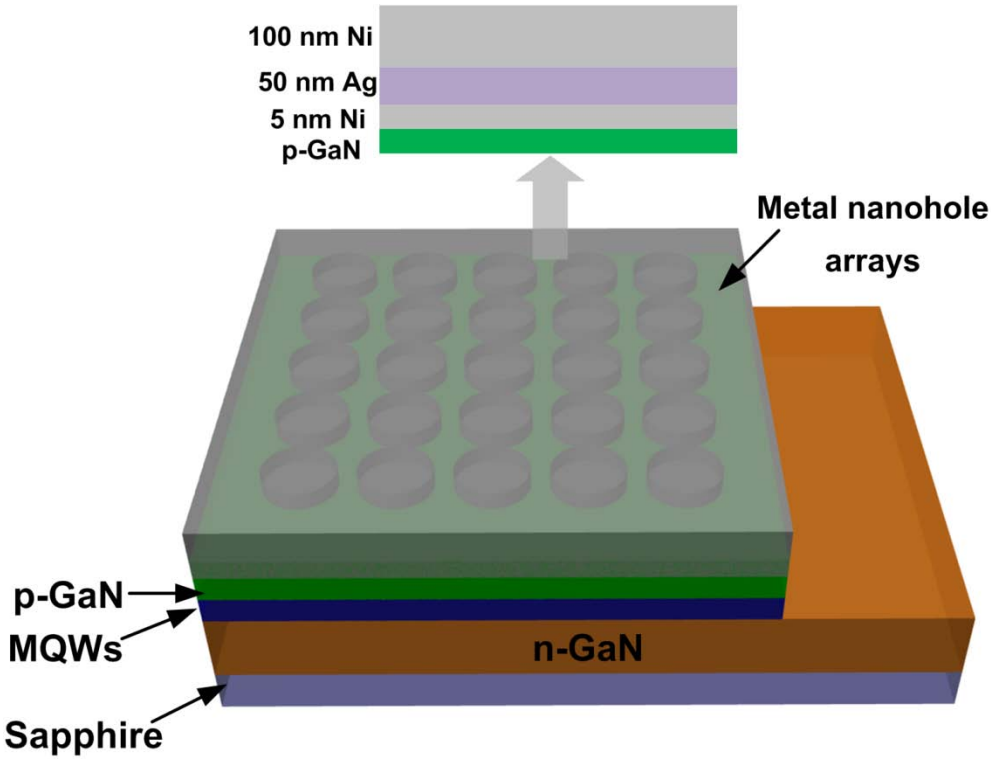

Figure 3-23: Schematic of plasmonic metal nano-dent arrays on InGaN/GaN MQW.

3.4.2 Laser interference ablation

Larger-scale periodic nanostructures are crucial to initial plasmonic effect. In recent years, a number of approaches have demonstrated large scale fabrication of nanostructure arrays, such as electron beam lithography (EBL),[73] nanosphere lithography (NSL),[74] and nanoimprint lithography (NIL).[75] However, they all have their own shortcomings. For example, the throughput is a problem for EBL, which is too slow, complex and costly for scale-up production. Although NSL and NIL are two popular methods to obtain ordered nanostructures, NSL suffers from poor repeatability, while NIL needs a master mold, which also increases the cost.

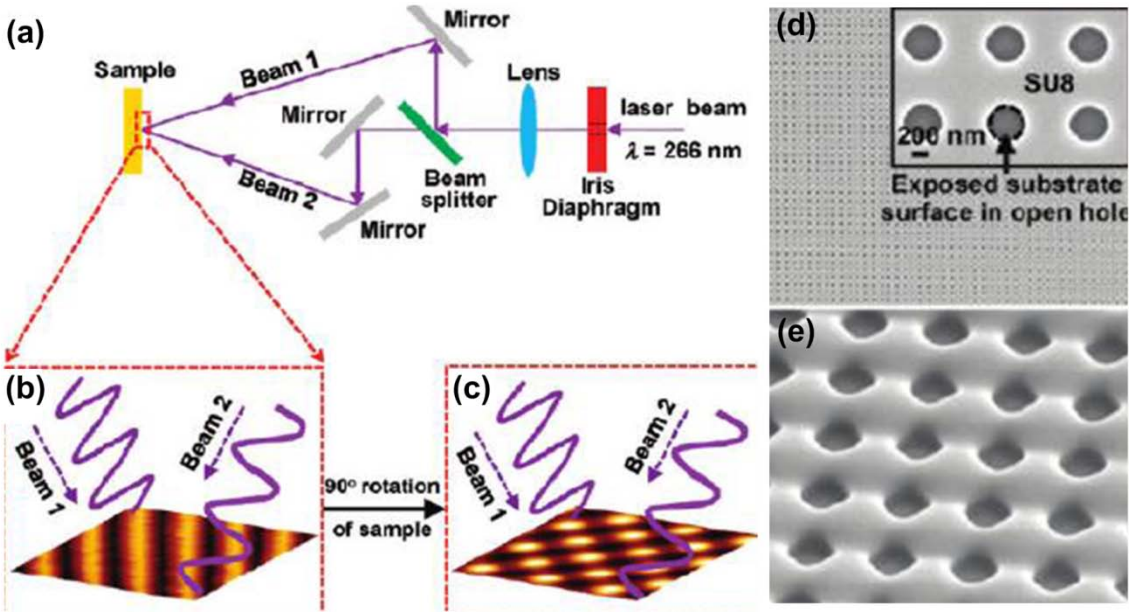

Figure 3-24: (a) Schematic of experimental setup for the laser interference patterning. (b) The interference between beam 1 and 2 forms a grating pattern on photoresist. (c) Sample is rotated by 90º with a second exposure. (d) The top view SEM image of patterned SU-8 film. (e) 45º-tilted-view SEM image of patterned SU-8 film.[76]

Laser interference lithography (LIL) is known as a fast, large-scale, and maskless technique, and has demonstrated itself as a promising method for nanopatterning on various materials. For example, LIL has been used to pattern SU-8 photoresist without a photomask, which is an epoxy-based negative photoresist commonly used in the microelectronics industry. As shown in Figure 3-24a, a 10ns pulsed Nd:YAG laser with wavelength of 266nm is used as the laser source. The primary laser beam is split into two coherent light beams (beam 1 and 2). The interference between beam 1 and 2 forms a grating pattern on photoresist under one single laser pulse (10 ns). The sample is then rotated by 90º for a second exposure. After development, the exposed areas of SU-8 remains and serves as the mask for the following processes.[76] Figure 3-24d and e show the SEM images of top and 45º tilted views of patterned SU-8 film, respectively.

To further reduce the cost of patterning nanostructures on semiconductors, laser interference ablation (LIA) is introduced. It has the advantage of LIL in creation periodic patterns, but more importantly, it can directly produce nanoscale patterns on various substrates,[77] thus eliminating several process steps compared to the LIL based approach.

Here, a three beam LIA is used to create nano-dent structure on InGaN/GaN MQW sample surface. Figure 3-25a shows the optical pathway of the three beam LIA. The primary beam from the laser source is split into three beams to interfere with each other on the sample surface. A 10 ns pulsed Nd:YAG laser, with 355 nm harmonic wavelength and intensity of 100 $mJ \cdot cm^{-2}$ per pulse is applied here. The laser beam diameter is 150 mm. The laser irradiation causes thermal decomposition of GaN into gaseous nitrogen and Ga droplets, following the equation:

$$GaN \rightarrow Ga + \frac{1}{2} N_2 \qquad \textbf{3-20}$$

The GaN sample after laser irradiation tends to show some material residues, such as Ga and Ga_2O_3. These residues can be cleaned up by dipping sample in a dilute 10% HCl.[78] The resulted surface has periodic array of nano-dent patterns with six-fold rotational symmetry as shown in Figure 3-25b.

The intensity distribution, $I(x,y)$ of the three beam interference, and the period P of the 2-dimensional (2-D) hexagonal lattice array are described by Equations 3-21 and 3-22, respectively:[79]

$$I(x,y) = I_{laser} + \tfrac{2}{3} I_{laser} \times \left[\cos\left(k \sin\theta\left(-\tfrac{3}{2}x + \tfrac{\sqrt{3}}{2}y\right)\right) + \cos\left(k \sin\theta\left(-\sqrt{3}y\right)\right) + \cos\left(k \sin\theta\left(\tfrac{3}{2}x + \tfrac{\sqrt{3}}{2}y\right)\right)\right] \quad \textbf{3-21}$$

$$P = \frac{\lambda}{\sqrt{3}\sin\theta} \quad \textbf{3-22}$$

where I_{laser} is the laser intensity, k is the wave vector, θ is the angle of the beams with respect to the vertical axis and λ is the wavelength of laser light. The simulated intensity distribution of three beam interference patterning is shown in Figure 3-26, with a Gaussian profile—the highest intensity at the center of each nano-dent, and decreasing along the radius. Such a laser intensity distribution should leave nano-dent with sloped sidewalls.

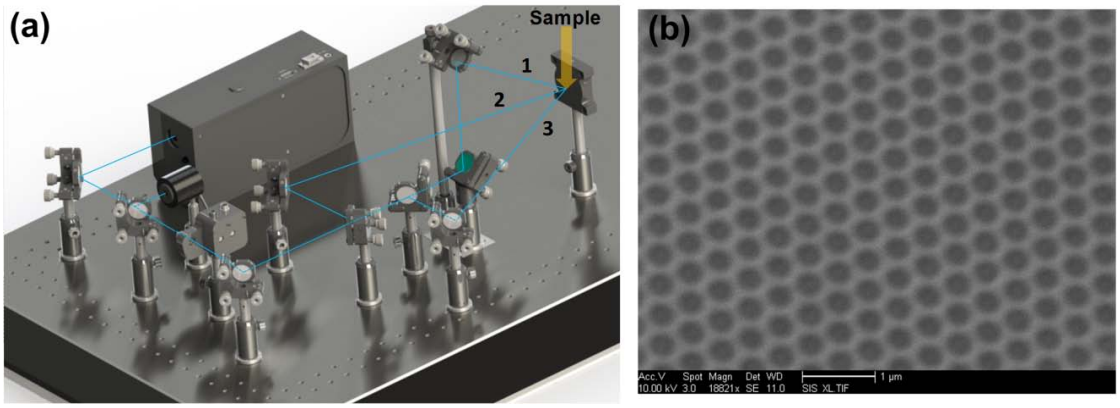

Figure 3-25: (a) Schematic of LIA with three coherent light beams. (b) The top view SEM image of patterned nano-dent structure on InGaN/GaN MQW sample.

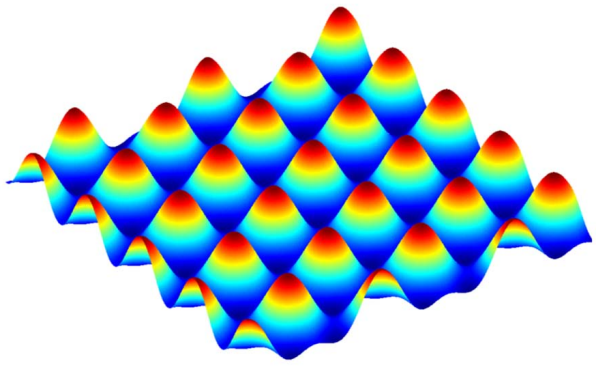

Figure 3-26: Simulation of three beam laser interference intensity distribution.

Figure 3-27a shows the atomic force microscopy (AFM) image of nano-dent arrays and Figure 3-27b shows the nano-dent profile based on AFM scan. The profile corresponds well with the simulated Gaussian distribution of the laser intensity, resulting in sloped sidewalls of each nano-dent. The AFM scan profile also indicates that the nanoh-dent depth is about 40 nm, and the periodicity of the nano-dent arrays is around 450 nm.

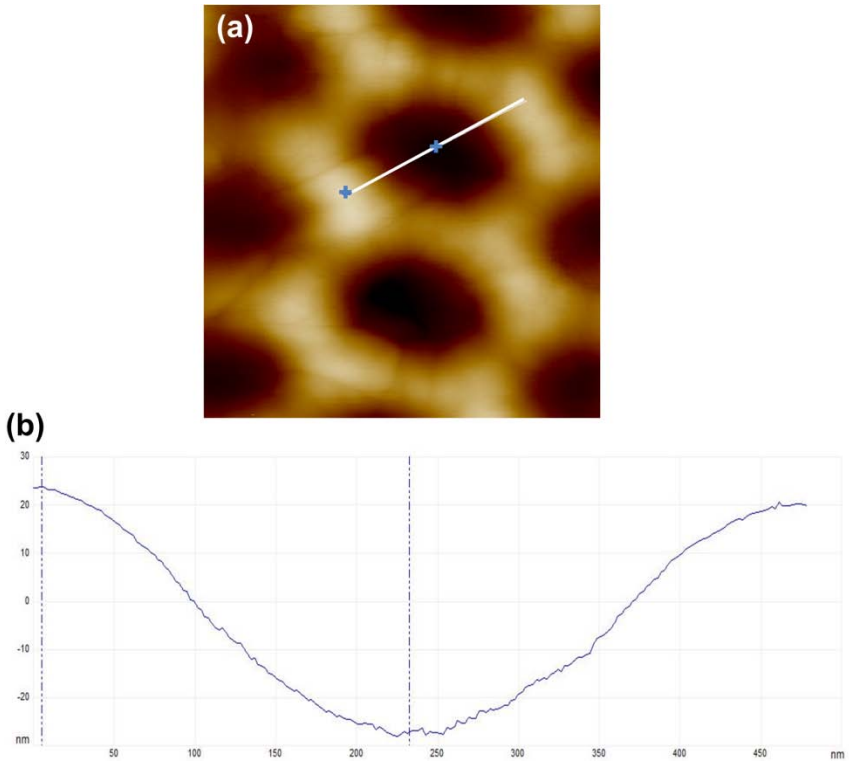

Figure 3-27: (a) AFM image of nano-dent arrays. (b) Profile of the AFM scan of nano-dent indicated by white line in (a).

In LIA, the laser beam angle and intensity are extremely important, controlling the dent diameter and periodicity as well as the hole depth. Especially the hole depth has to be optimized, because over-etch of the top p-GaN layer can cause degradation of the photovoltage, which will be harmful to spontaneous water splitting. This will be discussed in the PEC measurement section 3.4.4.

3.4.3 Absorption measurement and simulation

After the LIA and nano-dent formation, the Ni/Ag/Ni triple metal layers with thickness of 5 nm/50 nm/100 nm respectively are deposited on the samples by electron beam evaporation. Figure 3-28a shows the SEM image of the as-fabricated plasmonic metal nano-dents. Identical metal layers are also deposited on a sample with flat surface to make a comparison. Samples with different surface structures/deposition: flat/bare surface (Flat/Bare), flat with metals (Flat/Metal), and nano-dents with metals (ND/Metal), are characterized for light absorption inside an optical integration sphere. Broadband light from a halogen lamp comes into the integration sphere at a small angle (<5°) shining from the backside of the samples. Reflected light including specular and diffuse reflection is collected by the integration sphere. Figure 3-28b shows the measured absorption spectra of samples.

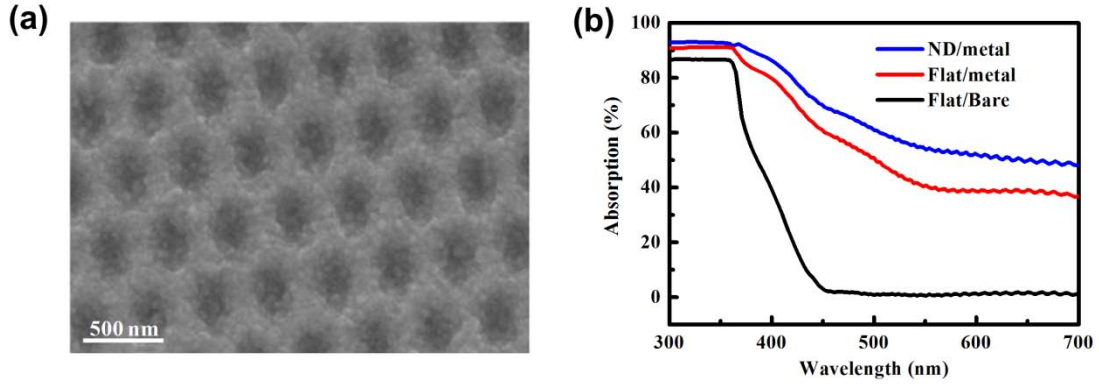

Figure 3-28: (a) SEM image of plasmonic metal nano-dents. (b) Absorption spectra of samples: Flat/Bare, Flat/Metal, and ND/Metal, respectively.

The ND/Metal sample (blue curve) shows a similar absorption spectrum as that of the Metal/Flat sample. The absorption stays high (> 90%) until 360 nm (3.4 eV), which can be attributed to the fully absorption from InGaN QWs as well as GaN layers. The absorption slowly decays over the longer wavelength. Compared to that of Flat/Metal

sample, the entire absorption spectrum is further evelated in ND/Metal case over broadband. This broadband absorption enhancement from Flat/Metal and ND/Metal can be explained as follow. At short wavelength (< 450 nm), the energies of incident photons are still larger than the bandgap of the InGaN QW. In this situation, photons can be efficiently absorbed by InGaN when they pass through the MQWs as well as the thick GaN layers. Even without surface structures or metal layers, the absorption could still be significant. The optical power absorbed per unit volume can be represented by Equation 3-23:

$$P_{abs}(\lambda) = \frac{1}{2}\omega\varepsilon' |E(\lambda)|^2 \qquad \textbf{3-23}$$

where $|E(\lambda)|^2$ is the magnitude of the electric field, $\omega = 2\pi c / \lambda$ is the angular frequency of the light, and ε' is the imaginary part of the GaN permittivity. Figure 3-29 shows the full-wave numerical simulation of electric field intensity distribution in the samples for incident wavelength of 450 nm. As can be seen in the Flat/Metal sample, the electric field intensity is increased over the MQWs region compared to that in the Flat/Bare sample. This intensity increase is due to the reflection from the top metal layers, and leads to the enhanced absorption. The additional enhancement in the ND/Metal case can be attributed to the plasmonic metal nanod-ent, which cause effective scattering of the incident light, in other words, the re-distribution of the intensity of the electric field in the sample. This conclusion is also supported by the full-wave numerical simulation. Clearly, in ND/Metal, the electric field intensity is re-distributed, with a significant electric field intensity increase in the QW region. The field re-distribution caused by the plasmonic metal nano-dent leads to the improved light absorption.

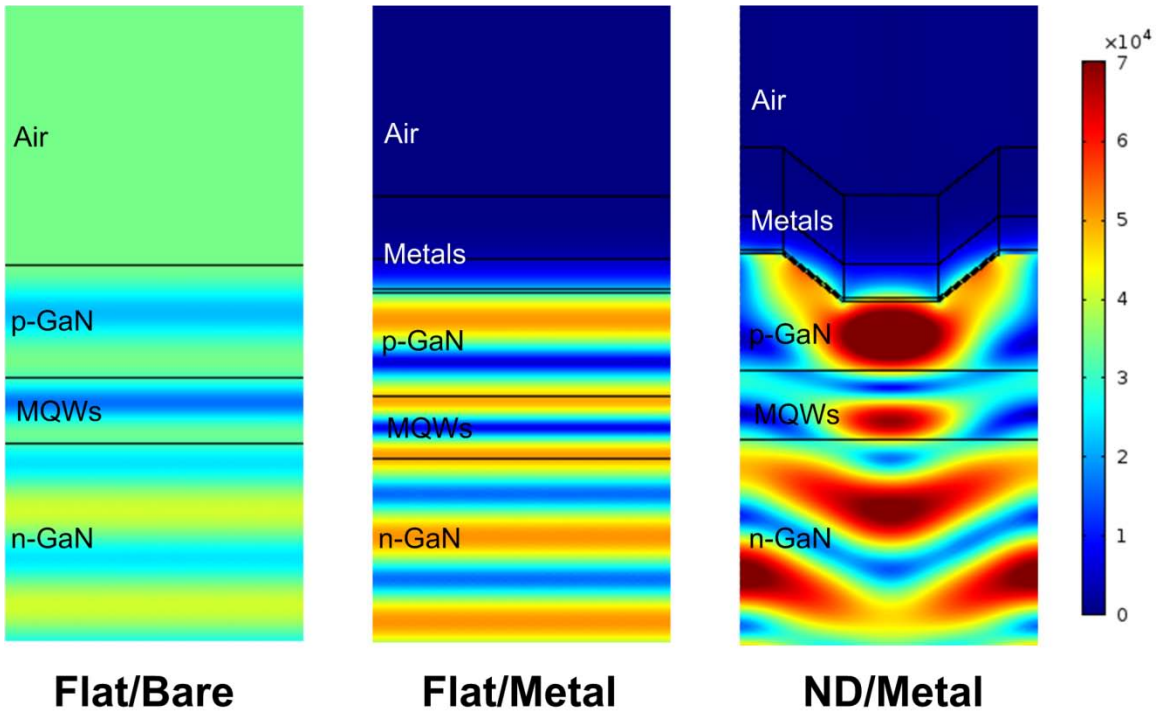

Figure 3-29: Full-wave numerical simulation for the electromagnetic wave (wavelength of 450 nm) distribution of the magnitude of electric field in Flat/Bare, Flat/Metal, and ND/Metal samples.

At wavelength longer than 450 nm, with photon energies smaller than the bandgap of InGaN QW, the Flat/Bare sample has very limited response to those photons and the absorption stays at very low level. The absorption also decays for Flat/Metal and ND/Metal samples over the long wavelength spectra, but compared to Flat/Bare sample, the absorption enhancement is actually increased in the Flat/Metal and ND/Metal samples at longer wavelength compared to that at short wavelength. Full-wave numerical simulation of electric field intensity distribution of incident wavelength of 500 nm (Figure 3-30) shows the electric field intensities are increased over the p-GaN, MQWs and n-GaN in both Flat/Metal and ND/Metal samples. Even the incident photon energies are smaller than the bandgaps of p-GaN, MQWs and n-GaN, the significantly increased electric field intensities still make the enhanced absorption. However, even though the

absorption at long wavelength is increased, since the InGaN bandgap is determined to be of 2.74 eV (450 nm), the long wavelength light absorption is not expected to contribute a lot to the carrier generation and thus total photocurrent.

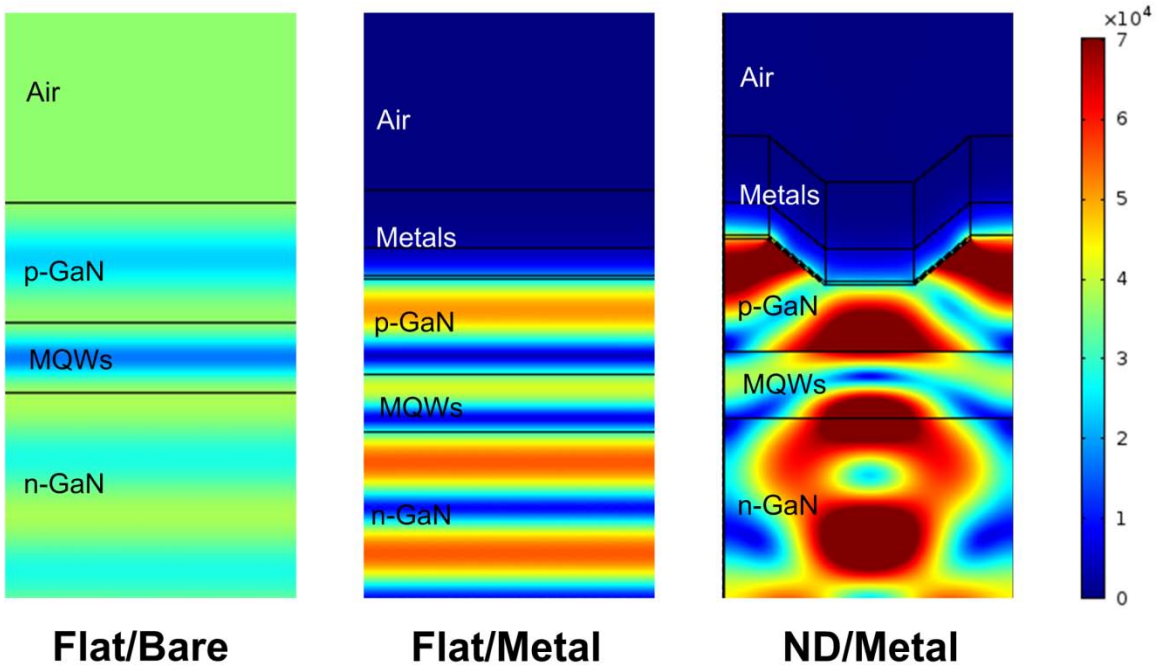

Figure 3-30: Full-wave numerical simulation for the electromagnetic wave (wavelength of 500 nm) distribution of the magnitude of electric field in Flat/Bare, Flat/Metal, and ND/Metal samples.

3.4.4 PEC measurement

PEC measurements of InGaN/GaN MQW photoanodes with different surface structures are conducted with the same setup and under the same conditions as described in section 3.3. First, PV measurement is conducted to determine if the V_{oc} from samples are sufficient to sustain water splitting. As shown in Figure 3-31, Flat/Metal and ND/Metal samples both demonstrate V_{oc} of 2.27 V, which should be enough for practical water splitting. ND/metal sample shows J_{sc} of 0.98 mA•cm^{-2}, which is smaller than the

theoretical value (2.4 mA•cm^{-2}) obtained from the absorption spectrum. This can be due to the carrier recombination in the MQWs as well as during transport. The Flat/Metal

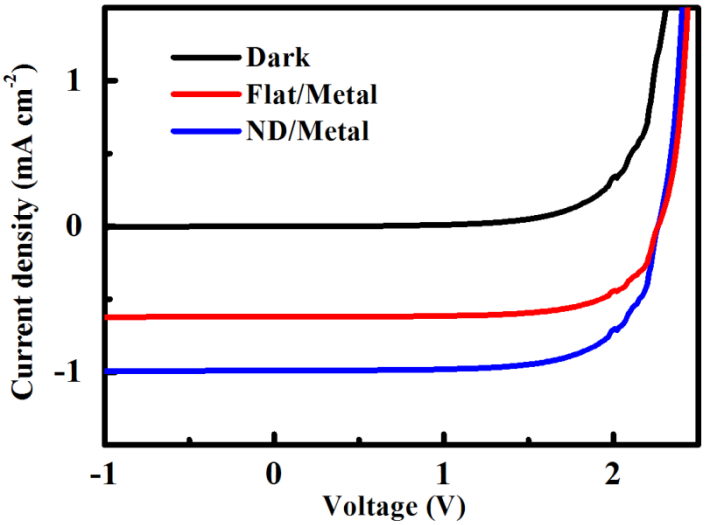

Figure 3-31: *J-V* plot of InGaN/GaN MQW PV cells with different surface structures.

sample shows a J_{sc} of 0.62 mA•cm^{-2}. The over 50% increase of J_{sc} from ND/metal sample corresponds well to the absorption measurement, in which plasmonic metal ND structure enhances the light absorption. In additional, the nanostructured interface between p-GaN/metal NDs increases the contact area and decrease the carrier transport distance, which could lead to increased carrier collection and thus photocurrent.

Note that the depth of nano-dent is a crucial parameter that affects the PV performance of the ND/Metal sample. Figure 3-32a shows an AFM image of a ND/Metal sample with the nano-dent depth of 130 nm. The PV measurement demonstrates that the V_{oc} of this sample drops dramatically to less than 1 V (Figure 3-32b), which would not be able to support PEC water splitting. The dark current of the device shows a low turn-on voltage compared to other InGaN/GaN MQW devices with shallow nano-dent, indicating there could be certain kind of leakage in the device structure. Moreover, since the light

absorption ability should vary little from sample to sample, the degraded V_{oc} cannot be due to the less carrier generation. This V_{oc} degradation could be due to the over-etch of the top p-GaN during LIA, and the Ni diffusion into the p-GaN or even MQW region during RTA, which creates an additional channel for carrier transport, and can pin down the quasi-Fermi level.

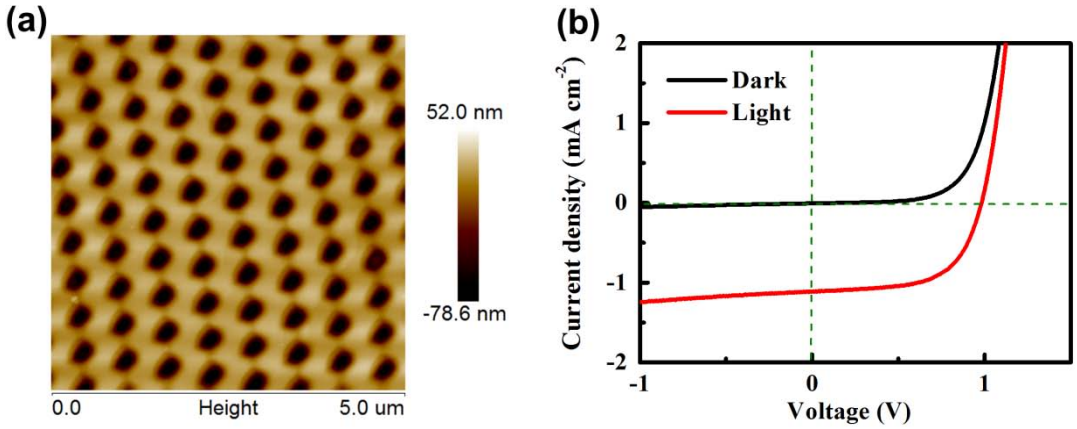

Figure 3-32: (a) AFM image of a ND/Metal sample with nano-dent depth of 130 nm. (b) PV measurement of sample with deep holes, showing decreased V_{oc}.

The top 100 nm Ni film is then activated to form NiO_x as catalysts for OER. Figure 3-33 shows the CV measurement of photoanodes with different surface structures. The NH/Metal photoanode demonstrates an onset potential ($V_{ph\text{-}onset}$, defined as 0.1 mA•cm^{-2} under 100 mW•cm^{-2} illumination) of -1.356 V vs. Hg/HgO, and the largest anodic current density (0.903 mA•cm^{-2}) at $E_{H2O/O2}$ (green dashed line, 0.264 V vs Hg/HgO, 1.23 V vs RHE). In the CV curve, there are several small peaks at the negative potentials, which can be attributed to Ni oxidation and reduction peaks. However, there is a relatively large peak at potential of -1.8 V vs Hg/HgO, which believed is due to the Ag oxidation.[80] Although, there should be 100 nm Ni film covered above, Ag may still expose to the electrolyte at the sidewalls of nano-dent, and get oxidized. The Flat/Metal

photoanode shows an onset potential of -1.267 V vs. Hg/HgO, and an anodic current density of 0.586 mA•cm^{-2} at $E_{H2O/O2}$. It is believed that two effects can contribute to the anodic current difference between ND/Metal and Flat/Metal photoanodes. First, the plasmonic metal nano-dent structures improve the light absorption in the ND/Metal photoanode, leading to higher photocurrent, which is supported by the PV measurement. Second, the nano-dent structures also increase the electrochemical reaction area compared to flat surface, favoring the carrier transfer at the interface. The Flat/Bare photoanode shows the lowest anodic current density of only 0.37 mA•cm^{-2} at $E_{H2O/O2}$.

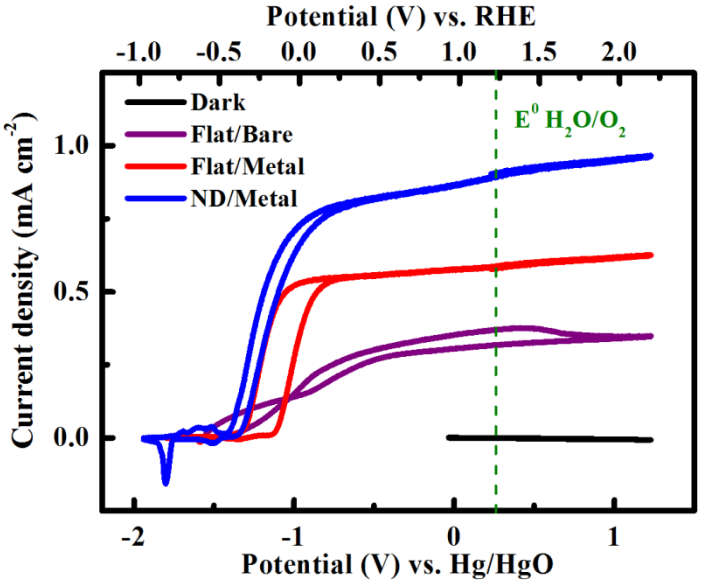

Figure 3-33: Comparison of CV characteristics of photoanodes with different surface structures.

Table 3-4: Summary of photoanodes performance (plasmonic metal nanostructures).

Electrode	**Current density (mA•cm^{-2}) at EH_2O/O_2**	**ABCE (% at 0V)**
ND/Metal	0.903	0.92
Flat/Metal	0.586	0.66
Flat/Bare	0.37	0.28

The two-electrode applied bias conversion efficiency (ABCE) measurement is subsequently conducted (Figure 3-34). The ND/Metal photoanode achieves 0.92% STH conversion efficiency at zero bias with a current density of 0.746 mA•cm^{-2}. The performances of different photoanodes are summarized in Table 3-4.

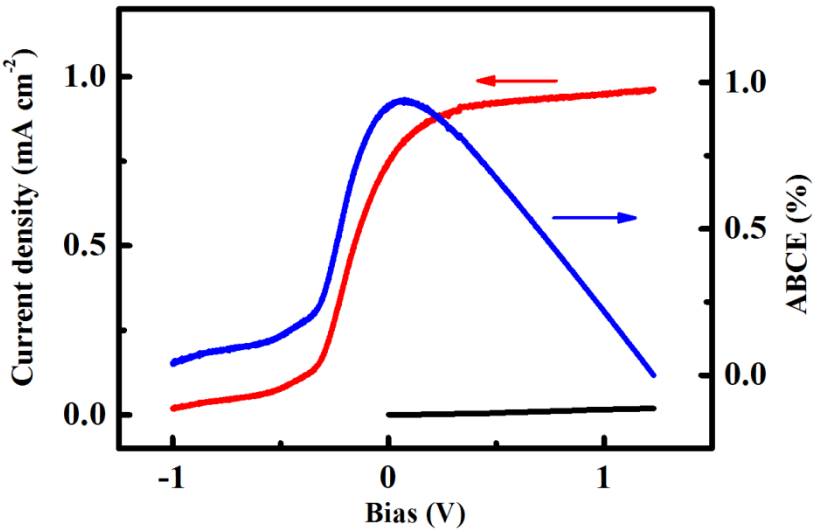

Figure 3-34: Two-electrode measurement and ABCE of ND/Metal photoanode.

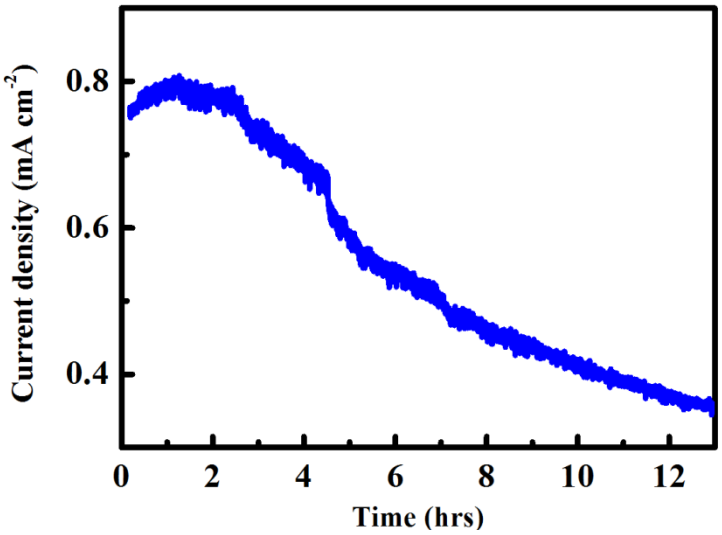

Figure 3-35: Stability test of ND/Metal photoanode under zero bias.

Lastly, the stability of the ND/Metal photoanode in the strong alkaline (pH=14) environment is studied. Setup is in two-electrode configuration, and the photoanode is

kept at zero bias. In 12 hours, the current density drops over 50% of its initial value (Figure 3-35). The possible reason of this decay is the Ag oxidation, which is also observed in PEC three-electrode characterization. In order to suppress the Ag oxidation, thicker Ni film should be deposited to fully protect the Ag film sidewall.

3.4.5 Summary

We have successfully created plasmonic metal nano-dent on InGaN/GaN MQW surface by laser interference ablation. It is found that the plasmonic metal nano-dent further improve the light absorption compared to flat metal structure. Simulations indicate that the plasmonic nanostructures cause electric field scattering and concentration within the sample, leading to a broad-wavelength light collection enhancement. Photoelectrode based on plasmonic metal nano-dent demonstrates a current density of 0.746 $mA \cdot cm^{-2}$ at zero bias, and an overall STH conversion efficiency of 0.92%, which is almost 1.5 times higher than photoelectrode with flat metal surface. The simple and high through-put manufacture process, together with the improved light absorption over broad wavelength range, makes our approach ideal for practical scale-up plasmon-enhanced solar water splitting and energy conversion.

3.5 Conclusion

In this chapter, PEC cells based on InGaN/GaN MQW for solar water splitting are demonstrated. First, PEC water splitting without biasing (spontaneous) is achieved from bare InGaN/GaN MQW photoanode. The InGaN/GaN MQW cell shows a STH conversion efficiency of 0.2% with current density of 0.16 $mA \cdot cm^{-2}$ at zero bias in pH 7 electrolyte. However, the performance stability is poor, probably due to the GaN oxidation and etching. Next, a Ni thin film layer is deposited on top of InGaN/GaN

MQW. This Ni film has multiple functions on improving the optical and electrical properties of the photoanode as well as the stability; but most importantly, it can be intentionally activated in alkaline electrolyte to form NiO_x as electrocatalysts for OER. The performance of the NiO_x|Ni|InGaN/GaN MQW cell is significantly improved, showing a STH conversion efficiency of 0.64%. Furthermore, plasmonic metal nanostructures are created on the photoanode by laser interference ablation for enhanced photon collection. Absorptions of photons with energies above and below the InGaN bandgap are both found improved, which is believed due to the plasmonic metal nanostructures induced local electric field enhancement. The overall STH conversion efficiency is found further boosted to 0.92% with ND/Metal InGaN/GaN MQW cell.

The use of InGaN/GaN MQW structure allows us to independently tune and optimize the solar energy harvesting and conversion processes and to overcome some inherited obstacles in the PEC system. To achieve high efficiency PEC water splitting and hydrogen fuel production, material growth (high In concentration in InGaN layer with good crystalline quality) would be the key. However, with the rapid development of wide bandgap semiconductors, especially in the GaN field, we believe that high performance, practical PEC cells can be readily built based on our studies and demonstrations.

Chapter 3, section 3.3, in part has been submitted for publication of the material as it may appear in Physical Chemistry Chemical Physics, 2014, Yang, Muchuan; Sun, Ke; Cheung Justin; Yu, Paul K.L.; Wang, Deli. The dissertation author was the primary investigator and the first author of this paper.

Chapter 3, section 3.4 in part is currently being prepared for submission for publication of the material. Yang, Muchuan; Lu, Dylan; Yuan, Dajun; Wang, Hsin-Ping; He, Jr-Hau; Liu, Zhaowei; Yu, Paul K.L.; Wang, Deli. The dissertation author was the primary investigator and the first author of this paper.

3.6 Appendix

This appendix describes the Matlab code for three beam laser interference simulation (Figure 3-26).

```
clc;
clear;
x=0:10:12000;
m=size(x);
y=0:10:12000;
n=size(y);
I_3beam=zeros(m(2),n(2));
alfa_degree=5.1;
alfa=alfa_degree/180*pi;
lambda=355;
k=2*pi/lambda;


for ii=1:m(2)
   for jj=1:n(2)
      I_3beam(ii,jj)=3*7/9+2*7/9*(cos(k*sin(alfa)*(-1.5*x(ii)+0.866*y(jj)))+cos(-
k*sin(alfa)*1.732*y(jj))+cos(k*sin(alfa)*(1.5*x(ii)+0.866*y(jj))));
   end;
end;


figure (1);
mesh(x,y,I_3beam);
```

3.7 References

1. Fujishima A., Honda K. Electrochemical Photolysis of Water at a Semiconductor Electrode. *Nature* **238**, 37 (1972).

2. Walter M.G., Warren E.L., McKone J.R., Boettcher S.W., Mi Q., Santori E.A., Lewis N.S. Solar Water Splitting Cells. *Chemical Reviews* **110**, 6446 (2010).

3. Li Z., Luo W., Zhang M., Feng J., Zou Z. Photoelectrochemical cells for solar hydrogen production: current state of promising photoelectrodes, methods to improve their properties, and outlook. *Energy & Environmental Science* **6**, 347 (2013).

4. Alexander B.D., Kulesza P.J., Rutkowska I., Solarska R., Augustynski J. Metal oxide photoanodes for solar hydrogen production. *Journal of Materials Chemistry* **18**, 2298 (2008).

5. Kennedy J.H., Frese K.W. Photooxidation of Water at α - Fe2 O 3 Electrodes. *Journal of The Electrochemical Society* **125**, 709 (1978).

6. Sivula K., Le Formal F., Grätzel M. Solar Water Splitting: Progress Using Hematite (α-Fe2O3) Photoelectrodes. *ChemSusChem* **4**, 432 (2011).

7. Mayer M.T., Du C., Wang D. Hematite/Si Nanowire Dual-Absorber System for Photoelectrochemical Water Splitting at Low Applied Potentials. *Journal of the American Chemical Society* **134**, 12406 (2012).

8. Vayssieres L. On Solar Hydrogen & Nanotechnology. John Wiley & Sons (Asia) Pte Ltd (2009).

9. Boris D.C., Harry B.R., Uros C., Jacek B.J., Vivekanand K., Todd D., Mahendra K.S. Photoelectrochemical activity of as-grown, α-Fe 2 O 3 nanowire array electrodes for water splitting. *Nanotechnology* **23**, 194009 (2012).

10. Lin Y., Xu Y., Mayer M.T., Simpson Z.I., McMahon G., Zhou S., Wang D. Growth of p-Type Hematite by Atomic Layer Deposition and Its Utilization for Improved Solar Water Splitting. *Journal of the American Chemical Society* **134**, 5508 (2012).

11. Hodes G., Cahen D., Manassen J. Tungsten trioxide as a photoanode for a photoelectrochemical cell (PEC). *Nature* **260**, 312 (1976).

12. Wagner F.T., Somorjai G.A. Photocatalytic and photoelectrochemical hydrogen production on strontium titanate single crystals. *Journal of the American Chemical Society* **102**, 5494 (1980).

13. Paulauskas I.E., Katz J.E., Jellison G.E., Lewis N.S., Boatner L.A., Brown G.M. Growth, Characterization, and Electrochemical Properties of Doped n-Type KTaO3 Photoanodes. *Journal of The Electrochemical Society* **156**, B580 (2009).

14. Reece S.Y., Hamel J.A., Sung K., Jarvi T.D., Esswein A.J., Pijpers J.J.H., Nocera D.G. Wireless Solar Water Splitting Using Silicon-Based Semiconductors and Earth-Abundant Catalysts. *Science* **334**, 645 (2011).

15. Khaselev O., Turner J.A. A Monolithic Photovoltaic-Photoelectrochemical Device for Hydrogen Production via Water Splitting. *Science* **280**, 425 (1998).

16. Kenney M.J., Gong M., Li Y., Wu J.Z., Feng J., Lanza M., Dai H. High-Performance Silicon Photoanodes Passivated with Ultrathin Nickel Films for Water Oxidation. *Science* **342**, 836 (2013).

17. Nakamura S., Senoh M., Nagahama S.-i., Iwasa N., Yamada T., Matsushita T., Sugimoto Y., Kiyoku H. Ridge-geometry InGaN multi-quantum-well-structure laser diodes. *Applied Physics Letters* **69**, 1477 (1996).

18. Jiang H.X., Jin S.X., Li J., Shakya J., Lin J.Y. III-nitride blue microdisplays. *Applied Physics Letters* **78**, 1303 (2001).

19. Dahal R., Pantha B., Li J., Lin J.Y., Jiang H.X. InGaN/GaN multiple quantum well solar cells with long operating wavelengths. *Applied Physics Letters* **94**, 063505 (2009).

20. Ho C.-H., Lai K.-Y., Lin C.-A., Lin G.-J., Hsing M.-K., He J.-H. Microdome InGaN-based multiple quantum well solar cells. *Applied Physics Letters* **101**, 023902 (2012).

21. Beach J.D., Collins R.T., Turner J.A. Band-Edge Potentials of n-Type and p-Type GaN. *Journal of The Electrochemical Society* **150**, A899 (2003).

22. Moses P.G., Van de Walle C.G. Band bowing and band alignment in InGaN alloys. *Applied Physics Letters* **96**, 021908 (2010).

23. Ono M., Fujii K., Ito T., Iwaki Y., Hirako A., Yao T., Ohkawa K. Photoelectrochemical reaction and H[sub 2] generation at zero bias optimized by carrier concentration of n-type GaN. *The Journal of Chemical Physics* **126**, 054708 (2007).

24. Waki I., Cohen D., Lal R., Mishra U., DenBaars S.P., Nakamura S. Direct water photoelectrolysis with patterned n-GaN. *Applied Physics Letters* **91**, 093519 (2007).

25. Li J., Lin J.Y., Jiang H.X. Direct hydrogen gas generation by using InGaN epilayers as working electrodes. *Applied Physics Letters* **93**, 162107 (2008).

26. Hwang Y.J., Wu C.H., Hahn C., Jeong H.E., Yang P. Si/InGaN Core/Shell Hierarchical Nanowire Arrays and their Photoelectrochemical Properties. *Nano Letters* **12**, 1678 (2012).

27. Benton J., Bai J., Wang T. Enhancement in solar hydrogen generation efficiency using a GaN-based nanorod structure. *Applied Physics Letters* **102**, 173905 (2013).

28. Muth J.F., Lee J.H., Shmagin I.K., Kolbas R.M., Casey J.H.C., Keller B.P., Mishra U.K., DenBaars S.P. Absorption coefficient, energy gap, exciton binding energy, and recombination lifetime of GaN obtained from transmission measurements. *Applied Physics Letters* **71**, 2572 (1997).

29. Tsai C.-L., Fan G.-C., Lee Y.-S. Effects of InGaN/GaN superlattice absorption layers on the structural and optical properties of InGaN solar cells. *Journal of Vacuum Science & Technology B* **29**, (2011).

30. Noh S.Y., Sun K., Choi C., Niu M., Yang M., Xu K., Jin S., Wang D. Branched TiO2/Si nanostructures for enhanced photoelectrochemical water splitting. *Nano Energy* **2**, 351 (2013).

31. Sun K., Park N., Sun Z., Zhou J., Wang J., Pang X., Shen S., Noh S.Y., Jing Y., Jin S., Yu P.K.L., Wang D. Nickel oxide functionalized silicon for efficient photo-oxidation of water. *Energy & Environmental Science* **5**, 7872 (2012).

32. Cai X.-m., Zeng S.-w., Zhang B.-p. Fabrication and characterization of InGaN p-i-n homojunction solar cell. *Applied Physics Letters* **95**, 173504 (2009).

33. S.M.Sze K.K.N. Physics of semiconductor devices. John Wiley & Sons, Inc. (2007).

34. Youtsey C., Adesida I., Bulman G. Broad-area photoelectrochemical etching of GaN. *Electronics Letters* **33**, 245 (1997).

35. Youtsey C., Bulman G., Adesida I. Dopant-selective photoenhanced wet etching of GaN. *Journal of Electronic Materials* **27**, 282 (1998).

36. Chen S., Wang L.-W. Thermodynamic Oxidation and Reduction Potentials of Photocatalytic Semiconductors in Aqueous Solution. *Chemistry of Materials* **24**, 3659 (2012).

37. Lee H.-Y., Huang X.-Y., Lee C.-T. Light Output Enhancement of GaN-Based Roughened LEDs Using Bias-Assisted Photoelectrochemical Etching Method. *Journal of The Electrochemical Society* **155**, H707 (2008).

38. Kamimura J., Bogdanoff P., Lähnemann J., Hauswald C., Geelhaar L., Fiechter S., Riechert H. Photoelectrochemical Properties of (In,Ga)N Nanowires for Water Splitting Investigated by in Situ Electrochemical Mass Spectroscopy. *Journal of the American Chemical Society* **135**, 10242 (2013).

39. Sun K., Pang X., Shen S., Qian X., Cheung J.S., Wang D. Metal Oxide Composite Enabled Nanotextured Si Photoanode for Efficient Solar Driven Water Oxidation. *Nano Letters* **13**, 2064 (2013).

40. Wang D., Pierre A., Kibria M.G., Cui K., Han X., Bevan K.H., Guo H., Paradis S., Hakima A.-R., Mi Z. Wafer-Level Photocatalytic Water Splitting on GaN Nanowire Arrays Grown by Molecular Beam Epitaxy. *Nano Letters* **11**, 2353 (2011).

41. Lodi G., Sivieri E., Battisti A., Trasatti S. Ruthenium dioxide-based film electrodes. *Journal of Applied Electrochemistry* **8**, 135 (1978).

42. Sakai Y., Sugahara S., Matsumura M., Nakato Y., Tsubomura H. Photoelectrochemical water splitting by tandem type and heterojunction amorphous silicon electrodes. *Canadian Journal of Chemistry* **66**, 1853 (1988).

43. Licht S., Wang B., Mukerji S., Soga T., Umeno M., Tributsch H. Efficient Solar Water Splitting, Exemplified by RuO2-Catalyzed AlGaAs/Si Photoelectrolysis. *The Journal of Physical Chemistry B* **104**, 8920 (2000).

44. Barral G., Diard J.P., Montella C. Re-examination of the voltage—pH diagram for the Ru-H2O system at 25°C. *Electrochimica Acta* **31**, 277 (1986).

45. Tseung A.C.C., Jasem S. Oxygen evolution on semiconducting oxides. *Electrochimica Acta* **22**, 31 (1977).

46. Young E.R., Costi R., Paydavosi S., Nocera D.G., Bulovic V. Photo-assisted water oxidation with cobalt-based catalyst formed from thin-film cobalt metal on silicon photoanodes. *Energy & Environmental Science* **4**, 2058 (2011).

47. Zaharieva I., Chernev P., Risch M., Klingan K., Kohlhoff M., Fischer A., Dau H. Electrosynthesis, functional, and structural characterization of a water-oxidizing manganese oxide. *Energy & Environmental Science* **5**, 7081 (2012).

48. Zhong D.K., Gamelin D.R. Photoelectrochemical Water Oxidation by Cobalt Catalyst ("Co−Pi")/α-Fe2O3 Composite Photoanodes: Oxygen Evolution and Resolution of a Kinetic Bottleneck. *Journal of the American Chemical Society* **132**, 4202 (2010).

49. Barroso M., Cowan A.J., Pendlebury S.R., Grätzel M., Klug D.R., Durrant J.R. The Role of Cobalt Phosphate in Enhancing the Photocatalytic Activity of α-Fe2O3 toward Water Oxidation. *Journal of the American Chemical Society* **133**, 14868 (2011).

50. Kanan M.W., Nocera D.G. In Situ Formation of an Oxygen-Evolving Catalyst in Neutral Water Containing Phosphate and Co2+. *Science* **321**, 1072 (2008).

51. Lutterman D.A., Surendranath Y., Nocera D.G. A Self-Healing Oxygen-Evolving Catalyst. *Journal of the American Chemical Society* **131**, 3838 (2009).

52. Kibria M.F., Mridha M.S. Electrochemical studies of the nickel electrode for the oxygen evolution reaction. *International Journal of Hydrogen Energy* **21**, 179 (1996).

53. Miller E.L., Rocheleau R.E. Electrochemical and Electrochromic Behavior of Reactively Sputtered Nickel Oxide. *Journal of The Electrochemical Society* **144**, 1995 (1997).

54. Bockris J.O.M. Kinetics of Activation Controlled Consecutive Electrochemical Reactions: Anodic Evolution of Oxygen. *The Journal of Chemical Physics* **24**, 817 (1956).

55. Qiao D., Yu L.S., Lau S.S., Lin J.Y., Jiang H.X., Haynes T.E. A study of the Au/Ni ohmic contact on p-GaN. *Journal of Applied Physics* **88**, 4196 (2000).

56. Medway S.L., Lucas C.A., Kowal A., Nichols R.J., Johnson D. In situ studies of the oxidation of nickel electrodes in alkaline solution. *Journal of Electroanalytical Chemistry* **587**, 172 (2006).

57. Seghiouer A., Chevalet J., Barhoun A., Lantelme F. Electrochemical oxidation of nickel in alkaline solutions: a voltammetric study and modelling. *Journal of Electroanalytical Chemistry* **442**, 113 (1998).

58. Lee Y.-J., Lee M.-H., Cheng C.-M., Yang C.-H. Enhanced conversion efficiency of InGaN multiple quantum well solar cells grown on a patterned sapphire substrate. *Applied Physics Letters* **98**, 263504 (2011).

59. Farrell R.M., Neufeld C.J., Cruz S.C., Lang J.R., Iza M., Keller S., Nakamura S., DenBaars S.P., Mishra U.K., Speck J.S. High quantum efficiency InGaN/GaN multiple quantum well solar cells with spectral response extending out to 520 nm. *Applied Physics Letters* **98**, 201107 (2011).

60. Li J., Cushing S.K., Zheng P., Meng F., Chu D., Wu N. Plasmon-induced photonic and energy-transfer enhancement of solar water splitting by a hematite nanorod array. *Nature Communication* **4**, (2013).

61. Standridge S.D., Schatz G.C., Hupp J.T. Distance Dependence of Plasmon-Enhanced Photocurrent in Dye-Sensitized Solar Cells. *Journal of the American Chemical Society* **131**, 8407 (2009).

62. Atwater H.A., Polman A. Plasmonics for improved photovoltaic devices. *Nature Materials* **9**, 205 (2010).

63. Ferry V.E., Munday J.N., Atwater H.A. Design Considerations for Plasmonic Photovoltaics. *Advanced Materials* **22**, 4794 (2010).

64. Warren S.C., Thimsen E. Plasmonic solar water splitting. *Energy & Environmental Science* **5**, 5133 (2012).

65. Dotan H., Kfir O., Sharlin E., Blank O., Gross M., Dumchin I., Ankonina G., Rothschild A. Resonant light trapping in ultrathin films for water splitting. *Nature Materials* **12**, 158 (2013).

66. Aydin K., Ferry V.E., Briggs R.M., Atwater H.A. Broadband polarization-independent resonant light absorption using ultrathin plasmonic super absorbers. *Nature Communication* **2**, 517 (2011).

67. Iandolo B., Antosiewicz T.J., Hellman A., Zoric I. On the mechanism for nanoplasmonic enhancement of photon to electron conversion in nanoparticle sensitized hematite films. *Physical Chemistry Chemical Physics* **15**, 4947 (2013).

68. Tian Y., Tatsuma T. Mechanisms and Applications of Plasmon-Induced Charge Separation at TiO2 Films Loaded with Gold Nanoparticles. *Journal of the American Chemical Society* **127**, 7632 (2005).

69. Cushing S.K., Li J., Meng F., Senty T.R., Suri S., Zhi M., Li M., Bristow A.D., Wu N. Photocatalytic Activity Enhanced by Plasmonic Resonant Energy Transfer from Metal to Semiconductor. *Journal of the American Chemical Society* **134**, 15033 (2012).

70. Chen H.M., Chen C.K., Chen C.-J., Cheng L.-C., Wu P.C., Cheng B.H., Ho Y.Z., Tseng M.L., Hsu Y.-Y., Chan T.-S., Lee J.-F., Liu R.-S., Tsai D.P. Plasmon Inducing Effects for Enhanced Photoelectrochemical Water Splitting: X-ray Absorption Approach to Electronic Structures. *ACS Nano* **6**, 7362 (2012).

71. Chen H.M., Chen C.K., Tseng M.L., Wu P.C., Chang C.M., Cheng L.-C., Huang H.W., Chan T.S., Huang D.-W., Liu R.-S., Tsai D.P. Plasmonic ZnO/Ag Embedded Structures as Collecting Layers for Photogenerating Electrons in Solar Hydrogen Generation Photoelectrodes. *Small* **9**, 2926 (2013).

72. Li J., Cushing S.K., Bright J., Meng F., Senty T.R., Zheng P., Bristow A.D., Wu N. Ag@Cu2O Core-Shell Nanoparticles as Visible-Light Plasmonic Photocatalysts. *ACS Catalysis* **3**, 47 (2012).

73. Xu S., Wei Y., Kirkham M., Liu J., Mai W., Davidovic D., Snyder R.L., Wang Z.L. Patterned Growth of Vertically Aligned ZnO Nanowire Arrays on Inorganic Substrates at Low Temperature without Catalyst. *Journal of the American Chemical Society* **130**, 14958 (2008).

74. Wang X., Summers C.J., Wang Z.L. Large-Scale Hexagonal-Patterned Growth of Aligned ZnO Nanorods for Nano-optoelectronics and Nanosensor Arrays. *Nano Letters* **4**, 423 (2004).

75. Mårtensson T., Carlberg P., Borgström M., Montelius L., Seifert W., Samuelson L. Nanowire Arrays Defined by Nanoimprint Lithography. *Nano Letters* **4**, 699 (2004).

76. Wei Y., Wu W., Guo R., Yuan D., Das S., Wang Z.L. Wafer-Scale High-Throughput Ordered Growth of Vertically Aligned ZnO Nanowire Arrays. *Nano Letters* **10**, 3414 (2010).

77. Yuan D., Guo R., Wei Y., Wu W., Ding Y., Wang Z.L., Das S. Heteroepitaxial Patterned Growth of Vertically Aligned and Periodically Distributed ZnO Nanowires on GaN Using Laser Interference Ablation. *Advanced Functional Materials* **20**, 3484 (2010).

78. Chu C.-F., Lai F.-I., Chu J.-T., Yu C.-C., Lin C.-F., Kuo H.-C., Wang S.C. Study of GaN light-emitting diodes fabricated by laser lift-off technique. *Journal of Applied Physics* **95**, 3916 (2004).

79. Dajun Y., Wei L., Rui G., Wong C.P., Suman D. The fabrication of vertically aligned and periodically distributed carbon nanotube bundles and periodically porous carbon nanotube films through a combination of laser interference ablation

and metal-catalyzed chemical vapor deposition. *Nanotechnology* **23**, 215303 (2012).

80. Pound B.G., Macdonald D.D., Tomlinson J.W. The electrochemistry of silver in koh at elevated temperatures—II. Cyclic voltammetry and galvanostatic charging studies. *Electrochimica Acta* **25**, 563 (1980).

Chapter 4

ZnO NWs Based Junctionless Light Emitting Device

4.1 Introduction

Wide bandgap semiconductors are promising materials for UV light sources, such as LEDs and LDs, which have broad applications in illumination, UV photolithography, high-density information storage and biosensing.[1] Compare to current large, toxic, low efficiency mercury based UV light sources, wide bandgap semiconductor LEDs/LDs are more compact, energy efficient and non-toxic, which technology has been advancing in a fast pace. However, one critical challenge associated with using wide bandgap semiconductors to make p-n junction for light emitting device is the difficulty in achieving p-type conductivity. Although p-type doping for GaN has been achieved,[2] only very limited success has been achieved for ZnO and other wide bandgap semiconductors.[3-6]

Since their introduction in the 1990s, inorganic semiconductor nanowires (NWs) have been extensively studied as novel light sources (LEDs/LDs) and much insight has been gained on their electrical and optical properties.[7] One advantage of NW LED over conventional planar structure is that the emitted light can be efficiently extracted from the material due to the waveguide effect. However, making effective electrical contacts for NW arrays has been problematic, and so far stalled their practical application. Typical

strategy involves filling the gap between NWs with insulating polymers or spin-on glass and coating transparent conducting materials (such as ITO) on the top of NWs.[8-10] These materials could affect the optical and electrical properties of NW LEDs, and cause inferior performance.

In this chapter, a demonstration of ZnO NWs based junctionless light emitting device (LED) that is able to overcome both obstacles mentioned above will be introduced. Inspired by the cathode ray tube (CRT) and field emission display, electron beam (EB) excitation is used as the carrier injection method. Vertical ZnO NW arrays are used as active light emitters. No p-n junction is formed in ZnO NWs in this approach, and no top electrical contact is required either. Electron-hole pairs are directly generated by energetic electron beams, and then recombine to emit light. Here, ZnO NWs are used as a demonstration, but this approach should be able to apply to other wide bandgap semiconductor nanostructures. The schematic of ZnO NW junctionless LED is shown in Figure 4-1. A carbon nanotubes (CNTs) based cathode and a ZnO NWs based anode are assembled face to face in a vacuum tube. Emitted through field emission process, electrons from CNTs directly shower on ZnO NWs, generate electron-hole pairs inside ZnO NWs, which subsequently recombine to give light emission. Strong near band edge emission is obtained from ZnO NWs. More importantly, the UV light from the ZnO NWs is able to excite different phosphors for color tuning, and this could potentially lead to white light illumination. This approach indicates a pathway for nanoscale materials based lighting technology.

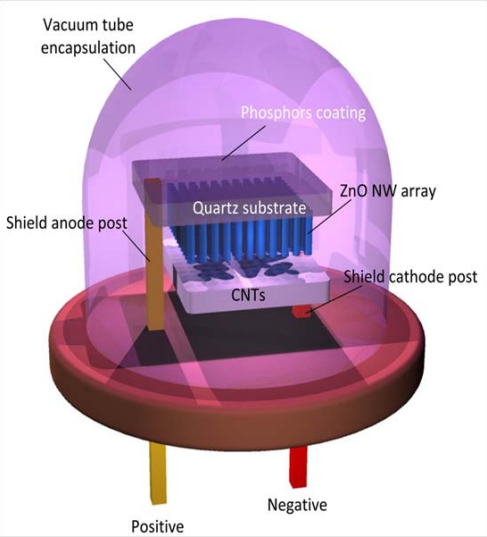

Figure 4-1: Schematic of ZnO NW junctionless light emitting device.

4.2 Electron beam excitation

4.2.1 Examples

Electron beam excitation has been successfully applied on some wide bandgap nitride semiconductor based light sources, as an alternative for carrier injection and generation. For example, high energy (8 kV) electrons are irradiated onto a AlGaN/AlN MQWs for efficient UV emission with ~ 40% power efficiency, which is significantly higher than that of AlGaN p-n junction LED with electrical injection.[11] The low efficiency of traditional p-n junction device is due to the intrinsically low hole concentration in p-type AlGaN, which is predicted only of ~ 2×10^{10} cm^{-3} at room temperature. This very low value degrades the hole transport as well as the electron-hole recombination, and eventually the light emission efficiency. With electrons penetrating into the MQW region, electron-hole pairs are directly generated in QWs, so they can efficiently recombine, and lead to much higher efficiency. Another example is that Watanabe and colleagues use electron field emitter and boron nitride (BN) powders to

fabricate a deep UV emission device.[12] These two demonstrations show electron beam excitation as a way for carrier injection and generation for UV light emitting devices.

4.2.2 Carbon nanotube electron field emission

Electron field emission is a phenomenon of emission of electrons from a solid surface, induced by a very high electrostatic field in vacuum. Field emission is explained by quantum tunneling theory, and is considered one of triumphs of quantum mechanics. Electron field emission has been used in application of displays, microscopy, and so on.

Electron field emission from nanoscale materials such as carbon nanotubes[13-15] (CNTs) has motivated a lot of interests in both industrial and academic research fields. Because of their nanometric tips, high local electric field can be generated at the CNT tops. This reduces the threshold voltage for electron emission, and thus more energy efficient field emission can be made. Prototypes of CNT based lamps and flat panel displays[16, 17] have both been demonstrated with impressive performance.

Here, multi-wall carbon nanotubes (MWNTs) are used as electron field emitters. Their field emission property is first measured. To fabricate the cathode, MWNTs are mixed with a silver paste, and the CNT paste is painted on a gold coated quartz substrate. An adhesive tape is used to pull the CNT tips out of the paste. The SEM image of the as-fabricated sample shows (Figure 4-2a) there is plenty of protruding CNT tips; each tip can be an effective electron emission site. The sample is then loaded into a vacuum chamber for field emission test.

The electron field emission characteristics of the cathode are measured in a vacuum chamber at pressure of 2.5e-5 Pa and with anode-cathode distance of ~200 μm. A copper rod with hemisphere tip of 1mm in diameter is used as anode electrode (shown

in Figure 4-2a inset). The emission current is measured with a Keithley 237 source-meter. The field emission test results are shown in Figure 4-2b. The rectifying *J-V* curve is typical for field emission devices, with a turn-on threshold voltage around 900 V. The Fowler-Nordheim Equation:[18]

$$J = a\beta^2 \frac{E^2}{\phi} \exp\left(-\frac{b}{\beta}\frac{\phi^{3/2}}{E}\right) \qquad \textbf{4-1}$$

$$\ln\left(J/E^2\right) = -\frac{b}{\beta}\phi^{3/2}\frac{1}{E} + \ln\left(\frac{a\beta^2}{\phi}\right) \qquad \textbf{4-2}$$

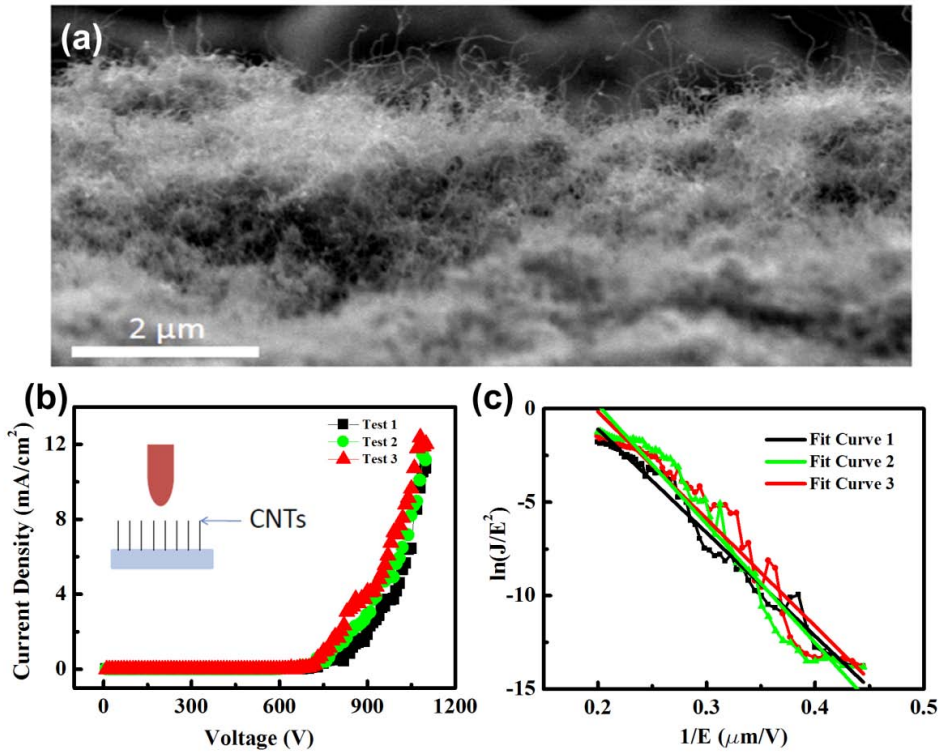

Figure 4-2: (a) SEM image of CNT cathode, (b) *J-V* plot of field emission measurement, (c) Fowler-Nordheim plot of field emission data.

where J is the current density, E is the electrical field, β is the field enhancement factor, ϕ is the material work function, and a, b are constants, describes the tunnelling behavior and can be transformed into a linear equation. As shown in Figure 4-2c, the fitting curves

of the obtained data from field emission show linear behavior, which is a signature sign of field emission.

4.3 Experiment setup

Figure 4-3a shows the schematic of assembled device under test condition. For the anode, Al grids are patterned on quartz substrate through a standard photolithography process (Figure 4-3b). The grid structure acts as the bottom electrode, generating electric field, as well as a window layer allowing light emission. Vertically-aligned ZnO nanowire arrays are then grown by low temperature hydrothermal technique described in chapter 2. A 50nm thin Al layer is then deposited on the upper faces of as-grown ZnO NWs by electron beam evaporation (Figure 4-3c), serving as the UV reflection mirror layer. After the fabrication processes, anode and cathode are assembled together using 1mm thick glass slides as spacers, and loaded into vacuum chamber (Figure 4-3d) for optical and electrical measurement. Figure 4-3e and f show sample module in the vacuum chamber under test condition.

To achieve a stable electron emission, the typical voltage-current data are recorded after several voltage sweeps up to 5 kV. A high voltage source integrated with a current meter (maximum current of 2 mA, resolution of 0.01 mA) is employed to manually apply the voltage and record the corresponding current. The light is collected by the optical fiber which is vertically put onto the top surface of quartz viewport. The emission spectra are recorded by the StellarNet EPP2000 fiber optic spectrometer with spectral measurement ranges from 190-2200 nm and resolution of 0.5 nm.

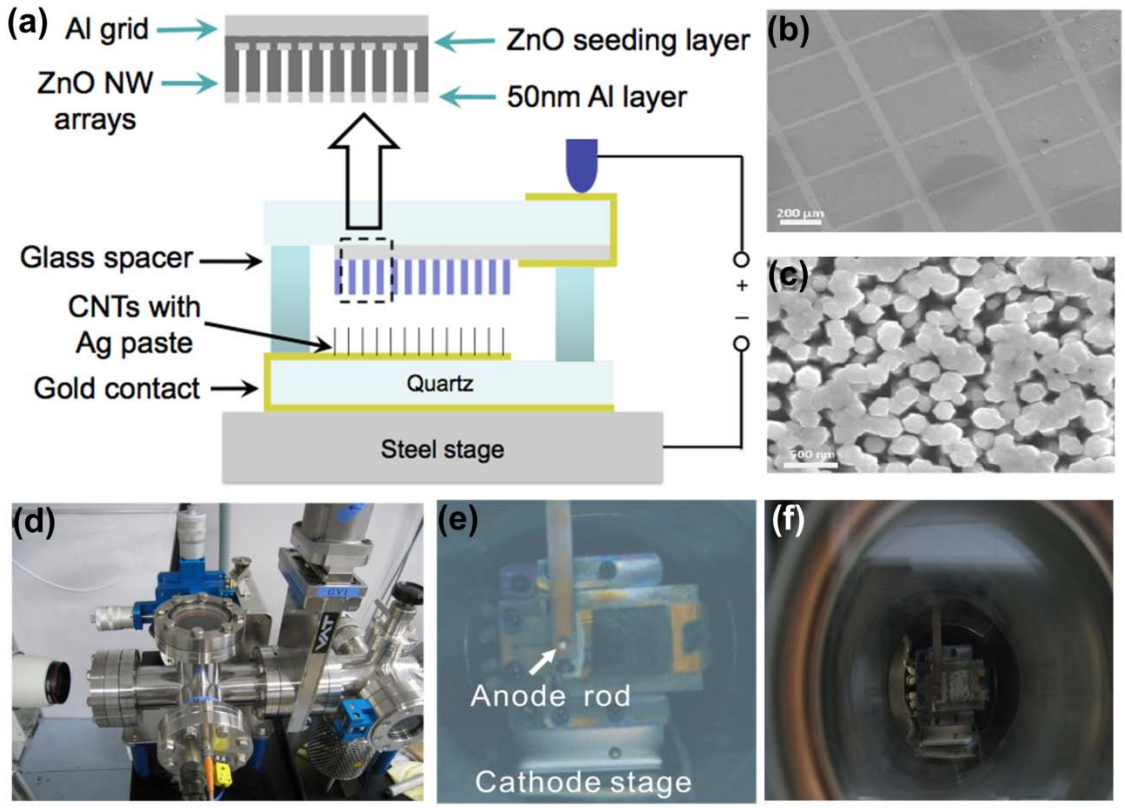

Figure 4-3: (a) Schematic of assemble module under test condition. (b) SEM image of ZnO NW arrays on Al grid. (c) SEM image of ZnO NWs topped with 50 nm Al film. (d) Vacuum chamber for test. (e) Sample device on stage, (f) Sample and stage image from optical window.

4.4 Results and discussion

When the anode voltage increases up to 3.5 kV, the device starts to turn on (detectable light emission). A simulation based on Monte Carlo method indicates that with an anode voltage of 4 kV, electrons are able to penetrate the 50 nm Al film, and reach the underneath ZnO (Figure 4-4a). The electrons start to losing energy in ZnO by either generating electron-hole pairs or interacting with lattices. Figure 4-4b shows the electrons energy distribution in the ZnO.

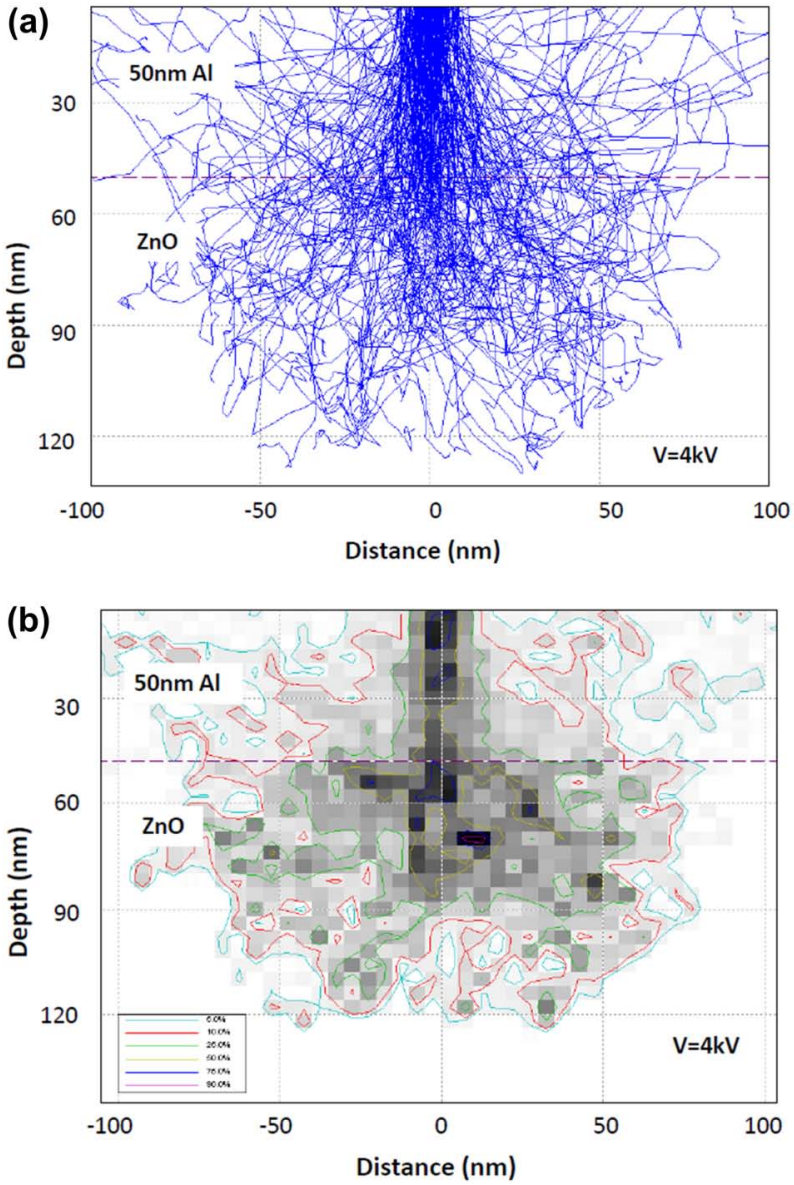

Figure 4-4: (a) Electron trajectories simulation with sample structure of 50nm Al film/ZnO substrate. (b) Energy distribution of electrons.

Figure 4-5a presents a typical spectrum from our device, showing a near band edge emission at 390nm. The band edge emission is attributed to free-exciton annihilation. This result shows the same trend as the room temperature cathodoluminescence (CL) spectrum (Figure 4-5b). Both of them show a dominate peak in the UV region. Besides the UV emission, room-temperature spectra from ZnO usually

exhibit one or more peaks from the defects-related emission in the visible region. The high intensity ratio of UV to the defect emission from our ZnO NWs, indicates that the ZnO NWs have relatively good crystalline quality. However, it should be noted that this ratio cannot be used as an absolute criterion for the sample quality; it is also dependent on

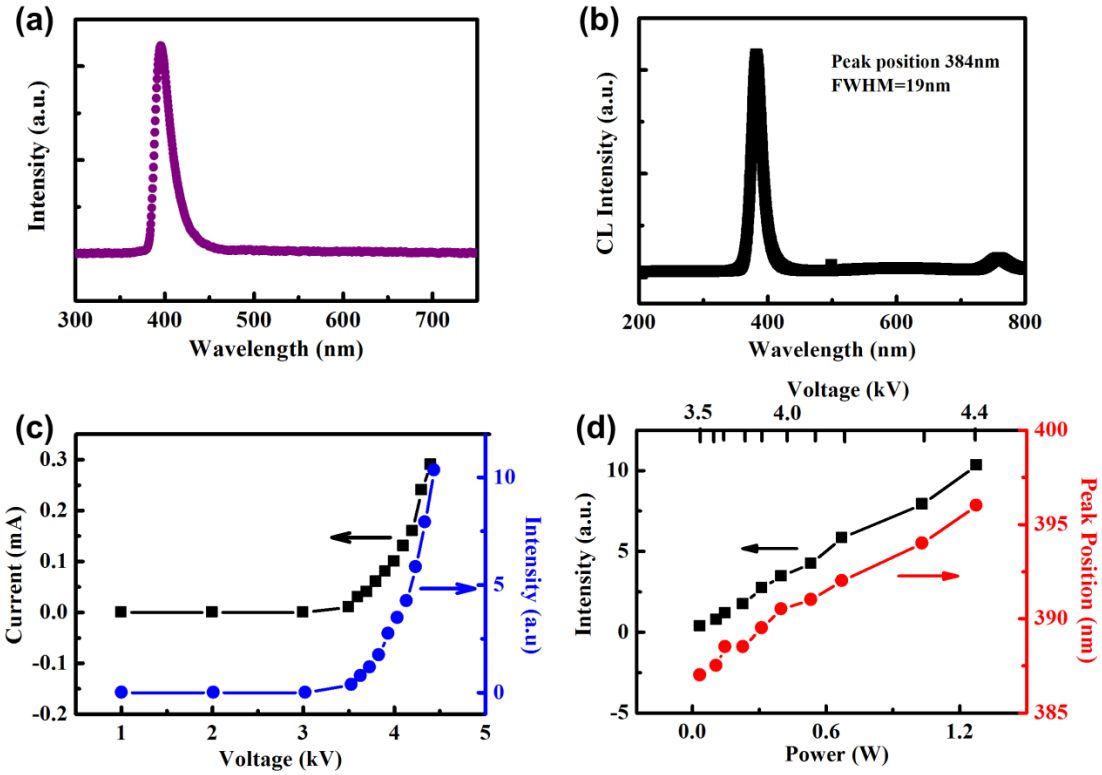

Figure 4-5: (a) Spectrum ZnO NW light emission. (b) CL measurement of ZnO NW. (c) I-V characteristic of LED (black curve); light intensity vs. voltage (blue curve). (d) Light intensity vs. applied power (black curve); spectrum peak position vs. applied power (red curve).

the excitation power as well as the excitation area. Figure 4-5c and d summarize the electrical and optical properties of our NW LED. In Figure 4-5c, the current and light intensity show standard rectifying behaviors, which correspond to the origin of field emission. After turn-on, the light intensity increases linearly with the applied power. This property promises that ZnO NW LED is completely dimmable. A red-shift of the

emission peaks occurs when the power increases. This could be attributed to the heating of ZnO caused by the high energy electron and lattice interaction.

By coating the backside of the anode with different PL phosphors (Figure 4-6a), we demonstrate that the UV light from ZnO NWs is able to excite those phosphors to generate different colors. The normalized spectra and the corresponding photographs of

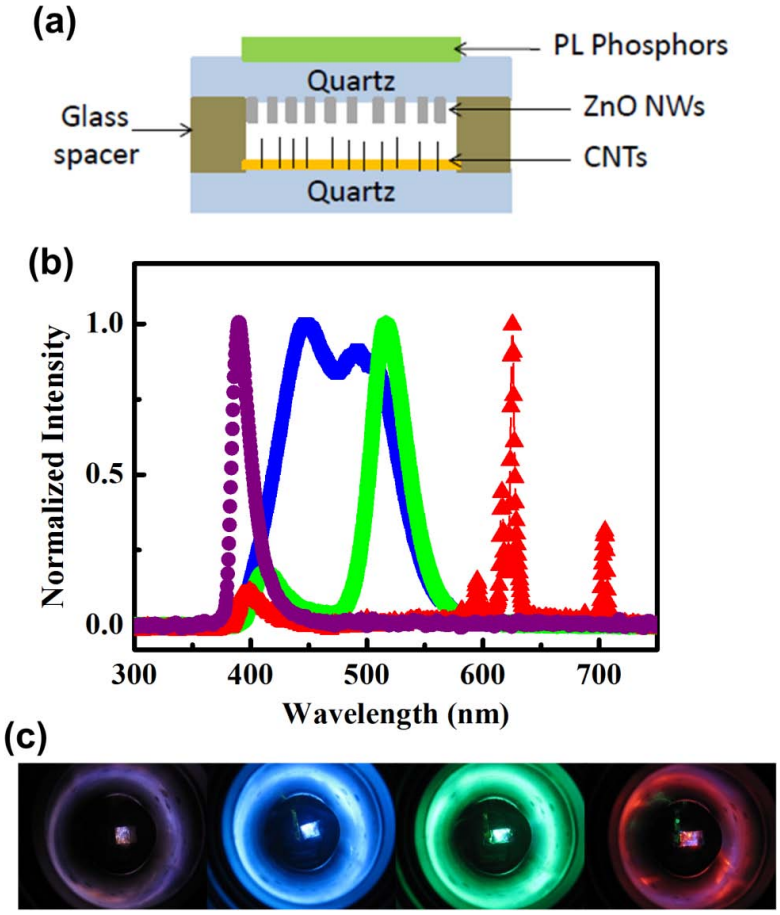

Figure 4-6: (a) Schematic of device coated with phosphor, (b) Normalized spectra of device coated with/without phosphors, (c) Optical images of devices emitting light.

phosphor-coated samples are shown in Figure 4-6b. The PL phosphors are those used for fluorescent lamps. Note that compared to fluorescent lamps, which require small amount of toxic mercury vapor to generate UV and excite phosphors, this device is apparently

more environmentally friendly. Figure 4-6c shows optical images of devices with phosphors.

According to the description above, with cathode and anode face to face, generating electrons and photons respectively, direct current (DC) signal is required, and light emission only occurs on one side. This configuration limits the device performance. In order to overcome this shortcoming, exploring a more efficient and practical design is of great interests. Instead of previously discussed structure, where CNTs and ZnO NWs are separated on cathode and anode, in the new design, CNTs and ZnO NWs are combined on both electrodes. First, ZnO NWs were grown on Al grid, and then topped with 50nm Al layer, just like described before. Then CNTs were sprayed on the samples, and an additional 10nm Al layer was deposited by electron beam evaporation, to hold the CNTs on the ZnO NWs. The electron field emission from CNTs has been considered to be instant, and the electron flight time between two electrodes is much smaller than the general power supply polarity switching time, which is typically 0.02s (50Hz). Electrons from one electrode could reach the opposite electrode before the polarization switched, and therefore photon generation could happen on both electrodes. After measuring the *I-V* characteristic and the emission spectrum from one electrode, we invert the entire device and measure again from the other electrode. Figure 4-7a and b present the electrical and optical measurements results of such device. The *I-V* curves both show rectifying behaviors (Figure 4-7a) and the two emission peaks from both electrodes overlap at 392nm (Figure 4-7b). This configuration offers additional freedom for light device design. For example, by coating different phosphors on two electrodes, one could easily mix different colors and potentially obtain white light.

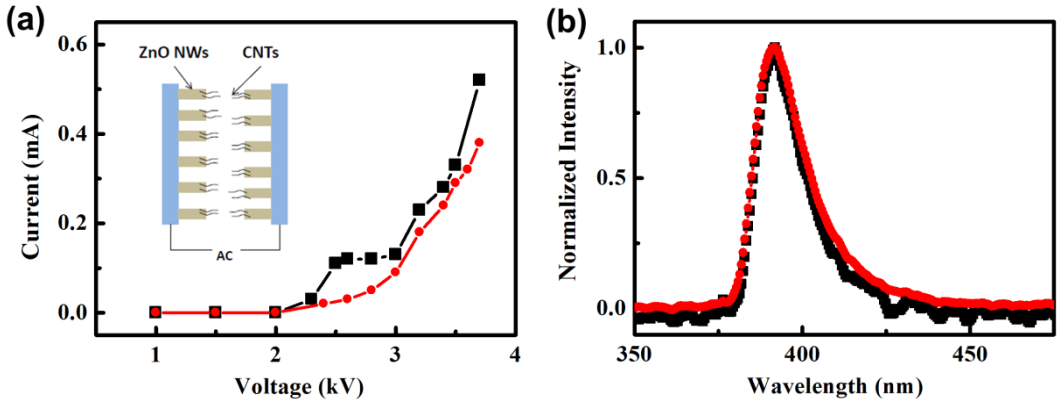

Figure 4-7: (a) Voltage versus current plots for both sides of the NW LED. The inset is a schematic of the AC configuration of the device. (b) Normalized spectra from the both sides of the device. The two emission peaks overlap at 392nm.

4.5 Conclusion

A new light emitting device based on ZnO NW arrays is demonstrated. Using energetic electron beam excitation, no p-n junction is required and no top electrical contact for ZnO NWs either. Strong near band UV emission is obtained. After coating the devices with PL phosphors, different colors are obtained. Moreover, a new design, which would enable the device working under AC signal, is explored. One could easily imagine that by employing our design, and using different semiconductor NWs, a lot of new and interesting phenomena or device structures could be achieved. Our work suggests a new strategy to solve the problems in wide bandgap semiconductor NW LEDs, in which electrode and junction technologies are not sufficiently advanced. It opens the door for the realization of more efficient, more ecological and more economic light sources.

Chapter 4, in part is currently being prepared for submission for publication of the material. Yang, Muchuan; Li, Chun; Sun, Ke; Jing, Yi; Bendo, Yoshio; Wang, Deli. The dissertation author was the primary investigator and author of this paper.

4.6 References

1. Takahashi K., Yoshikawa A., Sandhu A. Wide Bandgap Semiconductors. Springer Berlin Heidelberg (2007).

2. Nakamura S., Iwasa N., Senoh M., Mukai T. Thermal Annealing Effects on P-Type Mg-Doped GaN Films. *Japanese Journal of Applied Physics* **31**, (1992).

3. Chu S., Wang G., Zhou W., Lin Y., Chernyak L., Zhao J., Kong J., Li L., Ren J., Liu J. Electrically pumped waveguide lasing from ZnO nanowires. *Nature Nanotechnology* **6**, 506 (2011).

4. Taniyasu Y., Kasu M., Makimoto T. An aluminium nitride light-emitting diode with a wavelength of 210 nanometres. *Nature* **441**, 325 (2006).

5. Khan A., Balakrishnan K., Katona T. Ultraviolet light-emitting diodes based on group three nitrides. *Nature Photonics* **2**, 77 (2008).

6. Chen M.-T., Lu M.-P., Wu Y.-J., Song J., Lee C.-Y., Lu M.-Y., Chang Y.-C., Chou L.-J., Wang Z.L., Chen L.-J. Near UV LEDs Made with in Situ Doped p-n Homojunction ZnO Nanowire Arrays. *Nano Letters* **10**, 4387 (2010).

7. Yan R., Gargas D., Yang P. Nanowire photonics. *Nature Photonics* **3**, 569 (2009).

8. Xu S., Xu C., Liu Y., Hu Y., Yang R., Yang Q., Ryou J.-H., Kim H.J., Lochner Z., Choi S., Dupuis R., Wang Z.L. Ordered Nanowire Array Blue/Near-UV Light Emitting Diodes. *Advanced Materials* **22**, 4749 (2010).

9. Nadarajah A., Word R.C., Meiss J., Konenkamp R. Flexible Inorganic Nanowire Light-Emitting Diode. *Nano Letters* **8**, 534 (2008).

10. Lee C.-H., Yoo J., Hong Y.J., Cho J., Kim Y.-J., Jeon S.-R., Baek J.H., Yi G.-C. GaN/$In_{1-x}Ga_xN$/GaN/ZnO nanoarchitecture light emitting diode microarrays. *Applied Physics Letters* **94**, 213101 (2009).

11. Oto T., Banal R.G., Kataoka K., Funato M., Kawakami Y. 100 mW deep-ultraviolet emission from aluminium-nitride-based quantum wells pumped by an electron beam. *Nature Photonics* **4**, 767 (2010).

12. Watanabe K., Taniguchi T., Niiyama T., Miya K., Taniguchi M. Far-ultraviolet plane-emission handheld device based on hexagonal boron nitride. *Nature Photonics* **3**, 591 (2009).

13. Deheer W.A., Chatelain A., Ugarte D. A Carbon Nanotube Field-emission Electron Source. *Science* **270**, 1179 (1995).

14. Baughman R.H., Zakhidov A.A., de Heer W.A. Carbon Nanotubes--the Route Toward Applications. *Science* **297**, 787 (2002).

15. Lee N.S., Chung D.S., Han I.T., Kang J.H., Choi Y.S., Kim H.Y., Park S.H., Jin Y.W., Yi W.K., Yun M.J., Jung J.E., Lee C.J., You J.H., Jo S.H., Lee C.G., Kim J.M. Application of carbon nanotubes to field emission displays. *Diamond and Related Materials* **10**, 265 (2001).

16. Wang Q.H., Yan M., Chang R.P.H. Flat panel display prototype using gated carbon nanotube field emitters. *Applied Physics Letters* **78**, 1294 (2001).

17. Choi W.B., Chung D.S., Kang J.H., Kim H.Y., Jin Y.W., Han I.T., Lee Y.H., Jung J.E., Lee N.S., Park G.S., Kim J.M. Fully sealed, high-brightness carbon-nanotube field-emission display. *Applied Physics Letters* **75**, 3129 (1999).

18. Fowler R.H., Nordheim L. Electron Emission in Intense Electric Fields. *Proceedings of the Royal Society of London Series A* **119**, 173 (1928).

Chapter 5

Conclusions

In this dissertation, wide bandgap semiconductors are used for renewable energy and energy efficiency applications. Specifically speaking, InGaN/GaN MQW based photoelectrode for PEC solar water splitting and hydrogen fuel generation, and ZnO nanowires based light emitting device. The main accomplishments and contributions are summarized below:

- For the first time, InGaN/GaN MQW photoelectrode is used for PEC solar water splitting.
- The unique properties of InGaN/GaN MQW structure overcomes some inherent obstacles in photoelectrode design, allows the decoupling of light absorption, photovoltage generation, and electrochemical reaction.
- Spontaneous solar water splitting is demonstrated with a peak efficiency of 0.2% at zero bias.
- A NiO_x|Ni layer is applied on InGaN/GaN MQW photoelectrode. The NiO_x serves as oxygen evolution catalysts. The efficiency is improved to 0.64% at zero bias.
- The NiO_x|Ni layer also successfully suppresses the GaN oxidation, which is a severe problem in all III-nitride based PEC cell. The photoelectrode stability is improved.

- For the first time, plasmonic metal nano-dent are created and used to improve the light absorption ability of the InGaN/GaN MQW photoelectrode. The efficiency is further increased to 0.92%.
- Electron beam excitation is used to overcome the low p-type carrier concentration in some wide bandgap semiconductors and the carrier injection issue for nanowires.
- ZnO nanowires based junctionless light emission device is invented.
- Near band-edge emission is obtained from ZnO nanowires.
- Color tuning is achieved.
- Face-to-face design which can be potentially working under alternative current.

Chapter 6

Future work

6.1 Light absorption enhancement for InGaN/GaN MQW PEC cell

The STH conversion efficiency can be obtained by using Equation 3-9. In InGan/GaN MQW PEC cell, since there is sufficient photovoltage from the photoelectrode to split water, the STH conversion efficiency is simply related to photocurrent:

$$STH(\%) = 1.23 \times J_{ph}\left(mA \bullet cm^{-2}\right) \qquad \textbf{6-1}$$

Therefore, improving the photocurrent is of crucial importance to achieve high efficiency PEC cell. In Table 6-1, it is shown that for Flat/Metal sample, at wavelength of 450 nm, the absorption is about 60%. The corresponding theoretical photocurrent density is calculated to be 2.2 mA•cm^{-2}, however, the short circuit current density obtained in photovoltaic measurement is only 0.62 mA•cm^{-2}, indicating the existence of strong carrier recombination and loss, which can be partly due to the carrier trapping from MQWs. If we expect that sample can absorb most (>85%) of the incident light, the thickness of the total InGaN layer should be doubled, which means increasing the number of QWs to 20. However, increasing the QW number could also lead to poor material quality and serious recombination of the photo-generated carriers, which offset the light absorption. With ND/Metal, the absorption at 450 nm increases to 70%. In order to have 85% absorption of the incident light, 16 QWs are needed. It is clear that the ND/Metal

sample can achieve the same amount of light harvest with less number of QWs, and therefore reduce the carrier recombination and enhance the photocurrent.

Table 6-1: Light absorption and photocurrent study of InGaN/GaN MQW photoanodes.

Photoanode	**Number of QWs**	**Absorption at 450nm (%)**	**Theoretical photocurrent density (mA•cm^{-2})**	**J_{sc} in PV measurement (mA•cm^{-2})**	**QWs needed to achieve 85% absorption at 450 nm**
Flat/Metal	10	60	2.2	0.62	20
ND/Metal	10	70	2.4	0.98	16

Here, optimization of the metal nano-dent design based on simulation and using the simulation results to guide the material growth for further improved light absorption ability for the InGaN/GaN MQW photoelectrode will be discussed. In order to effectively enable surface plasmon resonance at 450 nm (bandgap of InGaN), periodicity between nano-dent is expected to be smaller than that.[1] A simulation with smaller periodicity (P=400 nm) of nano-dent (P=450 nm in section 3.4) is conducted to study the absorption property of the ND/Metal. In Figure 6-1, it is found that at short wavelength (< 500 nm); the absorption enhancement factors over Flat/Bare in both cases are very close. However, the smaller periodicity case (P=400 nm) shows higher absorption at longer wavelength (>500 nm). If the absorption edge of InGaN QW can be moved to longer wavelength, the plasmonic metal nano-dent arrays with periodicity of 400 nm are believed to be able to further improve the light absorption.

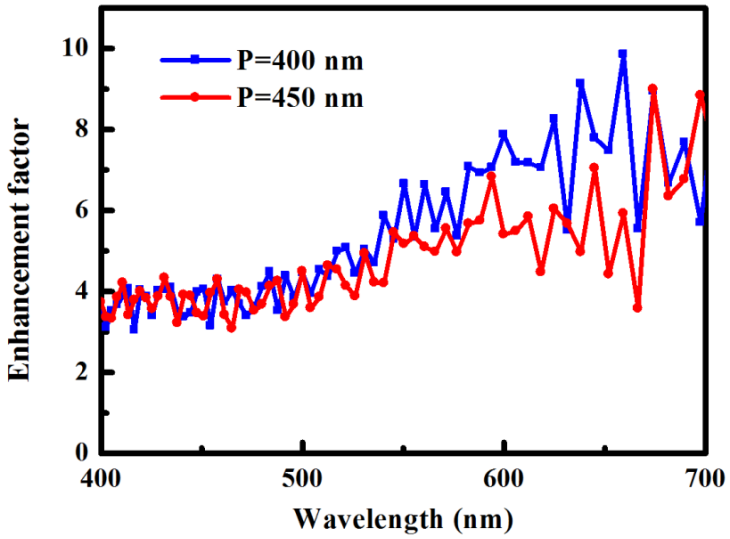

Figure 6-1: Simulated absorption enhancement of ND/Metal with periodicity of 400 nm and 450 nm over Flat/Bare.

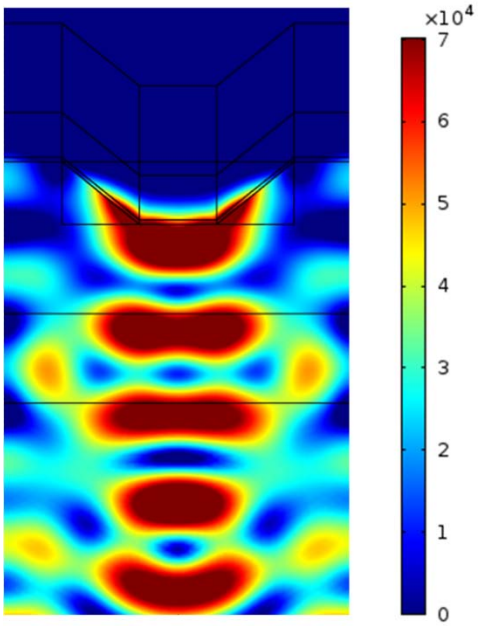

Figure 6-2: Full-wave numerical simulation for the electromagnetic wave (wavelength of 450 nm) distribution of the magnitude of electric field for ND/Metal with periodicity of 400 nm.

In the full-wave numerical simulation for the electromagnetic wave (wavelength of 450 nm) distribution in the ND/Metal with P=400 nm (Figure 6-2), it is found that incident light is concentrated in the metal nano-dent, which subsequently launches a

guided optical mode in the photoelectrode. The guided nature of the optical mode in the photoelectrode is revealed by the well-defined nodes in the electric field. The mode extends deep into the n-GaN region. By increasing the number of InGaN QWs, the waveguiding effect from plasmonic metal nano-dent should have a huge impact on the photonic enhancement.

6.2 Quantitative detection of hydrogen and oxygen

In PEC experiment, measured photocurrent reflects consequences of the electrochemical reactions, including desired and undesired product formation and the decomposition and dissolution of photoelectrode materials. The photocurrent, thus, cannot be used directly for quantitative analyses of the H_2 and O_2 evolution reaction. It is quantitative detection of H_2 and O_2 in the gas phase that provides direct evidence of true water splitting.

To investigate the gas evolution reactions and the STH efficiency, electrochemical mass spectrometry can be used. This technique essentially combines electrochemical half-cell experiment with mass spectrometry (EMS).[2] This allows the in situ, mass resolved observation of gaseous or volatile electrochemical reactants, reaction intermediates and products. The EMS has been applied to study the InGaN NW photoanode in water splitting, and detects only N_2 evolution.[3] EMS gives a direct experimental evidence of InGaN photoelectrode decomposition, and this information is very important to guide the design and optimization of GaN based photoelectrodes.

6.3 InGaN/GaN MQW wireless PEC cell

In section 3.2, spontaneous solar water splitting based on InGaN/GaN MQW photoelectrode is achieved. In section 3.3, by adding a top Ni thin film onto MQW, a

more efficient and robust photoanode is obtained, because of the NiO_x catalytic effect and surface protection. To further boost the photocurrent for water splitting, in section 3.4, plasmonic structures are created on the surface of photoanode to enhance solar light absorption.

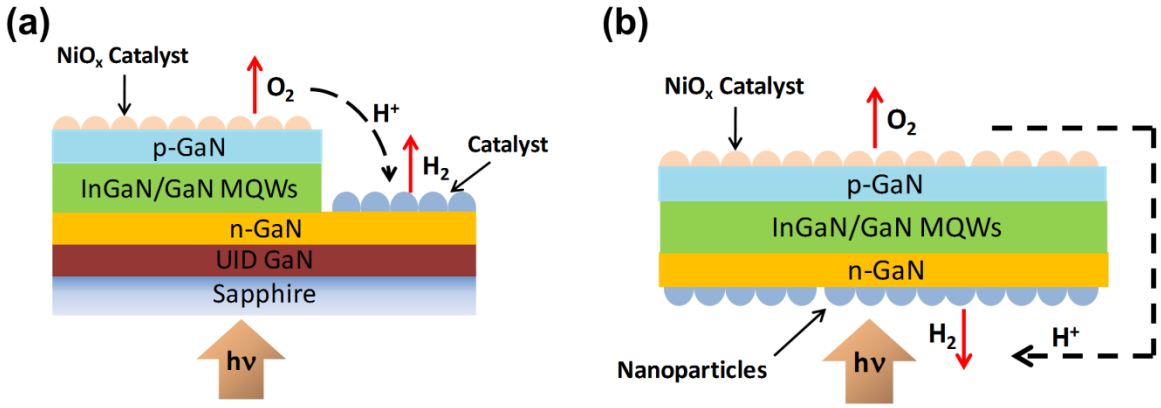

Figure 6-3: (a) InGaN/GaN wireless PEC cell with sapphire substrate. Hydrogen and oxygen evolutions happen at the same side. (b) InGaN/GaN wireless PEC cell, hydrogen and oxygen evolutions happen at two sides.

As a matter of fact, the beauty of using InGaN/GaN MQW structure is that with the sufficient photovoltage, it can be a self-powered wireless PEC cell, with the p-type GaN as the anode for oxygen evolution and n-type GaN as the cathode for hydrogen evolution. A schematic of InGaN/GaN MQW wireless PEC cell is illustrated in Figure 6-3a. In this case, sapphire is still used as the substrate for the growth. After the InGaN/GaN MQW growth, n-GaN is exposed by dry etching, and then coated with hydrogen evolution catalysts, such as Pt. HER and OER take place at the same side of the device. Alternatively, as shown in Figure 6-3b, after separating from the substrate, HER and OER could happen respectively on one side. Another advantage of using this configuration is that photo-carriers can travel vertically, rather than laterally, which would significantly reduce the recombination in the material as well as the series

resistance. The challenge lies on how to separate the InGaN/GaN MQW device from the substrate. The solution can be inserting some sacrificial layers between sapphire and InGaN/GaN MQW. As demonstrated in section 2.4, InGaN/GaN layers have been successfully grown on solution synthesized ZnO film. Based on those results, the complete InGaN/GaN MQW structure can be obtained by continuing growing a p-GaN layer. The epitaxial InGaN/GaN MQW can then be separated from the sapphire substrate by removing ZnO in diluted acid, such 10% HCl, leaving behind freestanding InGaN/GaN MQW film.

6.4 References

1. Kooyman R.P.H. Physics of Surface Plasmon Resonance. In: *Handbook of Sruface Plasmon Resonance*. The Royal Society of Chemistry (2008).

2. Bogdanoff P., Alonso-Vante N. On-line Determination via Differential Electrochemical Mass Spectroscopy (DEMS) of Chemical Products Formed in Photoelectrocatalytical Systems. *Berichte der Bunsengesellschaft für physikalische Chemie* **97**, 940 (1993).

3. Kamimura J., Bogdanoff P., Lähnemann J., Hauswald C., Geelhaar L., Fiechter S., Riechert H. Photoelectrochemical Properties of (In,Ga)N Nanowires for Water Splitting Investigated by in Situ Electrochemical Mass Spectroscopy. *Journal of the American Chemical Society* **135**, 10242 (2013).